DEVELOPMENT OF RADAR-ABSORBING COMPOSITE STRUCTURES

A Thesis Submitted to
the Graduate School of Engineering and Sciences of
İzmir Institute of Technology
in Partial Fulfillment of the Requirements for the Degree of

MASTER OF SCIENCE

in Materials Science and Engineering

by
Serkan KANGAL

July 2013
İZMİR

We approve the thesis of **Serkan KANGAL**

Examining Committee Members:

_____

Prof. Dr. Arzu MARMARALI
Department of Textile Engineering, Ege University

_____

Asisst. Prof. Dr. Engin ÖZÇİVİCİ
Department of Mechanical Engineering, İzmir Institute of Technology

_____

Assist. Prof. Dr. Kıvılcım Yüksel ALDOĞAN
Department of Electrical and Electronics Engineering, İzmir Institute of Technology

9 July 2013

_____   _____

Prof. Dr. Metin TANOĞLU   **Prof. Dr. Lütfi ÖZYÜZER**
Supervisor, Department of Mechanical   Co-Supervisor, Department of Physics,
Engineering, İzmir Institute of   İzmir Institute of Technology
Technology

_____   _____

Assoc. Prof. Dr. Mustafa M. DEMİR   **Prof. R. Tuğrul SENGER**
Head of the Department of Materials   Dean of the Graduate School of
Science and Engineering   Engineering and Sciences

ACKNOWLEDGMENTS

ABSTRACT

DEVELOPMENT OF RADAR-ABSORBING COMPOSITE STRUCTURES

Radar absorbing materials (RAMs) are dielectric or magnetic materials that has capacity for absorbing electromagnetic waves. In order to increase frequency range (bandwidth) of the absorbance, several structures have been already proposed by several researchers. Objective of this study is to design, fabricate and characterize RAMs based on glass fiber reinforced epoxy composites within 2-18 GHz frequency range.

For achieving radar wave absorbance, several structures such as Dallenbach layer, Salisbury screen and Jaumann absorber were designed and manufactured from polymeric composites. Glass fiber / epoxy system were employed as a base structure. Carbonyl Iron based powders were used as a filler for electromagnetic wave absorber in epoxy matrix. In Salisbury screens and Jaumann absorbers resistive sheets are used to increase the bandwidth of absorbance. Glass fabric surfaces were cotaed with thin layer of metallica conductor with surface resistances up to 1000 Ω to act as a resistive layers within the composite structure. Coatings were done by a large scale magnetron sputtering unit. Resulting structures achieve 12 dB reflection loss with thicknesses varies from 2.65 to 3.15 mm and the resonant frequency detected as 7 GHz.

Since in many applications composites are implemented into vehicles and structures such as aircraft wings and wind turbine blades, the purpose of Radar Absorbing Sturctures (RAS) is not only increase the bandwidth of absorbance, but also to serve as a structural element in which. For this reason, structural and physical performance of RAMs has been one of great importance. In this study, mechanical and thermomechanical properties of developed RAMs were also characterized to evaluate the structural performances. It is observed that, addition of carbonyl iron affected the mechanical properties due to lack of binding with epoxy matrix. This effect can be clearly seen at tensile and impact properties that up to 30% losses were observed.

ÖZET

RADAR ABSORBE EDEN KOMPOZİT YAPILARIN GELİŞTİRİLMESİ

Radar soğurabilen malzemeler (RSM)ler dielektrik veya manyetik malzemeler olup, elektromanyetik dalgaları soğurma özelliğine sahiptir. Soğurma frekans aralığını (bant genişliğini) arttırmak için değişik araştkırmacılar tarafından belli sayıda yapılar önerilmiştir. Bu çalışmanın amacı 2-18 GHz frekans aralığında cam elyaf takviyeli epoksi kompozit esaslı Radar Soğurabilen Malzemeler (RSM)lerin tasarımı, üretimi ve karakterizasyonudur.

Radar dalgalarının soğurulmasının başarılabilimesi için Dallenbach katmanı, Salisbury ekranı ve Jaumann soğurucusu gibi belli özel yapılar polimerik kompozitlerden tasarlanmış ve üretilmiştir. Cam fiber / epoksi sistemi temel yapı olarak kullanılmıştır. Karbonil demir esaslı tozlar epoksi matriksinin içinde elektromanyetik dalga soğurucu katkı olarak kullanılmıştır. Salisbury ekranları ve Jaumann soğurucularında soğurma bant genişliğini artırmak için direnç katmanları kullanılmaktadır. Cam elyaf yüzeyleri kompozit yapı içinde 1000 Ω yüzey direncine kadar direnç katmanı görevi görmek amacıyla ince metalik iletken katmanı ile kaplanmıştır. Kaplamalar, büyük ölçekli manyetik saçtırma ünitesi ile yapılmıştır. Ortaya çıkan yapılar 2.65 ve 3.15 mm arasında kalınlıklara sahip olup, 7 GHz'de rezonant frekansı tespit edilmişt ve 12 dB'e kadar yansıma kayıpları elde edilmiştir.

Uçak kanadı veya rüzgar türbini pervanesi gibi bir çok uygulamada kompozitler araç ve yapıların içine yapısal eleman olarak entegre edildiğinden, Radar Soğurabilen Yapılar (RSY) sadece soğurma bant genişliğini arttırmak için değil, aynı zamanda uygulandığı aracın veya platformun bir elemanı olarakta işlevsellik göstermesi beklenebilir. Bu nedenle radar soğurucu malzemelerin yapısal ve fiziksel performansları önem taşıyabilmektedir. Bu çalışmada geliştirilen RSM'lerin aynı zamanda mekanik ve termomekanik özellikleri de karakterize edilerek yapısal performansları da değerlendirilmiştir. Mekanik analizler sonucunda, karbonil demirin yapıya eklenmesi mekanik özellikleri düşürmektedir. Bunun nedeni olarak karbonil demirin epoksi matriks ile bağlanmamasından kaynaklandığı düşünülmektedir. Özellikle çekme ve darbe özelliklerinde %30'lara varan kayıplar gözlemlenmiştir.

TABLES OF CONTENTS

LIST OF FIGURES

LIST OF TABLES

CHAPTER 1

INTRODUCTION

Radar is a method for detecting the position and velocity of a distant object, such as an aircraft. Detection is achieved by analyzing the response of high frequency radio waves reflected from the target object. The term *RADAR* was coined in 1940 by the United States Navy as an acronym for *RA*dio *D*etection *A*nd *R*anging (Eugene F Knott, Shaeffer, and Tuley 2004). The term not only refers to the detection method, but also refers to the detection system itself.

Despite being found out as a military technology to detect enemy aircraft, nowadays radar technology serves many purposes to humankind. Notable examples include, air, marine and ground traffic control and navigation, short-term weather forecasting and specialised ground-penetrating radars for mapping the composition of Earth's crust (Hill 2007). Nevertheless, radar is still a very crucial technology for military applications.

Radar systems are based on transmitting and recieving radio waves which are electromagnetic waves between wavelengths of 1 mm to 100,000 km. Analyzing the response of the transmitted electromagnetic waves gives information about position, velocity, magnitude and type of the object. The object can be identified from its radar cross section (RCS) which is a footprint of the object in the radar system (Jenn 2005). Infomation gained from radar systems are very valuable for the course of military operations, thus giving enourmous advantage to the side which has proper radar systems.

As radar systems came into use, research for reducing the effectiveness of these systems were also began. Research generally focused on reducing the amount of electromagnetic waves reflected from the object by absorbing transmitted waves, achievable through using proper materials and design. These materials defined as Radar Absorbing Materials (RAMs).

Interest at radar absorbing materials and structures began immediately with the discovery of radar systems at World War II. One of the first applications was the using of carbon based radar absorbing materials on submarine periscobes which was

developed by Jaumann. But this attempt was greatly reduced by the effect of sea water on the material (Hepcke 2007)

In 1971, Naito and Suetake were studied on electromagnetic wave absorber composed of ferrite powder and rubber matrix. The study also investigated the existence of matching frequency, thickness of the RAM for maximizing the bandwith (Naito and Suetake 1971).

In early 80s, the development of RAM was generally based on ferrites or carbonyl iron. First implementation of RAMs was on military applications. One of them was utilized in the development of F-117 Nighthawk, which made its maiden flight in 1981. The aircraft had a paint type absorber, based on both ferrites and carbon particles. In 1983, F-117 fleet was ready for operations for U.S. Air Force. In 1988, the aircraft was announced to public as a "stealth fighter". The ability of radar wave absorbing generally denoted as "stealth" or "stealth technology" by military and quickly adapted by public (Eugene F Knott, Shaeffer, and Tuley 2004).

In late 80s, interest for RAMs greatly increased. Knott, Shaeffer and Tuley had written a book about radar cross section which was a concept of footprint of the object exposed to radar waves. Their work also included reducing of RCS, which refers RAMs but also size and shape of the object (Eugene F Knott, Shaeffer, and Tuley 2004).

In general, early works on RAMs and Radar Absorbing Structures (RASs) were consist of theoretical calculations, simulations and optimizations due to limitations to synthesize the material itself. Studies on Jaumann type absorbers in late 80s and early 90s can be given as an example in which contains simulations and optimizations for resistive sheet configurations and their resistances (Du Toit and Cloete 1989; du Toit and Cloete 1990; Chambers and Tennant 1996; E.F. Knott and Lunden 1995; Chambers and Tennant 1994).

RAM studies have been generally based on 0° degree (direct approach) angle of incidence. There were also studies about the performance of RAMs for wide range of angles of incidence. These works indicated that the angle of incidence of radar wave greatly effects the performance. With increasing angle of incidence until 60° reflection coefficient may even increase. However, it was found that above 60°, those value drops significantly (Perini and Cohen 1991; Perini and Cohen 1993).

In early 2000s, studies on lossy RAMs were increased. Both ferrimagnetic based and carbon based dielectric materials were investigated. Carbonyl iron and ferrite powders such as barium hexaferrite have been popular as magnetic RAMs (Pinho et al.

2002; S. Kim, Yoon, and Kim 2003; Meshram et al. 2004). Studies on dielectric absorbents gained more interest at mid 2000s. These RAMs include graphite, carbon black, single and multi-walled carbon nanotubes, carbon nano fibers which were mixed with epoxy, rubber or silicone matrix (Oh et al. 2004; Rosa et al. 2010; Ki-Yeon Park et al. 2009)

Radar systems generally operates at certain segments of electromagnetic spectrum such as X-band which includes frequencies from 8.2 GHz to 12.4 GHz. (Hill 2007) Thus, absorption of the waves at certain bands can be achievable but more complex materials or designs are needed to prevent all the waves throughout a band reflected. There were additional studies to increase the bandwidth of absorption below certain attuneation (-10 or -20 dB) beyond X-band. These studies focused on broadband absorbers generally aims for combination of X and K_u band or a wider 2-18 GHz range (Gama and Rezende 2010; Zhang et al. 2006; S. Kim, Yoon, and Kim 2003; Y. C. Qing et al. 2010). The electromagnetic spectrum with radio, microwave and visible light spectrums detailed, is illustrated in Figure 1.1.
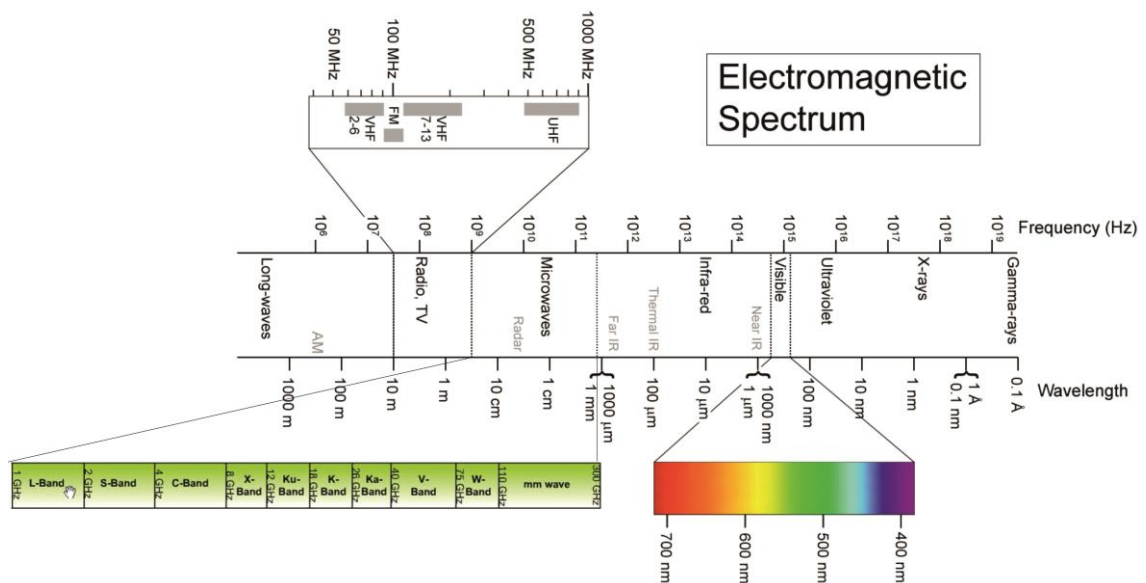
Figure 1.1. Illustration of electromagnetic wave spectrum

Recent studies concentrate on Radar Absorbing Structures (RAS), which are a combination of RAM and structural design to increase bandwidth and decrease attuneation. Structures have been based on sandwich type structures or continous fiber reinforced composites. Designs were based on single or multilayer Dallenbach layers

3

which consist a combination of lossy materials (D. Micheli et al. 2010), Salisbury screen which is basically a Dallenbach layer including a resistive sheet (S. Kim, Yoon, and Kim 2003) and Jaumann absorbers which include multiple resistive sheets to increase bandwidth (Ke et al. 2011; Hashimoto et al. 1995).

One of the important advantage of RAS designs is that they are applicaple to several current structures used for vehicles or constructions. Laminated composites and sandwich structures are suited examples for that usage. Vehicle parts such as aircraft wings, or wind turbine blades can be manufactured from materials such as fiber reinforced composites for both structural integrity and radar absorbing properties (Motevasselian 2010; McDonald et al. 2012).

The main objective of this study is to develop radar absorbing materials based on laminated fiber reinforced polymeric composites. For this purpose, RAS designs; Dallenbach layer, Salisbury screen and Jaumann absorber are considered and their performance theoratically calculated and optimized. Laminated glass fiber / epoxy composites were manufactured based on aforementioned designs. The radar absorbing performance of those manufactured structures are measured and compared with the calculated theoretical values. Also, for te evaluation structural integrity of the developed RAS, mechanical and thermomechanical properties are characterized and compared with unmodified composite structures.

CHAPTER 2

RADAR ABSORBING STRUCTURES

Radar wave absorbers are materials or structures that can soak up incident energy and reduce the energy reflected back to the radar. It's main objective is to achieve reduction in the radar cross section (RCS) of radar targets.

Reducing the electromagnetic waves that are reflected can be achievable by several phenomena including shaping of the vehicle or structure to scatter incoming radio waves, absorbing of the electromagnetic waves by absorbent materials and absorbing structures that capable of imprisoning incident waves into the structure thus increasing the absorption by absorbent material and increasing absorption by cancellation at interfaces (Barton and Leonov 1997; Seo, Chin, and Lee 2004). Understanding of these phenomena is crucial in radar absorbing structure development and design.

2.1. Shaping

The objective of shaping is to orient the target surfaces and edges to deflect the scattered energy in directions away from the radar. This cannot be done for all viewing angles within the entire sphere of solid angles because there will always be viewing angles at which surfaces are seen at normal incidence, and there the echoes will be high (Eugene F Knott, Shaeffer, and Tuley 2004).

All modern military air and surface platforms incorporate some aspect of shaping in their designs. Most known examples are the F-117 Nighthawk and B-2 Spirit bomber aircraft, shown in Figure 2.1. Neither aircraft has the standard vertical and horizontal tail surfaces.
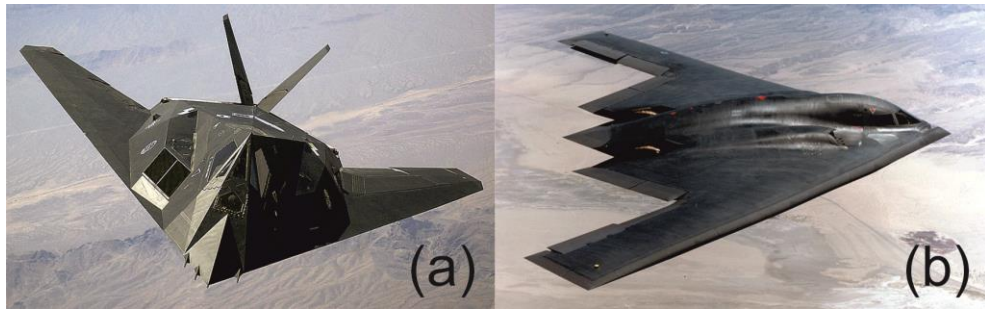
Figure 2.1. Photographs of first generation stealth aircraft. (a) F-117 Nighthawk and (b) B-2 Spirit (Source: "Lockheed F-117 Nightawk", "Northrop Grumman B-2 Spirit", Wikipedia, Wikimedia Foundation, Inc.)

Many stealthy aircraft shapes are aerodynamically unstable; they achieve their high performance and stability through computer control (Eugene F Knott, Shaeffer, and Tuley 2004). The latest generation of fighter aircraft such as F-22 Raptor, F-35 Lightning II and Eurofighter Typhoon shown in Figure 2.2 is incorporating at least some stealth shaping features.

Figure 2.2. Photographs of lastest generation aircraft. (a) F-22 Raptor, (b) F-35 Lightning II and (c) Eurofighter Typhoon (Source: "Lockheed Martin F-22 Raptor", "Lockheed Martin F-35 Lightning II", "Eurofighter Typhoon" Wikipedia, Wikimedia Foundation, Inc.)

Shaping principles have been applied to ships as well (Jenn 2005; Eugene F Knott, Shaeffer, and Tuley 2004; Folgueras, Alves, and Rezende 2010). The United States Navy's Sea Shadow show in Figure 2.3 (a), demonstrated the feasibility of shaping for ocean going vessels. Stealth and signature control are high priorities in the design of the next generation of warships such as U.S. Zumalt-class destroyers which are still in production (Figure 2.3 (b)). Corner reflector RCS for corner angles of 90° and 110° of currently deployed stealth-inspired ships include the Swedish Visby and the French LaFayette shown in Figure 2.3 (c) and (d) respectively.
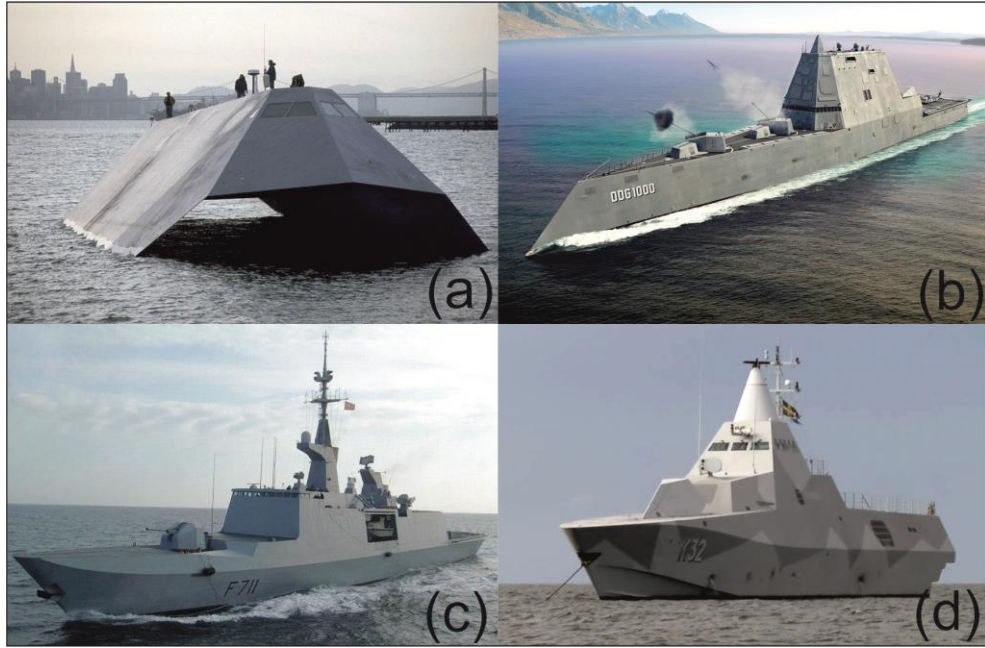
Figure 2.3. Photographs of lastest generation sea vessels. (a) US Navy Sea Shadow, (b) US Zumalt-class Destroyer (c) La Fayette class French frigate and (d) Swedish Navy's Visby-class corvette (Source: "Sea Shadow (IX-529)", "La Fayette-class frigate", "Visby-class corvette" Wikipedia, Wikimedia Foundation, Inc.)

2.2. Absorbing Materials

Most important aspect of a radar wave absorption or an electromagnetic wave absorption is to soak up the incident electromagnetic energy, thereby reducing the net energy available for reflection (Barton and Leonov 1997). In order to absorb energy, each material layer must act as much like a resistor in a simple electric circuit and the energy absorbed from the incident electromagnetic wave dissipated into heat.

Permittivity and permeability are material properties that define dielectric and magnetic behaviour of the material, respectively (Gama and Rezende 2010). Permittivity is a measure of how an electric field affects a dielectric medium. Permeability is the degree of magnetization that a material obtains in response to an applied magnetic field. Both properties can be expressed as in Equation 2.1 and 2.2 respectively.

$$\varepsilon = \varepsilon_0 \varepsilon_r = \varepsilon_0 (\varepsilon'_r - j\varepsilon''_r) \tag{2.1}$$

$$\mu = \mu_0 \mu_r = \mu_0 (\mu'_r - j\mu''_r) \tag{2.2}$$

Dielectric permittivity (ε) can be defined as relative permittivity of the material (ε_r) to the permittivity of vacuum ($\varepsilon_0 = 8.8541878175 \; x \; 10^{-12} \; F/m$). Relative permittivity can be decomposed into real and imaginary parts (ε_r' and ε_r'') that can be measured.

Similar to permittivity, magnetic permeability (μ) can be defined as relative permeability (μ_r) of the material to the permeability of free space ($\mu_0 = 4\pi \; x \; 10^{-7} \left(\frac{N}{A^2}\right) \cong 1.2566370614 \; x \; 10^{-6} \; H/m$). Again, relative permeability can be decomposed into real and imaginary parts (μ_r' and μ_r'') that can be measured.

First absorber designs were based on perfect materials that ε_r and μ_r are considered as positive integer numbers but in real applications, all materials behave as a lossy medium. Some materials may have dominant dielectric or magnetic properties but these properties may change significantly with changing frequency of the incident wave. So, real and imaginary parts of permittivity and permeability can be measured in frequency domain and designs based on measurements became more consistent with real life conditions (Jenn 2005; K.-Y. Park et al. 2011).

Absorbant materials generally have a particulate form and these particulate materials act as filler in a matrix which generally composed of rubber, silicone, or thermoset resin (K.-Y. Park et al. 2011; Lee, Kang, and Kim 2006; Y. Qing et al. 2009; Xu et al. 2013; Y. Qing et al. 2010). There are mainly two types of particulate absorbers; carbon based absorbers have dominant dielectric properties compared to nearly steady permeability in frequency domain and magnetic absorbers, which have significant magnitude of relative permeability compared to dielectric absorbers.

2.2.1. Carbon Based Absorbers

Carbon was the basic material used in the fabrication of early absorbers because of its imperfect conductivity, and it continues to be important today (Eugene F Knott, Shaeffer, and Tuley 2004). The unique structure and excellent properties of carbon nano structures has prompted intensive study for radar absorbing applications. Most used carbon based absorbers are graphite, carbon black, single and multi-walled carbon nanotubes, short carbon fibers, carbon nano fibers (Oh et al. 2004; Rosa et al. 2010; D. Micheli et al. 2010). These materials are microwave lossy materials that have been characterized in terms of the electrical permittivity, which describes the interaction of a

material with an electric field and in general is a complex quantity (ε) which is shown in Equation 2.1.

According to the theory of complex permittivity, when an electromagnetic field propagates within a dielectric material, the electric field induces two types of electrical effects, which are conduction and displacement currents. The effect of conduction current gives rise to power loss, which is related to the imaginary permittivity (ε_r''), the interaction with displacement current induces the polarization effect, which is described by the real permittivity (ε_r'). Therefore, an increase of the real part of the complex permittivity can be mainly ascribed to dielectric relaxation and space charge polarization effect, whereas an increase of the imaginary part of the complex permittivity can be attributed to the enhanced electrical conductivity of the material (D. Micheli et al. 2010; Davide Micheli 2011).

Carbon based absorbers generally tend to have very low densities and their mixing ratios are very low in comparison with those of the magnetic absorbers. In turn they require more thickness to be resonant in radar wave frequencies (Barton and Leonov 1997).

2.2.2. Magnetic Absorbers

Magnetic materials that are capable of absorbing electromagnetic wave mostly based on iron, iron oxides, cobalt, nickel, manganese and zinc (Eugene F Knott, Shaeffer, and Tuley 2004; Y. Qing et al. 2009; Y. B. Feng, Qiu, and Shen 2007). The two most common materials used as magnetic RAM are carbonyl iron and iron oxide based ferrites (Meshram et al. 2004; Y. Feng et al. 2006).

The loss mechanism is primarily due to a magnetic dipole moment. Some ceramics exhibit a permanent magnetization, termed ferrimagnetism which is defined as magnetism with unbalanced antiparallel magnetic alignment (Jenn 2005). From the point of view of electrical properties, these materials are semiconductors or insulators, in contrast to metallic magnetic materials which are electrical conductors (Eugene F Knott, Shaeffer, and Tuley 2004).

The important ferrites are the hexaferrites or M-type ferrites, characterized by the compound $MeFe_{12}O_{19}$, where Me can be substituded as barium, strontium or lead. M

type ferrites are widely used as permanent magnet materials (Meshram et al. 2004; Parida, Singh, and Agarwal 2007).

Magnetic materials offer the advantage of compactness because they are typically a fraction of the thickness of dielectric absorbers. However, magnetic absorbers are heavy because of their iron content and mostly used at high mixing ratios, so that most of the magnetic absorbers have high aerial weight (Meshram et al. 2004; J. Kim, Lee, and Kim 2008).

2.2.3. Conductive Polymers

In a polymer such as polypyrrole (PPy) or polyaniline (PAN), partial oxidation of the polymer (doping) causes it to become conducting through the formation of polarons and bipolarons; the charge carriers along the chains (Tong 2009). The conductivity of a conducting polymer is modelled by phonon assisted hopping between the randomly distributed localized states (that result from the partial oxidation) (Stenger-Smith 1998).

One of the problems with conducting polymers is that they are typically difficult to manage and shape (Tellakula et al. 2004). Formation of composites with thermoplastic or thermoset materials is a solution for improving processibility. Deposition on fabric materials is another method. Textile materials have been used as substrates for a number of materials and have been coated with conducting polymers by soaking them with oxidant and then exposing them to monomer (Tellakula et al. 2004; Malinauskas 2001; Marchant et al. 1998).

Polypyrrole by itself does not have great physical properties and so most of the useful materials are composites of polypyrrole and other materials such as latex, fibres or polymer blends (Tellakula et al. 2004). Polypyrrole finds great use due to its relative stability in air.

2.3. Absorbing Structures

Radar absorbing structures are promising topic for avoiding radar detection. RASs are capable of both load bearing and electromagnetic energy absorbing. Thus they

don't interfere with the external profiles set by the designers unlike shaping and paint/dye type absorbers. This structures can be expressed, modelled and optimized by electromagnetic theory and using circuit analogy (Eugene F Knott, Shaeffer, and Tuley 2004).

The reflection of electromagnetic radiation from the surface of any material can be calculated from Maxwell's equations if the electromagnetic properties are known (Hill 2007). As mentioned before the relevant properties are the magnetic permeability μ and the dielectric permitivitty ε. Both μ and ε may be expressed as complex numbers, in which case the imaginary part represents the magnetic loss or dielectric loss, respectively. These parameters in turn define the characteristic or intrinsic impedance η, given by Equation 2.3, and the propagation coefficient β, given by Equation 2.4 (D. Micheli et al. 2010).

$$\eta = \sqrt{\frac{\mu}{\varepsilon}} = \sqrt{\frac{\mu_0}{\varepsilon_0}}\sqrt{\frac{\mu_r}{\varepsilon_r}} = Z_0 \sqrt{\frac{(\mu_r' - j\mu_r'')}{(\varepsilon_r' - j\varepsilon_r'')}} \tag{2.3}$$

$$\beta = j2\pi f \sqrt{\mu\varepsilon} = j2\pi f \sqrt{\mu_0\varepsilon_0}\sqrt{\mu_r\varepsilon_r} \tag{2.4}$$

$$\beta = j2\pi f \sqrt{\mu_0\varepsilon_0}\sqrt{(\mu_r' - j\mu_r'')(\varepsilon_r' - j\varepsilon_r'')} \tag{2.5}$$

In Equation 2.3, Z_0 is the impedance of free space which equals to 377 Ω. f is frequency of the propagating wave and j is the complex number $\sqrt{-1}$. In the case of radar absorbing materials, the objective is to minimize the reflection by matching the input impedance Z_n of the last (n[th]) material layer to the characteristic impedance Z_0 of free space (Davide Micheli 2011; S. Kim, Yoon, and Kim 2003). A generalized input impedance can be defined as in Equation 2.6.

$$Z_i = \eta_i \frac{Z_{i-1} + \eta_i \tanh(\beta_i t_i)}{\eta_i + Z_{i-1} \tanh(\beta_i t_i)} \tag{2.6}$$

In this equation, t_i is the thickness of ith material layer. The energy reflection coefficient or reflection loss, Γ is given by expression;

$$\Gamma = 20log_{10} \left| \frac{Z_n - Z_0}{Z_n + Z_0} \right| \tag{2.7}$$

11

Zero reflection will occur in the case where Z_n is equal to Z_0. In the simple case where the attenuation in the material is such that there is no reflected energy from the conducting surface, the hyperbolic tangent (tanh) function in Equation 2.6 tends to unity and the only reflection is at the free-space/material interface. This condition must be met for μ and ε as complex numbers. Since either μ or ε must contain an imaginary component in order to attenuate the radiation, it necessarily follows that in this case both μ and ε must be complex numbers with both the real parts and imaginary parts in the same ratio as the ratio of μ_0 and ε_0.

Considering these equations, several types of structures were proposed that can increase the absorbance of radar waves. Most important of these structures can be named as Dallenbach layers, Salisbury screen, Jaumann absorbers and Circuit Analaog absorbers (Eugene F Knott, Shaeffer, and Tuley 2004; Jenn 2005).

2.3.1. Dallenbach Layer

A Dallenbach layer is a homogeneous absorber layer backed by a conducting plate. The desing variables of a dallenbach layer consists of thickness of the layer, permittivity and permeability of the material used.
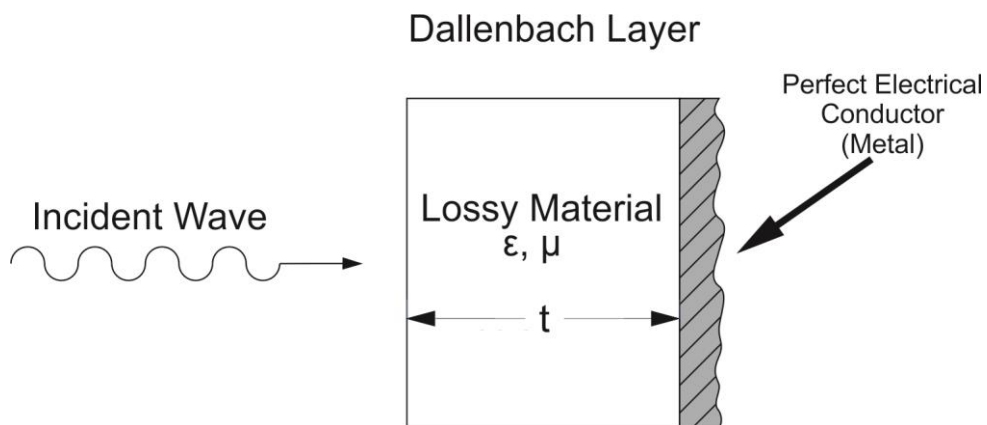
Figure 2.4. Schematic illustration of a Dallenbach layer

For reflectivity to result in a minimum, the effective impedance of the layer, must equal the incident impedance Z_0. Considering Equation 2.6 and Figure 2.4, Z_{i-1}

denotes the impedance of perfect electrical conductor (metal) surface (Z_{PEC}) and equals to 0 Ω so Equation 2.8 can be reduced as in Equation 2.9

$$Z_i = \eta_i \frac{Z_{PEC} + \eta_i \tanh(\beta_i t_i)}{\eta_i + Z_{PEC} \tanh(\beta_i t_i)} \tag{2.8}$$

$$Z_i = \eta_i \tanh(\beta_i t_i) \tag{2.9}$$

However, since Z_i is complex and Z_0 real there is a requirement that the sum of the phase angles in Z_i and $\tanh(\beta_i t_i)$ is zero (destructive interference) and the product of their magnitudes is equal to Z_0.

Dallebach layers can also be considered as multilayer structures (D. Micheli et al. 2010). So impedances can be calculated in series from Z_1 to Z_n. Different materials or same materials with different concentrations can be used in multilayer Dallenbach layers. The key point is, interface between two layers must be perfect without any voids.

2.3.2. Salisbury Screen

The Salisbury Screen is also a resonant absorber, however, unlike the Dallenbach absorbers it does not solely rely on the permittivity and permeability of the bulk layer. The Salisbury Screen consists of a resistive sheet placed in front of a conducting metal backing usually separated by an air gap, foam or a lossy bulk material. This decreases the required gap thickness at the expense of bandwidth (Eugene F Knott, Shaeffer, and Tuley 2004). A schematically illusrated Salisbury screen is shown in Figure 2.5.

In terms of transmission line theory, the quarter wavelength transmission line transforms the short circuit at the metal into an open circuit at the resistive sheet. The effective impedance of the structure is the sheet resistance. (If the gap is a half wavelength then the short circuit reappears and perfect reflection occurs). If the sheet resistance is 377 ohms/square (Z_0, the impedance of air), then good impedance matching occurs (S. Kim, Yoon, and Kim 2003). An analogue of the electrical screen would be to place a magnetic layer on the metal surface, resulting in a thinner device.
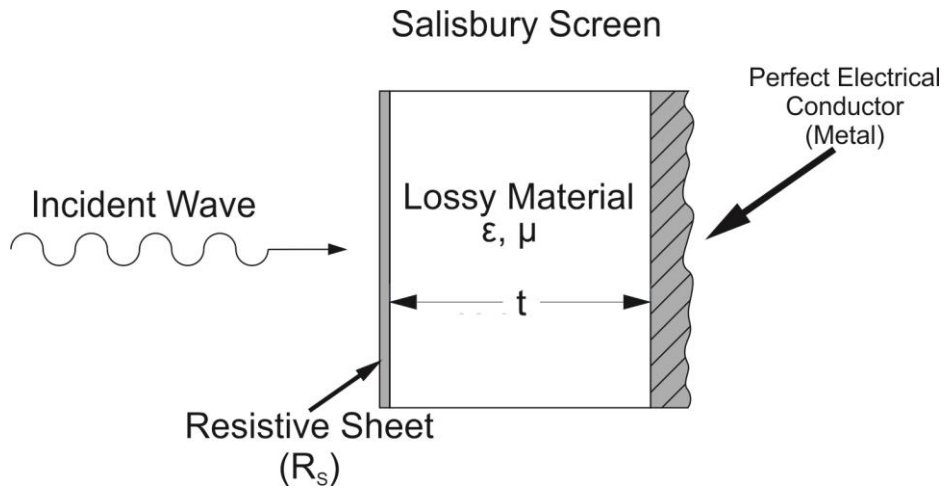
Figure 2.5. Schematic illustration of a Salisbury screen

2.3.3. Jaumann Absorbers

Jaumann absorbers are using a method of increasing the bandwidth of the Salisbury screen, the simplest form of a Jaumann absorber. Additional resistive sheet layers found out be increase the bandwidth by forming more than one minima in the reflectivity (Eugene F Knott, Shaeffer, and Tuley 2004; E.F. Knott and Lunden 1995; du Toit and Cloete 1989). Correctly placed resistive sheets in the structure can increase the bandwith of absorbance significantly. Multilayer Jaumann devices consisting of low loss dielectric sheets separating poorly conductive sheets. The effect of additional resistive sheets in the reflectivity is shown in Figure 2.6. As it can be clearly seen, additional resistive sheets create additional resonant frequencies, thus increasing bandwidth.
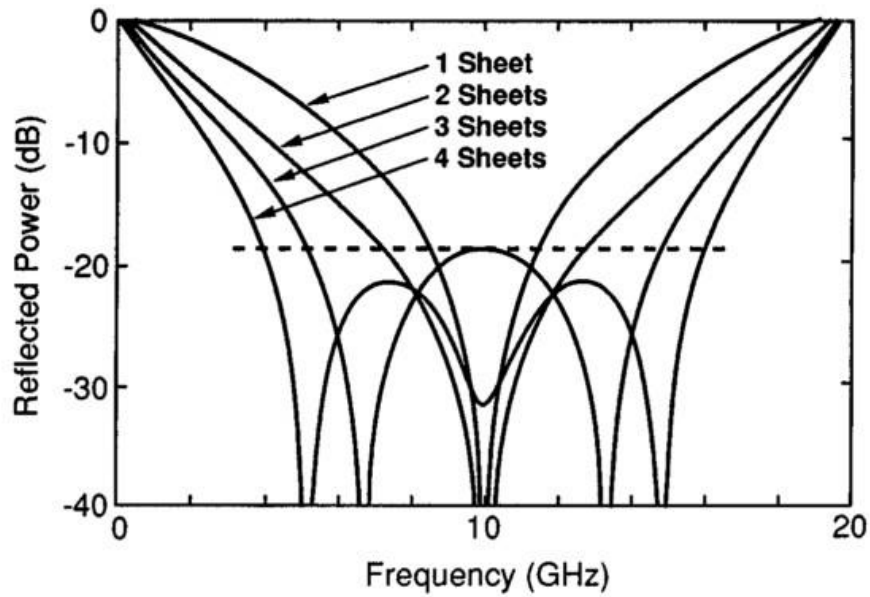
Figure 2.6. Comparison of additional resistive sheets effect on reflectivity
(Source: Eugene F Knott, Shaeffer, and Tuley 2004)

Optimization of Jaumann absorbers is complex due to the number of parameters involved, which increase as the number of layers increase. Empirical procedures and numerical optimization techniques have been used for designing Jaumann absorbers (Du Toit and Cloete 1989; du Toit and Cloete 1990; E.F. Knott and Lunden 1995; Perini and Cohen 1991). A Jaumann absorber containing two resistive sheet is schematically illustrated in Figure 2.7.
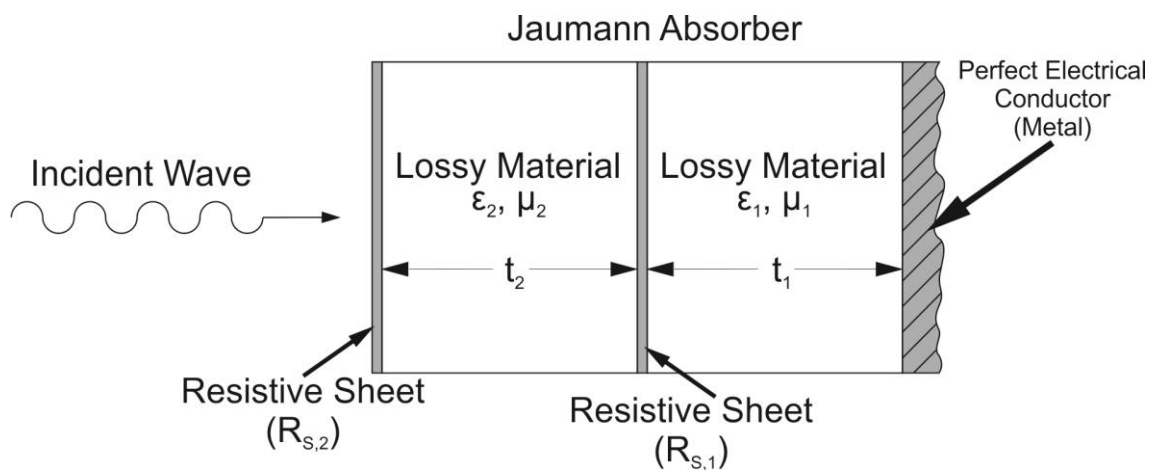
Figure 2.7. Schematic illustration of a Jaumann absorber

2.3.4. Frequency Selective Surfaces and Circuit Analog Absorbers

Frequency selective surfaces (FSSs) are two-dimensional periodic structures that consist of metallic patch elements printed on a thin dielectric layer or aperture elements within a metallic screen (Munk 2000). FSSs basically are filters that transmit or reflect electromagnetic waves at chosen frequency bands. Gangbuster dipole, multi pole, ring, polygon loops, and cross are some examples for FSS element geometry (Munk 2000). Some these element geometries are shown in Figure 2.8. The size and geometry of the element are chosen to fit the desired overall frequency response of the structure. Planar and curved FSS have been used for a variety of applications including antenna radome design dichroic surfaces for reflectors and sub-reflectors of large aperture antennas or even radar absorbers (Barton and Leonov 1997).
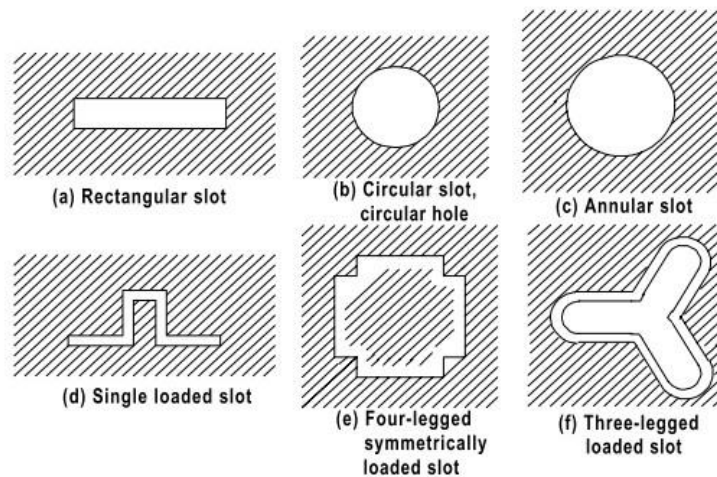
Figure 2.8. Examples of patterns for frequency selective surfaces
(Source: Barton and Leonov 1997)

Circuit analog (CA) absorbers are sheets of low-loss material on which specific conducting patterns have been deposited on the surface of the sheet. The patterns constitute resistance, inductance, and capacitance. The deposited film can be represented by an equivalent circuit, parameters of which can be controlled by the geometric configuration, film thickness, and conductivity of the deposition on the film (Barton and Leonov 1997).

2.3.5. Pyramidal Structures

Pyramidal absorbers are typically thick materials with pyramidal or cone structures extending perpendicular to the surface in a regularly spaced pattern. These type of absorbers are also called as geometric transition absorber. Pyramidal absorbers were developed so that the interface presents a gradual transition in impedance from air to that of the absorber. The height and periodicity of the pyramids tend to be on the order of one wavelength. The disadvantage of pyramidal absorbers is their thickness and tendency to be fragile. They are usually used for anechoic chambers (Eugene F Knott, Shaeffer, and Tuley 2004; Barton and Leonov 1997).
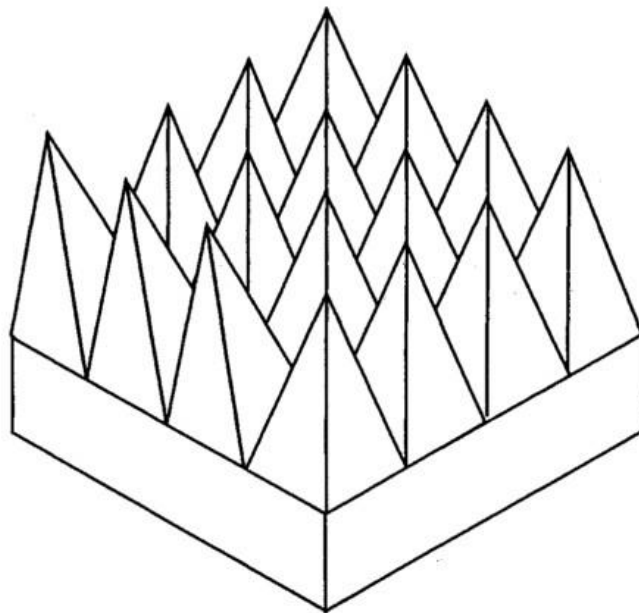
Figure 2.9. Schematic illustration of a pyramidal structure
(Source: Eugene F Knott, Shaeffer, and Tuley 2004)

2.4. Optimization of Radar Absorbing Structures

Optimization is the act of obtaining the best result under given conditions. The ultimate purpose in design of any engineering system is either to minimize the effort required or to maximize the desired benefit. Since the effort required or the benefit anticipated in any practical situation can be expressed as a function of certain decision

variables, optimization can be defined as the process of finding the conditions that give the maximum or minimum value of a function (Haupt and Haupt 2004).

There are several optimization techniques available such as genetic algorithm (GA) optimization, particle swarm optimization (PSO), Taguchi methods and optimization by finite element method. In the case of radar absorbing materials and structures, genetic algorith is one of the popular optimization methods and widely used in literature (Davide Micheli 2011; Guan et al. 2003; Michielssen et al. 1993; Chambers and Tennant 1996; Foroozesh, Cheldavi, and Hodjat 2000).

Genetic Algorithm (GA) is a stochastic global optimisation routine loosely based on Darwin's theory of evolution and genetics. An evolutionary process arrives at the optimized solution over several iterations (generations), by selecting only the best (the fittest) solutions and allowing these to survive and form the basis for calculating the next round of solutions. In this manner the optimization routine evolves the initial solutions into the optimum (Sivanandam and Deepa 2007).

Broadband absorbers such as Jaumann absorbers are based on multilayer stacks of resistive sheets separated by lossy bulk materials. As mentioned before, wider absorption bandwidths can be obtained by using more sheets. The reflectivity from a multilayer absorber is non-linear and cannot be analytically solved beyond one or two layers (Du Toit and Cloete 1989; E.F. Knott and Lunden 1995).

Complexity of the structures thus design variables increases from Dallenbach layer to Jaumann absorbers. In the case of Jaumann absorbers, as material layer resistive sheet pairs increase, design variable also increase for that each layers ε, μ, thickness, resistive sheet resistance should be taken into account. Thus optimization algorithms are needed for optimum solutions.

2.4.1. Genetic Algorithm Optimization

Genetic Algorithm (GA) is based on a natural selection process which ends up with the evolution of organisms best adapted to the environment. Genetic algorithm begins its search with a population of random individuals. Each member of the population holds a chromosome which encodes certain characteristics of the individual. The algorithm methodically analyzes each individual in the population of designs according to set specifications and assigns it a fitness rating which represents the

designer's aims. This fitness rating is then used to identify the structural designs which perform better than others. Thus, it enables the genetic algorithm to determine the designs which are weak and must be eliminated using the reproduction operator. After this step, the remaining, more desirable genetic material is utilized to create a new population of individuals. This part is carried out by applying two more operators similar to natural genetic processes, which called gene crossover and gene mutation. The process is iterated over many generations in order to obtain optimal designs (Sivanandam and Deepa 2007). A flowchart summarizing the process of genetic algorithm is shown in Figure 2.10.
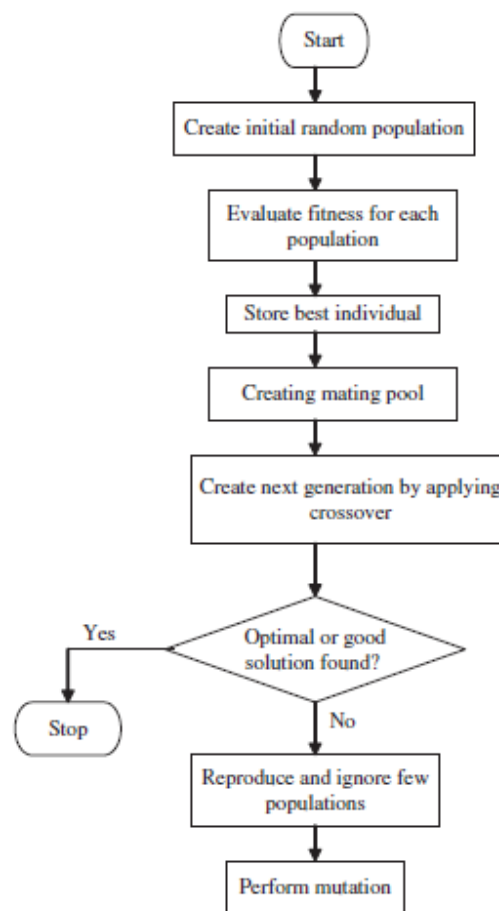
Figure 2.10. Genetic Algorithm flowchart
(Source: Sivanandam and Deepa 2007)

As the evolutionary algorithm technique, GA provides important benefits over traditional gradient based optimization routines, such as nominal insensitivity to problem complexity and the ability to discover easily global optimum rather than local optima (Sivanandam and Deepa 2007).

19

The basic terminologies used in GA to obtain a good enough solution for possible terminating conditions need to be defined at this point. The two distinct elements in the GA are individuals and populations. An individual is a single solution while the population is the set of individuals currently involved in the search process. Individual includes two forms of solutions. They are the chromosome, which is the raw genetic information (genotype) that the GA deals and the phenotype, which expresses the chromosome in the terms of the model. A chromosome includes subsections of genes. A gene is the GA's representation of a single factor for a control factor. Each factor in the solution set corresponds to gene in the chromosome (Gen and Cheng 2000).

The fitness of an individual in a genetic algorithm is the value of an objective function for its phenotype. For calculating fitness, the chromosome has to be first decoded and the objective function has to be evaluated. The fitness not only specifies how good the solution is, but also corresponds to how close the chromosome is to the optimal one (Gen and Cheng 2000).

2.5. Manufacturing of Radar Absorbing Structures

Radar absorbing structures mentioned earlier are theoretical structures that can immensely increase the bandwidth of absorbance. But in real life conditions, there are some difficulties with manufacturing, especially when complexity of the structure increases.

Dallenbach layers are generally easier to manufacture, most of the paint type absorbers falls into this category, with single layer or perfectly binded multi layer structures consists of rubber or silicone matrix with magnetic or dielectric fillers are basically particulate composite structures and widely investigated in literature (D. Micheli et al. 2010; K. Park et al. 2006; Oikonomou, Giannakopoulou, and Litsardakis 2007).

Salisbury screens and Jaumann absorbers contain resistive sheets which are greatly increase the absorbance, but implementing these sheets into the structure still remains an imporant obstacle for real life applications. These structures began to be theoretically investigated in 1980s but only in 2000s studies about real life demonstrations emerged (Lederer 1992; S. Kim, Yoon, and Kim 2003). These studies

included sandwich structres, which resistive sheets were divided with spacer materials such as foams. Resistive sheets were also applied as metal coated thin films and integrated into polycarbonate spacers (Hashimoto et al. 1995).

Recently, wind turbine farm interference with radar installations were investigated. To prevent the noise generated by wind turbines, radar absorbing materials integrated into the polymeric composite structure of turbine blades were proposed (McDonald et al. 2012).

Similar to this study, optimizations based on aircraft wing profiles that were capable of radar wave absorbing were investigated (Motevasselian 2010). Proposed structure was an Jaumann absorber on an aircraft wing which can be integrated into fiber reinforced polymeric composites.

2.5.1. Polymeric Composites

A composite is a structural material that comprises of two or more components that are combined at macroscopic level and are not soluble in each other. One of the components is called the reinforcement and the other one which reinforcement is embedded into, called the matrix. The reinforcement may be in the form of continous fibers, short fibers, particles, or flakes.

Fiber-reinforced materials enable a better combination of strength and modulus as compared with many traditional metallic materials. Due to their low density, high strength and modulus, these composite materials are significantly superior to conventional materials. Furthermore, fatigue strength as well as fatigue damage tolerance of many laminated composites are pretty good. Therefore, fiber reinforced materials have come up as a major class of structural materials and they are considered for use as substitution for metals in many weight-critical components in aerospace, automotive, and other industries (Mallick 2007).

Table 2.1. Mechanical property comparison of most common reinforcement fibers
(Source: Campell 2003)

Fiber	Density Ib/in³	Tensile Strength (ksi)	Elastic Modulus (msi)	Strain to Failure (%)	Diameter (Mils)	Thermal Expansion Coefficient 10-6 in/in/ F
E-glass	0.090	500	11.0	4.8	0.36	2.8
S-glass	0.092	650	12.6	5.6	0.36	1.3
Quartz	0.079	490	10.0	5.0	0.35	1.0
Aramid (Kelvar 49)	0.052	550	19.0	2.8	0.47	−1.1
Spectra 1000	0.035	450	25.0	0.7	1.00	−1.0
Carbon (AS4)	0.065	530	33.0	1.5	0.32	−0.2
Carbon (IM-7)	0.064	730	41.0	1.8	0.20	−0.2
Graphite (P-100)	0.078	350	107	0.3	0.43	−0.3
Boron	0.093	520	58.0	0.9	4.00	2.5

Most common fiber reinforcements are glass, carbon, graphite and aramid. Each type of fiber reinforcement has its own advantages over other and used for suitable applications (Long 2005). A comparison between these fibers can be found in Table 2.1.

With good strength and modulus per cost ratio, glass fibers are the most abundant and relatively cost efficient type of fiber reinforcements (Campell 2003).

Carbon fibers are more often used in high-modulus and high-strength applications such as aircraft components, etc. The advantages of carbon fibers are high specific strength and modulus, low coefficient of thermal expansion, and high fatigue strength. The disadvantages are high cost, low impact resistance, and high electrical conductivity (Mallick 2007).

An aramid fiber is an aromatic organic compound made of carbon, hydrogen, oxygen, and nitrogen. The advantages of using aramid fiber are low density, high tensile strength, low cost, and high impact resistance. Its disadvantages are low compressive properties and degradation in sunlight. Kevlar 29® and Kevlar 49® are the two main types of aramid fibers. Both types of Kevlar fibers have similar specific strengths, but Kevlar 49 has a higher specific stiffness. Kevlar 29 is principally used in bulletproof vests, ropes, and cables. Kevlar 49 is used in high performance applications by the aircraft industry (Campell 2003).

Various polymers are used as matrix in polymeric composites. These polymers are epoxy, phenolics, acrylic, urethane, and polyamide and each polymer holds its advantages and disadvantages in its use (Campell 2003).

Table 2.2. Comparison of most commonly used resin systems
(Source: Campell 2003)

Polyesters	Used extensively in commercial applications. Relatively inexpensive with processing flexibility. Used for continuous and discontinuous composites.
Vinyl Esters	Similar to polyesters but are tougher and have better moisture resistance.
Epoxies	High performance matrix systems for primarily continuous fiber composites. Can be used at temperatures up to 250-275F. Better high temperature performance than polyesters and vinyl esters.
Bismaleimides	High temperature resin matrices for use in the temperature range of 275-350F with epoxy-like processing. Requires elevated temperature post cure.
Polyimides	Very high temperature resin systems for use at 550-600F. Very difficult to process.
Phenolics	High temperature resin systems with good smoke and fire resistance. Used extensively for aircraft interiors. Can be difficult to process.

Besides, each of the resin systems has its some advantages and disadvantages. The use of a particular resin system depends on the application. These considerations involve mechanical strength, cost, smoke emission, temperature excursions, resistance to corrosion etc (Mazumdar 2001). A summary of most commonly used resin systems can be found in Table 2.2.

2.5.2. Glass / Epoxy Polymeric Composite Systems

Glass / epoxy systems are cost efficient, high strength and modulus structures.that are widely used in industry, from aerospace applications to protective equipments.

As mentioned before, glass fibers are one of the most commonly used reinforcement materials in the industry. The main types of glass fibers are E-glass (fiberglass) and S-glass. The "E" in E-glass corresponds to electrical since it was designed for electrical applications. Besides, it is used for many other purposes now, such as decoration and structural applications. The "S" in S-glass corresponds to higher content of silica. S-glass fibers hold their strength at high temperatures compared to E-glass and have higher fatigue strength. They are used principally for aerospace applications. Other types available commercially are C-glass (Corrosion) used in chemical environments, such as storage tanks; R-glass used in structural applications such as construction; D-glass (Dielectric) used for applications requiring low dielectric constants, such as radomes; and A-glass (Appearance) used to improve surface

appearance. Some combinational types such as E-CR glass (Electrical and Corrosion resistance) and AR glass (Alkali Resistant) also exist (Mallick 2007).

As a matrix, epoxy is the most commonly used polymeric composite matrix, however it is costlier than other polymer matrices. More than two-thirds of the polymer matrices used in aerospace applications is epoxy based. Because of their some advantages such as high strength, low viscosity and low flow rates, which allow good wetting of fibers and prevent misalignment of fibers during processing, low volatility during cure, corrosion resitance, low shrink rates, which reduce the tendency of gaining large shear stresses of the bond between epoxy and its reinforcement, epoxy resins are the most widely held polymeric composite matrix and existing in more than 20 grades to meet specific property and processing requirements (Mazumdar 2001).

2.5.3. Manufacturing Methods

Manufacturing holds great importance for quality of the finishing part. Especially in polymeric composites, phenomena like void formation, wetting, degree of curing, resin flow, processing time and reinforment ratio hugely affect the final product. The early manufacturing method for fiber-reinforced composite structural parts used a hand lay-up technique. Although hand lay-up is a reliable process, it is by its nature very slow and labor-intensive. In recent years, particularly due to the interest generated in the automotive industry, there is more emphasis on the development of manufacturing methods that can support mass production rates. Resin transfer moulding (RTM) is another manufacturing process that has received significant attention in both aerospace and automotive industries for its ability to produce composite parts with complex shapes at relatively high production rates (Long 2005; Campell 2003; Mazumdar 2001).

In RTM, several layers of dry continuous fiber reinforcement are placed in the bottom half of a two-part mould, the mould is closed, and a catalyzed liquid resin is injected into the mould via a centrally located channel. The injection pressure is in the range of 0.7 – 7 bars. As the resin flows and spreads throughout the mould, it fills the space between the fiber yarns in the dry fiber preform, displaces the entrapped air through the air vents in the mould, and coats the fibers. Depending on the type of the resin-catalyst system used, curing is performed either at room temperature or at an

elevated temperature in an air-circulating oven. After the cured part is pulled out of the mould, it is often necessary to trim the part at the outer edges to conform to the exact dimensions. (Long 2005) Step by step schematic illustration of RTM process is shown in Figure 2.11.

There are several variations of the basic RTM process described earlier. In one of these variations, known as vacuum-assisted RTM (VARTM), vacuum is used in addition to the resin injection system to pull the liquid resin into the preform.
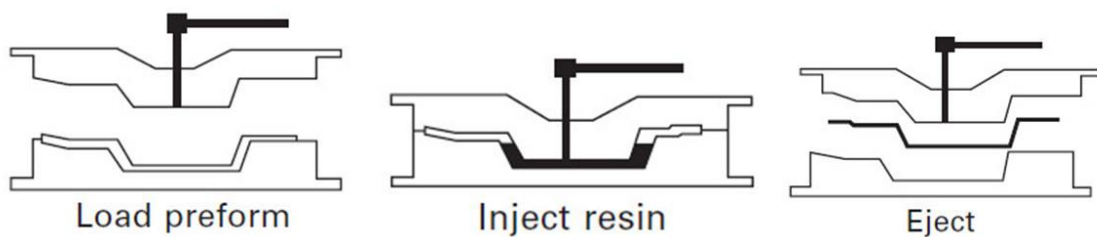
Figure 2.11. Step by step schematic illustration of RTM process
(Source: Long 2005)

Vacuum infusion is another type of process that compared to RTM, the upper half of the mould pair is replaced with a vacuum membrane. This reduces the tooling cost significantly and provides an increasingly important fabrication route for large structures where the throughput requirement is small (Long 2005). The key advances over open-mould alternatives are control of volatiles, thickness and fibre volume fraction (V_f) and resin consumption. The usual infusion set-up involves a mould operated at room temperature. The fabric is laid-up by hand, followed by the ancillary materials – peel ply, breather felt, infusion mesh and vacuum membrane. Sealing relies on mastic tape, as with conventional vacuum bag moulding, and the facility to pull an effective vacuum. While the impregnation process is relatively fast for most set-ups (owing largely to the infusion mesh), the overall manufacturing time may be quite similar to those for hand lay-up laminated products (Long 2005). This is because the mould preparation are all critical, manual operations. Cross section of a vacuum infusion process is schematically illustrated in Figure 2.12.
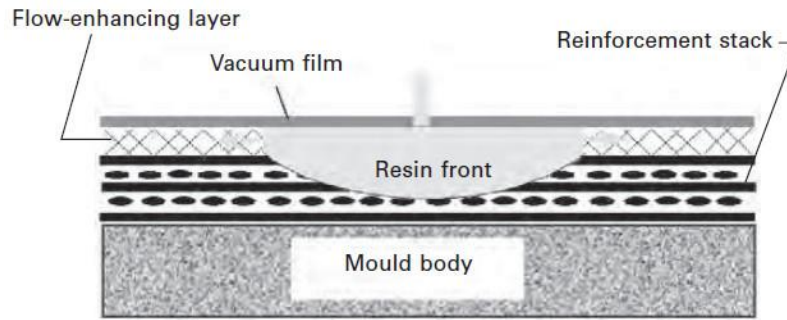
Figure 2.12. Schematic illustration of Vacuum Infusion process
(Source: Long 2005)

2.5.4. Hand Lay-Up

Hand lay-up or wet lay-up is the simplest and oldest open moulding method of the composite fabrication processes. It is a low volume, labor intensive method suited especially for large components, such as boat hulls. Glass or other reinforcing fabric is positioned manually in the open mould, and resin is poured, brushed, or sprayed over and into the glass plies. Entrapped air is removed manually with squeegees or rollers to complete the laminates structure. Room temperature curing polyesters and epoxies are the most commonly used matrix resins. Curing is initiated by a catalyst in the resin system, which hardens the fiber reinforced resin composite without external heat. For a high quality part surface, a pigmented gel coat may optionally be applied to the mold surface (Campell 2003).

A step by step illustration of hand lay-up process is shown in Figure 2.13.
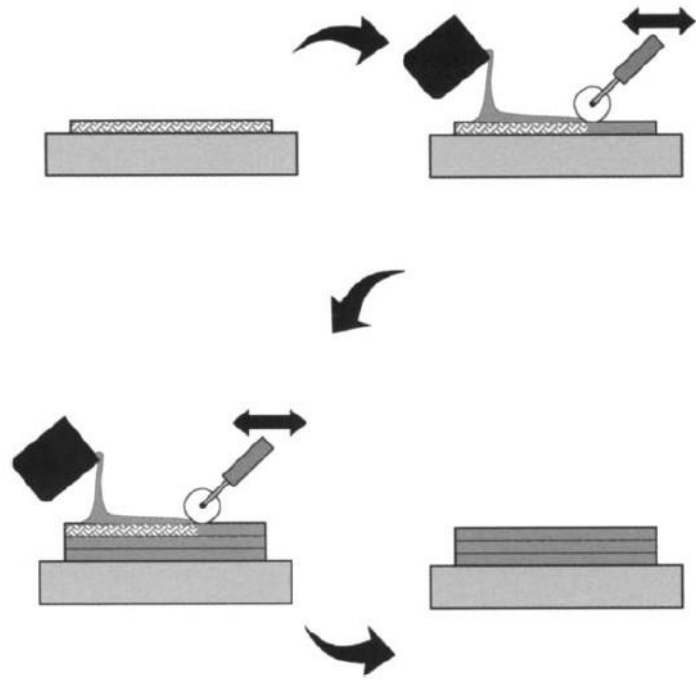
Figure 2.13. Illustration of Hand Lay-up process
(Source: Campell 2003)

CHAPTER 3

EXPERIMENTAL

3.1. Materials

In this study glass fiber reinforced epoxy matrix polymeric composites were manufactured for radar absorbing applications. Fiber reinforcement was non-crimp unidirectional glass fabrics purchased from Metyx Composites. The product coded as L300 E10B-0 Unidirectional E-Glass fabric that has about 330 gr/cm^2 area weight. Despite being branded as unidirectional, fabric was multiaxial as it contains fibers both in 0° and 90° directions. The fabrics contain fibers dominantly at 0°, having about 287 gr/m^2 areal weight and fibers at 90°, having about 37 gr/m^2 areal weight. Stiches are tricot and contribute to area weight about 10 gr/m^2. The photo of the fabric used within the study is shown in Figure 3.1.
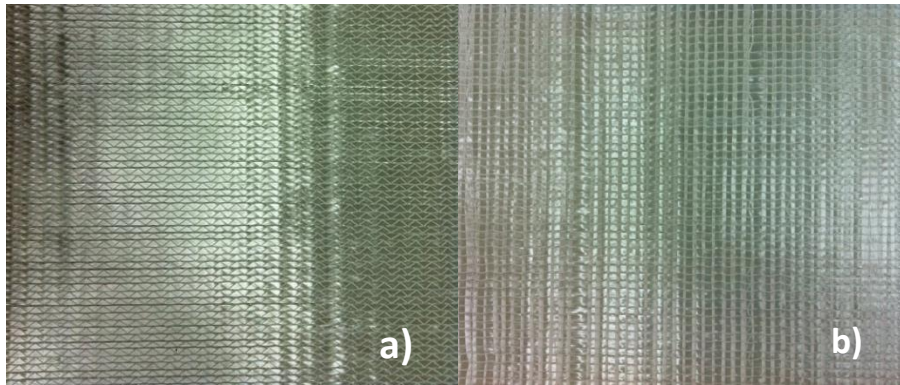
Figure 3.1. Photo of non-crimp E-Glass fabric, (a) front side, (b) back side, used within the study

Epoxy resin was used as a matrix material. It was purchased with the brand name of Momentive laminating resin MGS L 160 and hardeners MGS 160 and 260 S. It was chosen as a suitable combination specifically for processing lamination time and glass transition temperature (T_g).

Carbonyl Iron (CI) was chosen as a filler due to it's radar absorbing features. CI was purchased from Sigma Aldrich. Density of the CI reported as 7.86 g/mL at 25 ^{o}C. The CI was blended within epoxy matrix with the weight ratio of 25%.

3.2. Polymeric Composite Structure Manufacturing

For radar absorbing purposes, glass fiber reinforced epoxy matrix polymeric composite structures were manufactured. Hand lay-up technique was used for manufacturing purpose. Hand lay-up technique was followed by stacking and pressurizing the resin impregnated fabrics within a closed metal mould.

For comparison of both radar absorbing performance and mechanical properties, a symmetrical stacking squence was chosen. Eight layers of fabrics were used to prepare composite samples for mechanical property testing. Fabrics were stacked at $[0^{o}/90^{o}]_{2S}$ orientation. This orientation provides 0° direction on both surfaces which is recommended for ASTM D 3039 tensile test and ASTM D 6641 compression test. Also, center of symmetry provides appropiate condition for interlaminar peel testing.

For Salisbury screen and Jaumann absorber structures, fabric surfaces were coated with a thin layer of Indium Tin Oxide (ITO) by magnetron sputtering technique. The photo of magnetron sputtering unit used to coat E-glass fabrics is shown in Figure 3.2. Surface resistance of ITO coated fabrics were measured as 1000 Ω/square.
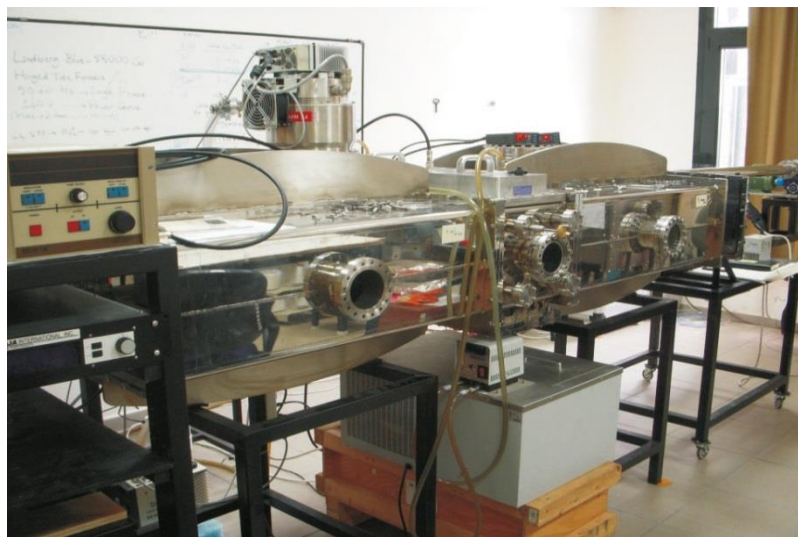
Figure 3.2. Photo of Magnetron Sputtering unit used for metal coating of fabrics

For manufacturing composites, fabrics were cut properly in the dimensions of the mould used. Hardeners of the epoxy resin (MGS 160 and 260 S) were mixed with 70:30 weight ratio to obtain expected thoughness and processing time which is set for about 2.5 hours. The epoxy resin was prepared by mixing of resin and hardeners by 100:27 weight ratio. CI filler was added to resin system after adequate mixing of resin and hardener. To prevent segregation of CI particles which have higher density than those of matrix, constant mechanical stirring was applied throughout the hand lay-up process. Manufacturing process, photographed step by step, is shown in Figure 3.3.
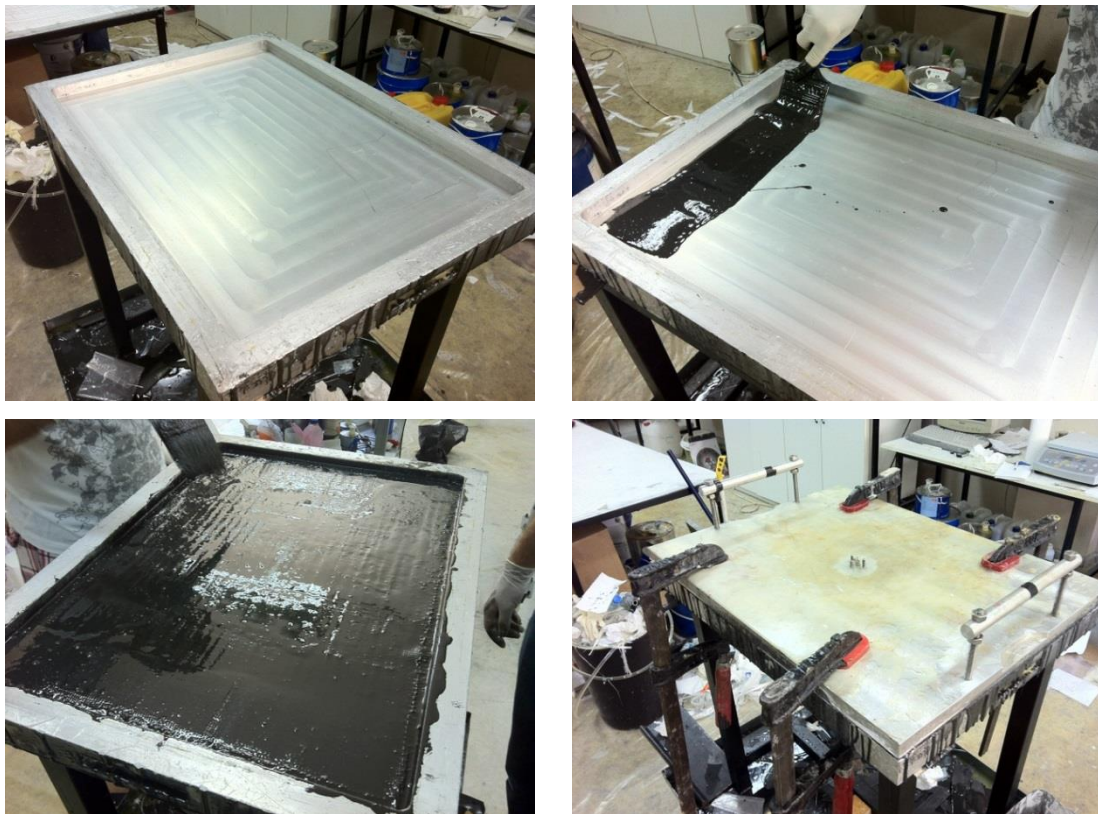
Figure 3.3. Step by step manufacturing of composites by hand lay-up technique

After finishing of hand lay-up process, the impregnated fabrics were placed in a metallic mould and the mould was closed and clamped firmly in order to increase fiber volume ratio and to improve surface properties of the composites for perfect finish of both surfaces of the samples. The laminates were cured for 24 hours at room temperature within the mould under pressure. After remolding the composite parts, post-curing was applied in a ventilated drying oven at 80 ^{o}C for 24 hours.

The fabricated structure is schematically illustrated in Figure 3.4. The composite samples were sectioned using a diamond saw for the preparation of test samples. Specimens that were prepared for radar wave absorbance measurements is shown in Figure 3.5.
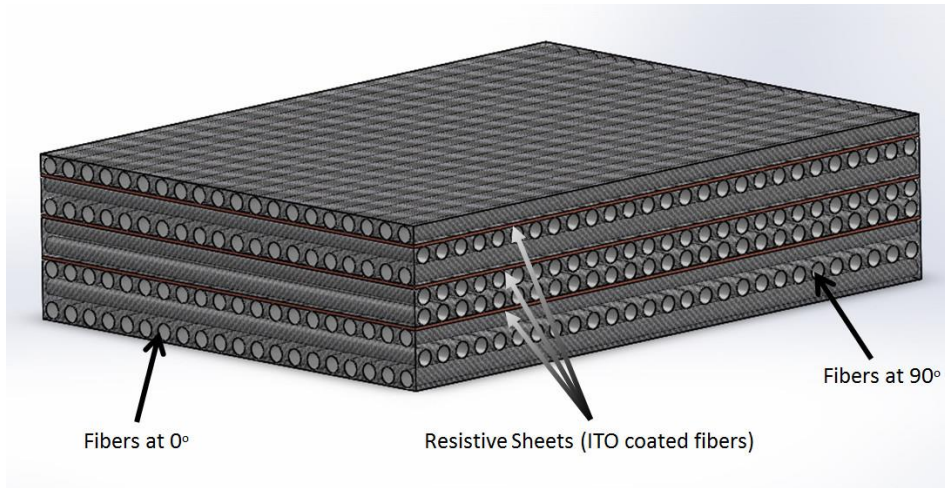
Figure 3.4. Schematic illustration of a laminated polymeric composite with 3 resistive sheets designed as Jaumann absorber
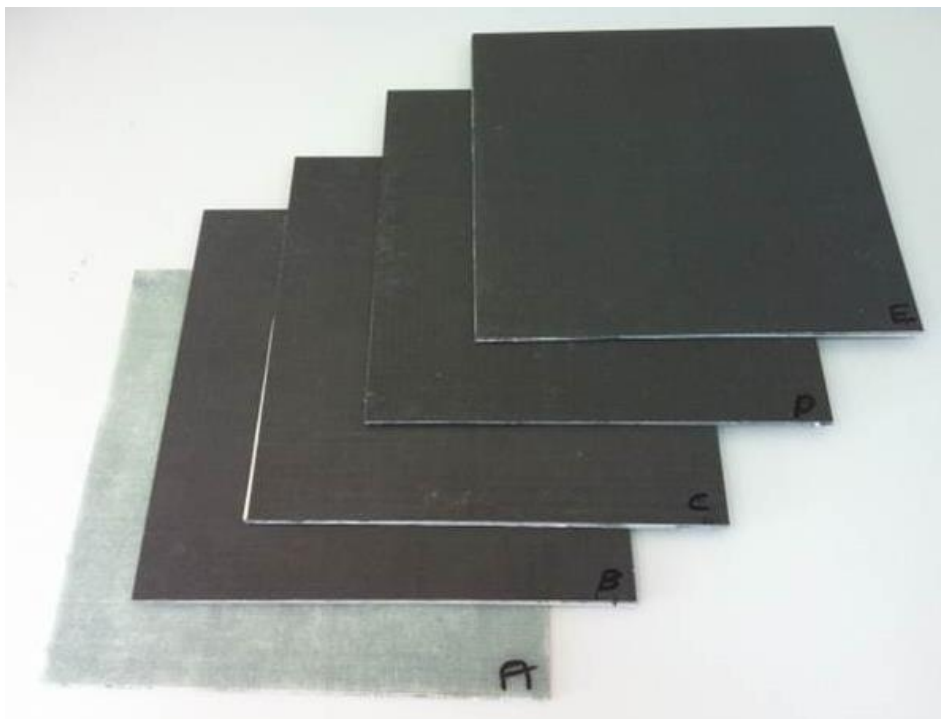
Figure 3.5. Photographs of manufactured specimens for electromagnetic absorbing measurements

3.3. Characterization of Radar Absorbing Structures

3.3.1. Microstructural Property Characterization

3.3.1.1. Determination of Fiber Weight and Volume Ratio

The fiber weight and volume ratio of radar absorbing polymeric composite was measured by ignition loss of cured resins in accordance with ASTM D 2584–02. In this method, small amount of samples (about 1 grams) from composite structures were cut and burned off in a high temperature oven at 700 $^{\circ}$C. The fiber and CI filler residues were weighted after cooling the samples to room temperature. Based on the weight and density of fiber, filler and polymer matrix, volume ratios were calculated by Equation 3.1.

$$V_f = \frac{v_f}{v_f + v_m + v_p} = \frac{\dfrac{m_f}{\rho_f}}{\dfrac{m_f}{\rho_f} + \dfrac{m_m}{\rho_m} + \dfrac{m_p}{\rho_p}} \tag{3.1}$$

In this equation, v_f, v_m and v_p indicate the volumes of fiber, matrix and filler respectively. m_f, m_m and m_p indicate the mass of fiber, matrix and filler of composite sample. In addition, ρ_f, ρ_m and ρ_p denotes densities of fiber, matrix and radar absorbing filler material.

In CI and ITO containing samples, these materials were also avalaible in the residue. ITO weight was neglected in the calculations because it hardly affected the weight due to its very thin layer of material (10-50 nm) nature. As epoxy burnt off from the sample, epoxy weight were known as residue weight subtracted from initial sample weight. Assuming epoxy matrix mixture ratio was homogeneous throughout the matrix, CI weight calculated from epoxy weight. Then calculated CI weight subtracted from residue weight to obtain fiber weight. After weight calculations, by knowing densities of the materials in the structure, volumes and volume ratios were calculated.

3.3.1.2. Microstructure by Scanning Electron Microscopy

Scanning electron microscopy (SEM) and Energy-Dispersive X-Ray (EDX) mapping were performed on ITO coated and uncoated fabric surfaces and cross sections of radar absorbing structures. For this purpose, Quanta 250FEG scanning electron microscope at IZTECH Materials Research Center was used.

Back scattering electron mode was used through SEM analysis. This mode provides identification of materials based on their atomic number, thus creating a contrast between higher and lower atomic numbered elements.

3.3.2. Dynamic Mechanical Analysis (DMA)

Dynamic Mechanical Analysis (DMA) experiments were performed on samples sectioned as 60 mm length and 10 mm width. DMA was performed to evaluate the storage (E') and loss (E") modulus of materials at different frequencies and temperatures. The samples were tested in a TA Instruments Q800 (Figure 3.6) in dual cantilever mode.

Glass transition temperatures (T_g) of specimens were determined from the maximum value of Tan Delta (Tan δ), which is the tangent of storage and loss modulus ratio.

Figure 3.6. Photo of TA Instruments Q800 DMA

3.3.3. Mechanical Property Characterization

Mechanical properties of manufactured radar absorbing structures were investigated to evaluate the mechanical performance of RAMs and to determine the effect of filler and coated fabrics on the structral integrity of the composites. Quasi-static tests such as tensile, bending and compression tests were performed on the specimens sectioned from composite plates. Also, impact strength and interlaminar fracture thoughness test were conducted based on standard procedures.

3.3.3.1. Determination of Tensile Properties

Standard test procedure in accordance to ASTM D 3039-00 was applied for determination of tensile properties, tensile strength, tensile modulus and strain at failure of samples manufactured.

Test specimens with dimensions of 250 mm length and 25 mm width were prepared using a diamond saw. At least 5 samples were tested for each composite configurations. The specimens were tested at room temperature using universal mechanical testing machine, Shimadzu AG-IC 100KN at a cross head speed of 2 mm/min. Strain values were measured by video extensiometer. Tensile grips and specimen during tensile testing is shown in Figure 3.7.

Figure 3.7. Photo of experimental setup for tensile tests

Tensile stress and strain values were calculated based on the following equations;

$$\sigma = \frac{F}{A} \tag{3.2}$$

$$\varepsilon = \frac{(L - L_0)}{L_0} \tag{3.3}$$

In the Equation 3.2 and 3.3, F is the ultimate load, A is the cross sectional area of the specimen tested, L_0 is the original distance between gauge marks and L is the distance between gauge marks at any time. Elastic modulus (E) was obtained from the initial slope of the stress-strain curves.

3.3.3.2. Determination of Flexural Properties

The flexural test and specimen preparation was performed in accordance with ASTM D 790-03. Specimes were tested in 3-point bending configuration with a span to thickness ratio of 16. Specimen length, span distance and test speed were adjusted according to specimen thickness with correlations provided from test standard. All specimens were cut 13 mm wide through all flexural tests. At least five specimens from each radar absorbing structures were tested using the universal testing machine. Force and deflection values at the center of the beam was recorded. Flexural test setup can be seen in Figure 3.8.


Figure 3.8. Photo of experimental setup for flexural tests

3.3.3.3. Determination of Compressive Properties

Compression test method according to ASTM D 6641-01 was utilized to measure in-plane compressive strength, compressive modulus and strain at break values of the composite panels manufactured. For this purpose, compression test specimens in the length of 140 mm and the width of 12 mm were sectioned from manufactured panels. Compression tests along in-plane loading direction were performed using the universal test machine with test fixture shown in Figure 3.9, at a cross-speed of 1.3 mm/min. At least 5 specimens for each set were tested and force vs. stroke data were recorded. The compressive stress values were obtained by dividing load values with cross-sectional area of the specimens. The strain was estimated by dividing stroke values with the initial specimen thickness. The modulus values were estimated from the slope of the stress-strain graphs.
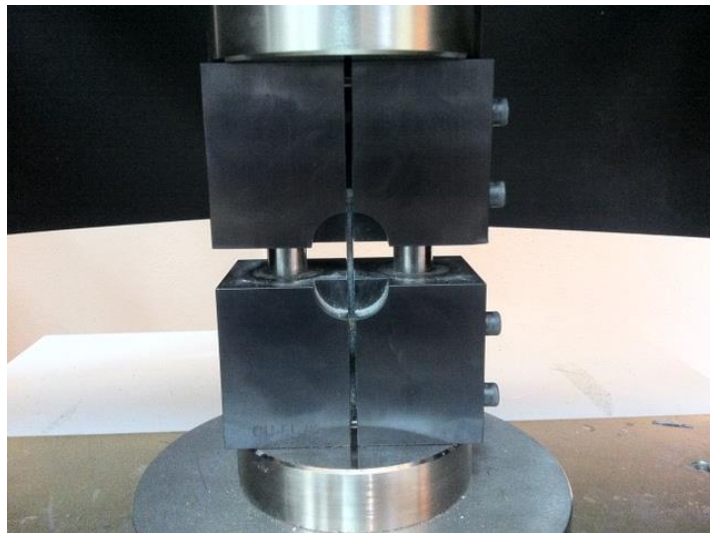
Figure 3.9. Photo of experimental setup for compression tests

3.3.3.4. Determination of Charpy Impact Strength

A Charpy impact test provides a measurement of the impact toughness of a material. A swinging pendulum was used in the Charpy test to initiate and propagate cracking in a notched sample. The pendulum was released from a known height it rotates to the bottom position. At the bottom, the pendulum impacts the sample that is setup in single-edge notched specimen and then the pendulum swings up to a final

height, which is recorded. The difference between the initial and final heights of the pendulum and the pendulum mass were used to calculate the potential energy loss of the pendulum, which is the primary measurement in a typical Charpy test.

The fracture energy is the amount of energy absorbed by the sample that fractures, and in such a sample is equal to the potential energy loss of the pendulum. The energy measured from a Charpy test is the sum of several components including the energy to initiate a crack, propagate the crack, elastically and plastically deform the material around the crack and contact surfaces, and accelerate the sample. As a result, the Charpy test provides a measure of these combined mechanisms.

Specimens were prepared according to ISO 179 with the dimensions of 80 mm length and 10 mm width. In addition, all specimes were notched 2 mm in-plane direction in accordance with ISO 179. At least 5 specimens were tested for each sample plate. Impact energy values were recorded from CEAST 6545 Charpy Impact Energy Test Instrument shown in Figure 3.10.
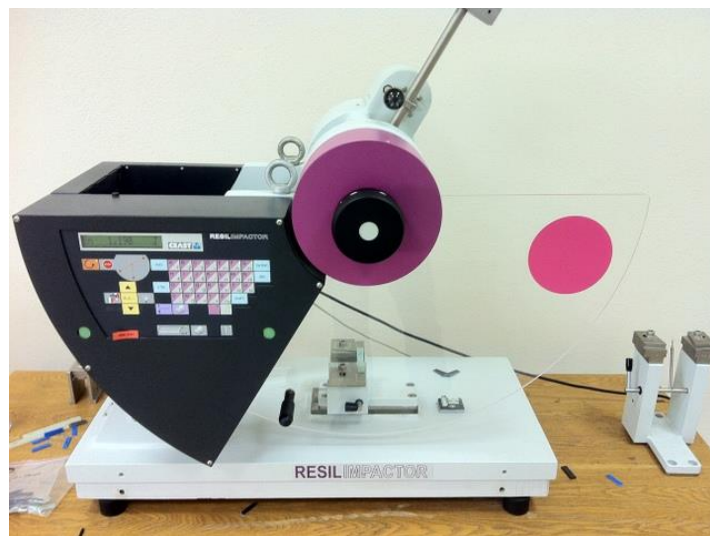
Figure 3.10. Photo of experimental setup for Charpy impact tests

3.4. Evaluation of Radar Wave Absorbing Properties

Four different structure designs were proposed for electromagnetic wave absorption purpose. These include a Dallenbach layer, a Salisbury screen, and two Jaumann absorbers which consist different number of resistive layers. Salisbury screen

and Jaumann absorbers have a front spacer material which was same as matrix, for protecting the first resistive sheet.

All simulations and optimizations were based on permittivity and permeability data acquired from literature (Y. Qing et al. 2009). Results obtained from these optimizations had given preliminary design for manufactured samples. Composite structures based on optimization results were manufactured and reflection loss measurements were performed and those experimental values were compared with simulation results.

3.4.1. Construction of Governing Equations for RASs

Governing equations used for simulation and optimization for RAS derived from Transmission Line circuit equivalent of the proposed designs.

Dallenbach layer consist of a single layer of lossy material, in our case, this layer is 25 wt.% CI filled glass fiber/epoxy system. Equation 3.4 used for simulation and optimization purposes.

$$Z_1 = \eta_1 \tanh(\beta_1 t_1) \tag{3.4}$$

Z_1 denotes input impedance of layer 1, η_1 refers to characteristic impedance of layer 1 and β_1 is the propagation constant of layer 1. The only design variable is the thickness of the lossy material layer (t_1). As thickness changes, resonant frequency of the layer, as well as the bandwidth of absorbance through within 2-18 GHz range changes. Schematic illustration and circuit equivalent of Dallenbach layer are shown in Figure 3.11.
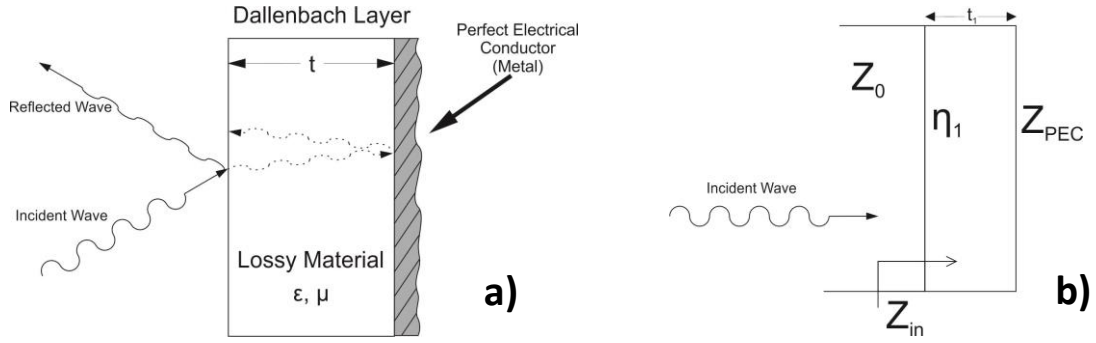
Figure 3.11. Schematic illustration of (a) and circuit equivalent (b) of Dallenbach layer

In Salisbury screen simulation, surface resistance of ITO coated fabric was added into the transmission line equations. In addition to resistive sheet, a front spacer layer for protecting the resistive sheet was added into structure. Equations 3.4 to 3.6 were derived for optimization purposes. Schematic illustration and circuit equivalent of Salisbury screen with front spacer layer and resistive sheet are shown in Figure 3.12.

$$Z_1 = \eta_1 \tanh(\beta_1 t_1) \tag{3.4}$$

$$Z_2 = \frac{Z_1 R_{s,1}}{Z_1 + R_{s,1}} \tag{3.5}$$

$$Z_3 = \eta_2 \frac{Z_2 + \eta_2 \tanh(\beta_2 t_2)}{\eta_2 + Z_2 \tanh(\beta_2 t_2)} \tag{3.6}$$
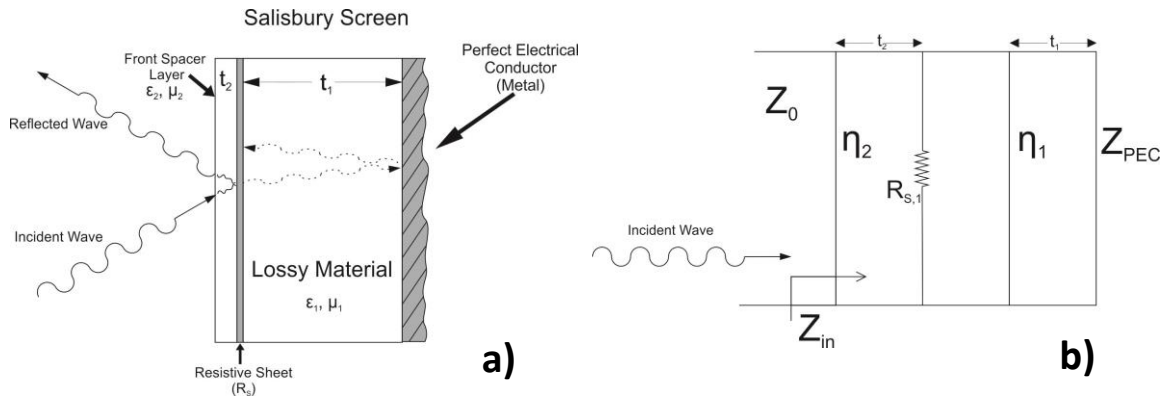

Figure 3.12. Schematic illustration of (a) and circuit equivalent (b) of Salisbury screen

Jaumann absorbers include additional resistive sheets into the radar absorbing structure, thus increasing the bandwidth of absorbance. In turn, simulation complexity increases as design variables such as thickness of layers between resistive sheets are

included. So, Equations 3.4 to 3.9 can be written for Jaumann absorbers in general, as given below.

$$Z_1 = \eta_1 \tanh(\beta_1 t_1) \tag{3.4}$$

$$Z_2 = \frac{Z_1 R_{s,1}}{Z_1 + R_{s,1}} \tag{3.5}$$

$$Z_3 = \eta_2 \frac{Z_2 + \eta_2 \tanh(\beta_2 t_2)}{\eta_2 + Z_2 \tanh(\beta_2 t_2)} \tag{3.6}$$

$$Z_4 = \frac{Z_3 R_{s,2}}{Z_3 + R_{s,2}} \tag{3.7}$$

$$.$$
$$.$$
$$.$$

$$Z_{i-1} = \frac{Z_{i-2} R_{s,n}}{Z_{i-2} + R_{s,n}} \tag{3.8}$$

$$Z_i = \eta_i \frac{Z_{i-1} + \eta_i \tanh(\beta_i t_i)}{\eta_i + Z_{i-1} \tanh(\beta_i t_i)} \tag{3.9}$$

Schematic illustration for multilayer Jaumann absorber structures containing two and three resistive sheets are shown in Figures 3.13 and 3.14.
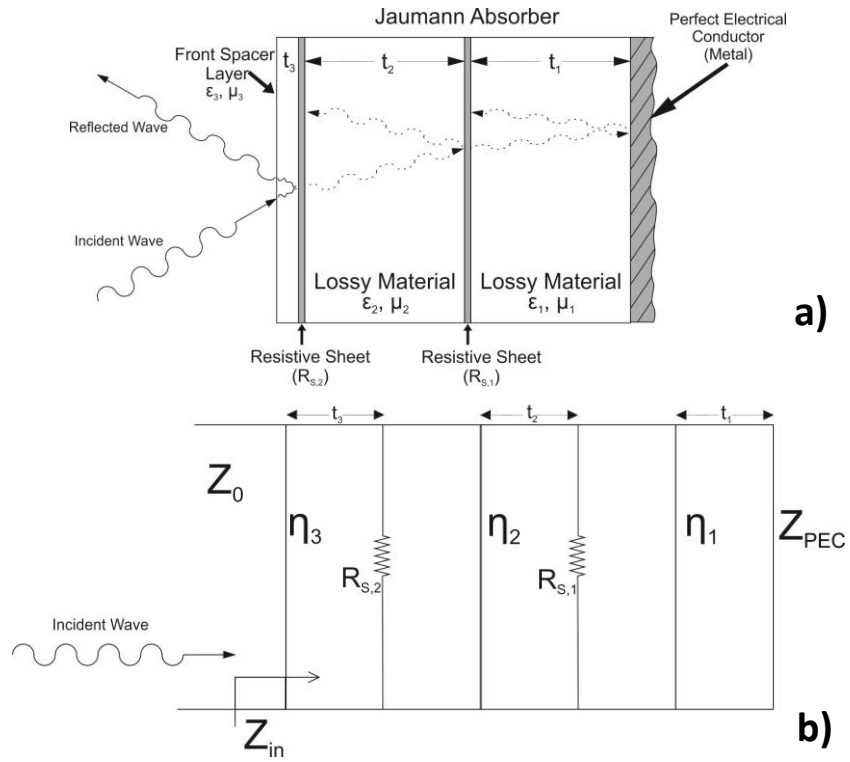
Figure 3.13. Schematic illustration of (a) and circuit equivalent (b) of Jaumann absorber with 2 resistive sheets
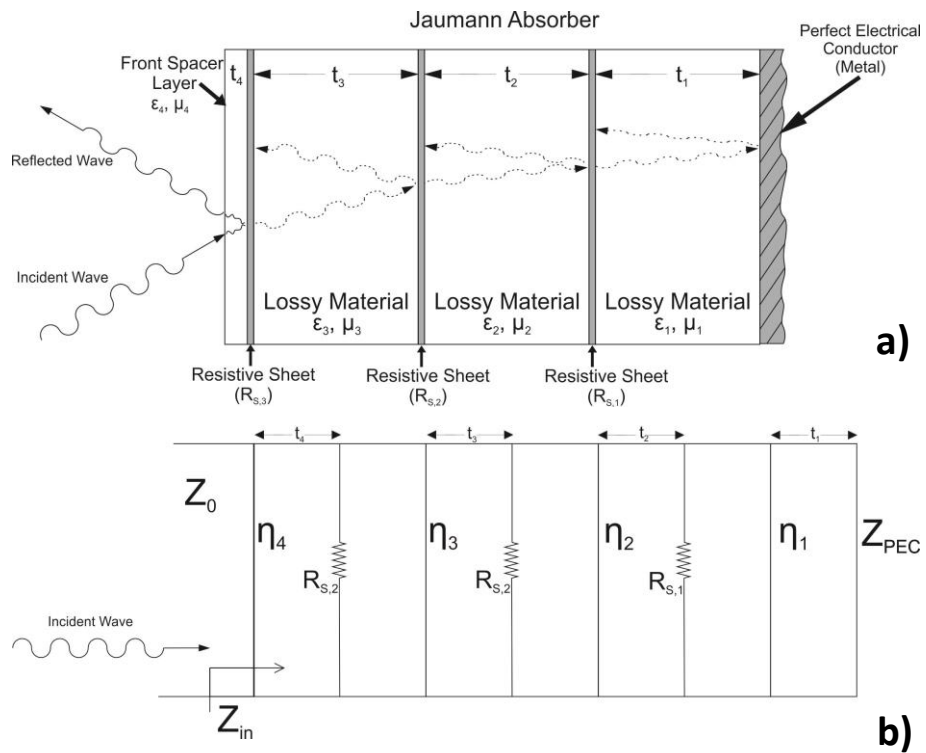

Figure 3.14. Schematic illustration of (a) and circuit equivalent (b) of Jaumann absorber with 3 resistive sheets

3.4.2. Genetic Algorithm Optimization

Reflection loss simulation and Genetic Algorithm (GA) optimization codes were written in MATLAB software package. Governing equations for each structure mentioned in the previous section were implemented into the code with absorbance calculation.

Several parameters for GA optimization were modified for faster processing time without affecting the results. Initial population size was selected as 120 and crossover fraction was selected as 0.5. Stopping criteria were stall generations and total generations, and those values were selected as 200 and 250 respectively.

As a scholastic algorithm, GA results may change of each run. So, for validation of the solutions, at least ten runs of GA optimization were done for each structure and best results which have widest bandwidth of absorbance were taken.

Based on the optimization results obtained, samples were manufactured experimentally tested. Both simulation and measurement results were compared.

3.4.3. Reflection Loss Measurements

Reflection loss measurements were done by free space method, using HP 8720D Network Analyzer. A single broad band horn antenna operating between 700 MHz -18 GHz was used for both transmitting and receiving of electromagnetic waves in S_{11} mode. Experimental setup for reflection loss measurements is shown in Figure 3.15.

Samples were sectioned from manufactured composite plates by 30 cm width and 30 cm length. Sectioned samples were adhered to a 2 mm thick aluminum plate to ensure complete reflection in the back end of the sample.

Each sample plate placed before horn antenna and reflection loss data in dB was recorded between 1-18 GHz frequency ranges. Additionally, a polished metal plated was also placed in front of the antenna and its data was recorded. It is assumed that this plate reflects all the electromagnetic waves transmitted from the antenna. From the difference between sample data and polished metal plate data, absorption of electromagnetic waves can be observed.
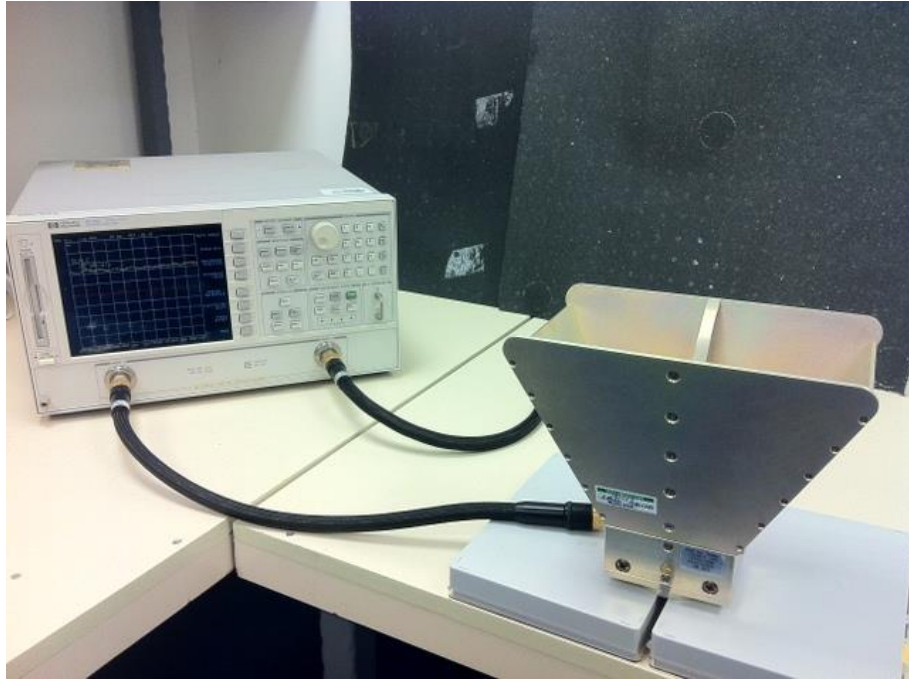
Figure 3.15. Experimental setup for free space measurements

CHAPTER 4

RESULTS AND DISCUSSIONS

In this chapter, simulation, optimization and experimental results for radar absorbing structures are given. The design approach for RAMs, the fabrication routes of polymeric composites as RAS is introduced within the chapter. In addition, the microstructure and mechanical properties of the radar absorbing structures are also given. Finally, reflection loss measurements are presented.

4.1. Structures Manufactured

Five different structures were manufactured for evaluation of radar absorbing capability and mechanical properties. The list of sample configuration are given in Table 4.1.

Sample A contained no modification and used as a reference plate for mechanical and radar absorbing analysis. It only contained 8 layers of glass fabric with $[0^o/90^o]_{2S}$ orientation. The thickness of the samples prepared with hand lay-up process was measured about 2.40 mm.

For preparation of sample B, 25 wt.% carbonyl iron was added as a filler into epoxy matrix. Carbonyl iron served as a ferrimagnetic absorber. This configuration was a Dallenbach layer and average thickness of 3.15 mm was measured for those samples.

Sample C was a representation of a Salisbury screen. A thin layer of Indium Tin Oxide (ITO) coated fabric layers replaced were used in addition to 25 wt.% CI filler within the matrix material. This coated layer act as a resistive sheet and assumed to increase the reflection loss. ITO coated fabric surface resistance measured as 1000 ohms/square. Resulting thickness of the samples was measured about 2.90 mm.

Sample D represents a Jaumann absorber with two resistive sheets. Sheets were placed according to optimization results. Similar to Sample C, all ITO coated fabric surface resistance were measured about 1000 ohms / square within these samples.

Sample E included an additional resistive sheet layer such that total of 3 resistive sheets existed within the structure.

Table 4.1. Configurations of radar absorbing structures fabricated

Sample #	# Layers	Filler	Resistive Sheets	Orientation
A	8	N/A	N/A	$[0^o/90^o]_{2S}$
B	8	25 wt% CI	N/A	$[0^o/90^o]_{2S}$
C	8	25 wt% CI	1 ITO coated fabric	$[0^o/90^o]_{2S}$
D	8	25 wt% CI	2 ITO coated fabrics	$[0^o/90^o]_{2S}$
E	8	25 wt% CI	3 ITO coated fabrics	$[0^o/90^o]_{2S}$

4.2. Microstructural Properties

4.2.1. Fiber Weight and Volume Ratio

Fiber volume ratio directly affects the physical properties of composite structures. Fibers are the main mechanical load-bearing elements of the structure, and as their volume increases in the structure, mechanical properties improves significantly. Thus, before comparing mechnanical properties of the samples, their fiber volume content should be also taken into account.

Tables 4.2 to 4.6 summarizes results for fiber weight and volume ratios for each sample. It is observed that fiber volume ratio may change due to manual clamping of the mould. In hand lay-up fabrication process, fiber volume ratio can not be fully controlled since it is a open mould process. Also, mould is pressurized by clamping and clamping force directly affects the fiber volume ratio.

Table 4.2. Fiber weight and volume ratios for Sample A

Sample #	Fiber Weight Ratio (%)	Fiber Volume Ratio (%)
1	60.60	39.97
2	61.56	40.93
3	61.15	40.52
4	62.50	41.90
5	63.18	42.61
Average	61.80	41.19
Std. Dev.	1.04	1.07

Table 4.3. Fiber weight and volume ratios for Sample B

Sample #	Fiber Weight Ratio (%)	Fiber Volume Ratio (%)
1	49.18	34.78
2	49.84	36.44
3	50.08	36.66
4	49.75	36.36
5	49.65	36.27
Average	**49.70**	**36.10**
Std. Dev.	**0.33**	**0.75**

Table 4.4. Fiber weight and volume ratios for Sample C

Sample #	Fiber Weight Ratio (%)	Fiber Volume Ratio (%)
1	56.97	42.19
2	56.12	42.46
3	55.12	41.47
4	55.91	42.25
5	54.54	40.91
Average	**55.73**	**41.86**
Std. Dev.	**0.94**	**0.65**

Table 4.5. Fiber weight and volume ratios for Sample D

Sample #	Fiber Weight Ratio (%)	Fiber Volume Ratio (%)
1	54.52	39.78
2	51.50	37.99
3	51.34	37.85
4	45.95	32.91
5	52.21	38.67
Average	**51.10**	**37.44**
Std. Dev.	**3.15**	**2.64**

Table 4.6. Fiber weight and volume ratios for Sample E

Sample #	Fiber Weight Ratio (%)	Fiber Volume Ratio (%)
1	58.36	43.58
2	58.88	45.25
3	56.29	42.63
4	57.47	43.81
5	58.53	44.88
Average	**57.90**	**44.03**
Std. Dev.	**1.04**	**1.05**

4.2.2. Microstructural Features of the RAS Structures

Figures 4.1 and 4.2 shows electron micrographs of carbonyl iron particles that were used throughout this study. Micrographs show that CI particles are nearly perfectly spherical with particle size ranges from 1 μm to 7 μm.

Figures 4.3 to 4.8 shows the SEM images taken from the cross section of Sample B and Sample C. Those images were taken using back scattering electron detector at 150X, 800X and 10,000X magnifications. Both structures consist of 0° and 90° fibers, epoxy matrix and carbonyl iron filler. Carbonyl iron particles are visible as brighter areas as compared to those of the others. This is due to iron element which has the highest atomic number in the structure.

It was observed that the distribution of carbonyl iron particles are not homogoneous throughout the matrix phase. Carbonyl iron particles seem to be precitipitated onto fabric layers. Although constant blending of particles and epoxy resin was applied until manufacturing process completed, these particles may precipitated within the structure due to significant density difference with the epoxy matrix during curing stages. The glass bundles with 0° and 90° are visible within the micrographs.

Sample C contains an ITO coated fabric, however, this layer is not visible in these images due to very thin coating thickness of the ITO layer (about 10-50 nm).
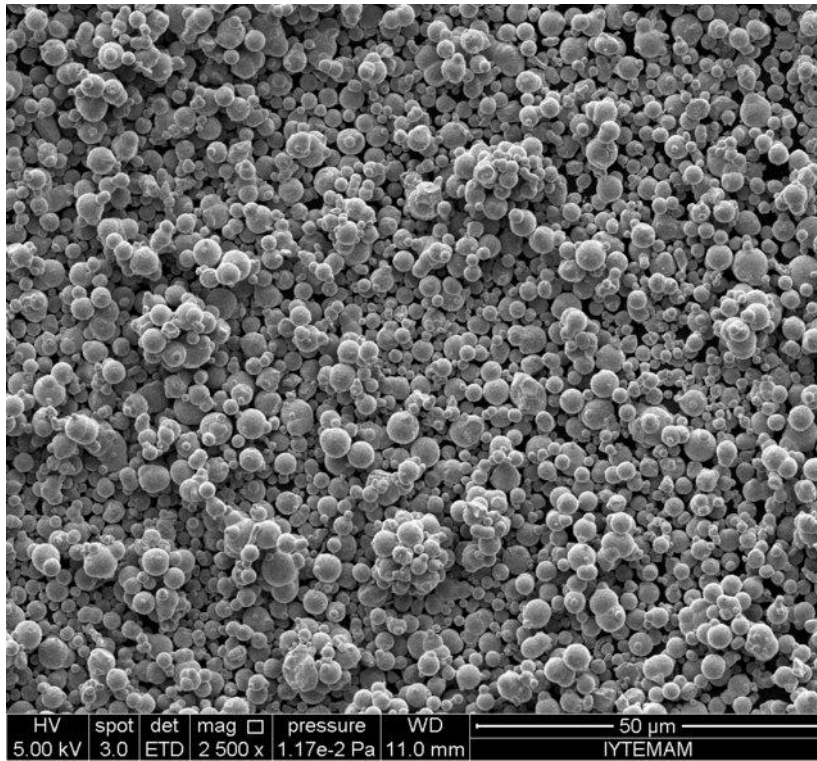
Figure 4.1. Electron micrograph of carbonyl iron powder (2500X)
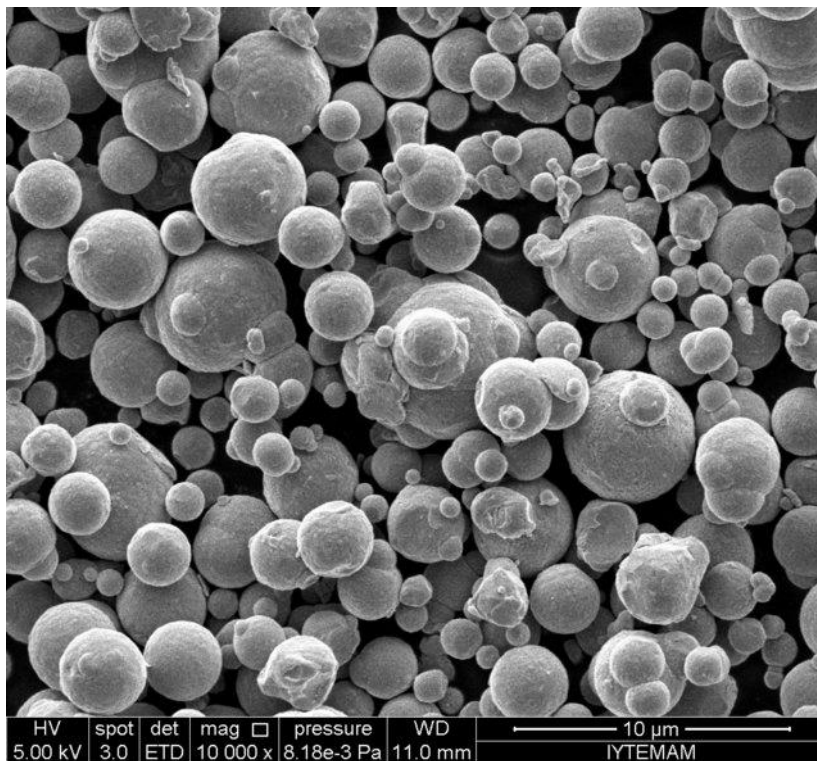
Figure 4.2. Electron micrograph of carbonyl iron powder (10000X)
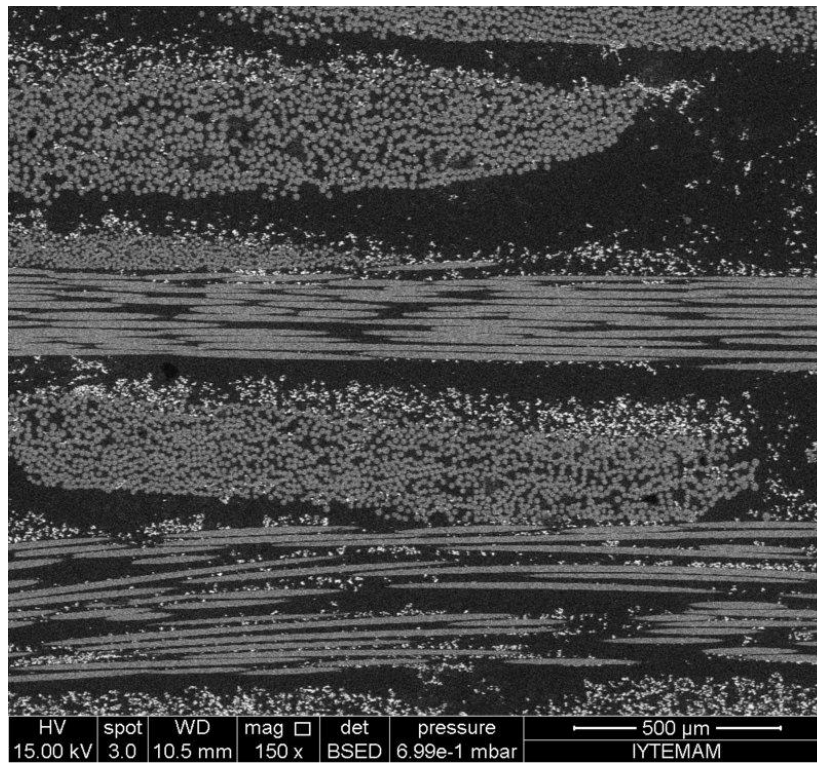
Figure 4.3. Back scattered electron micrograph from glass fiber / carbonyl iron / epoxy based laminated composite cross-section, sample (150X)
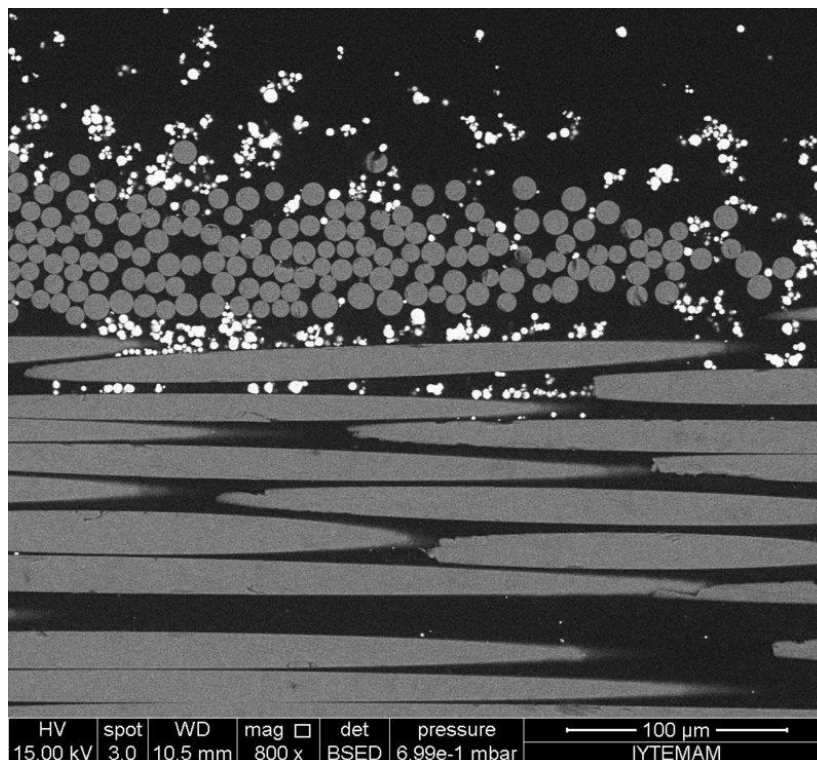

Figure 4.4. Back scattered electron micrograph from glass fiber / carbonyl iron / epoxy based laminated composite cross-section, sample (800X)
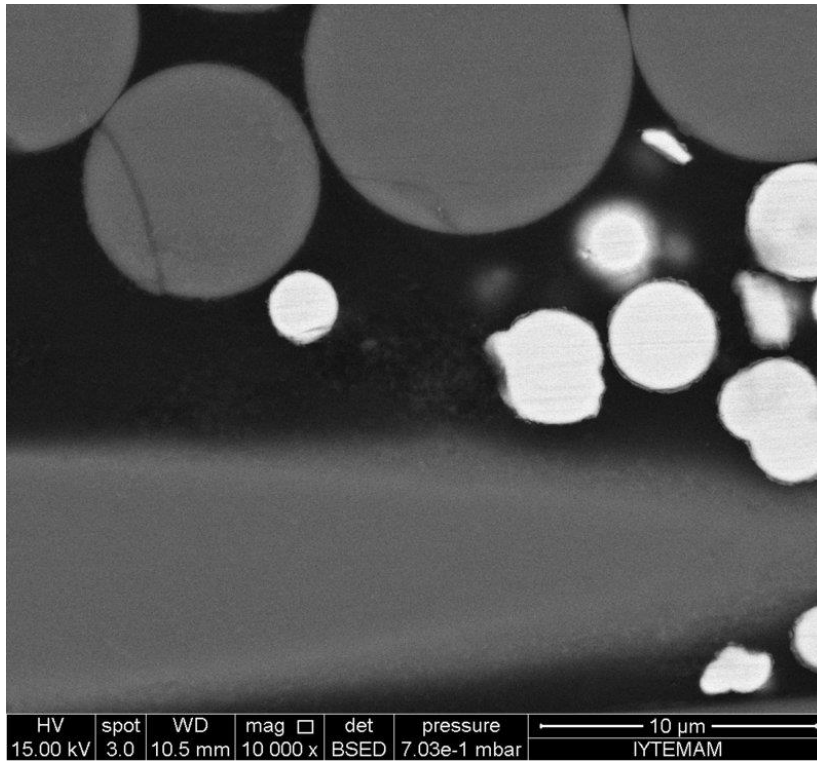
Figure 4.5. Back scattered electron micrograph from glass fiber / carbonyl iron / epoxy based laminated composite cross-section, sample (10000X)
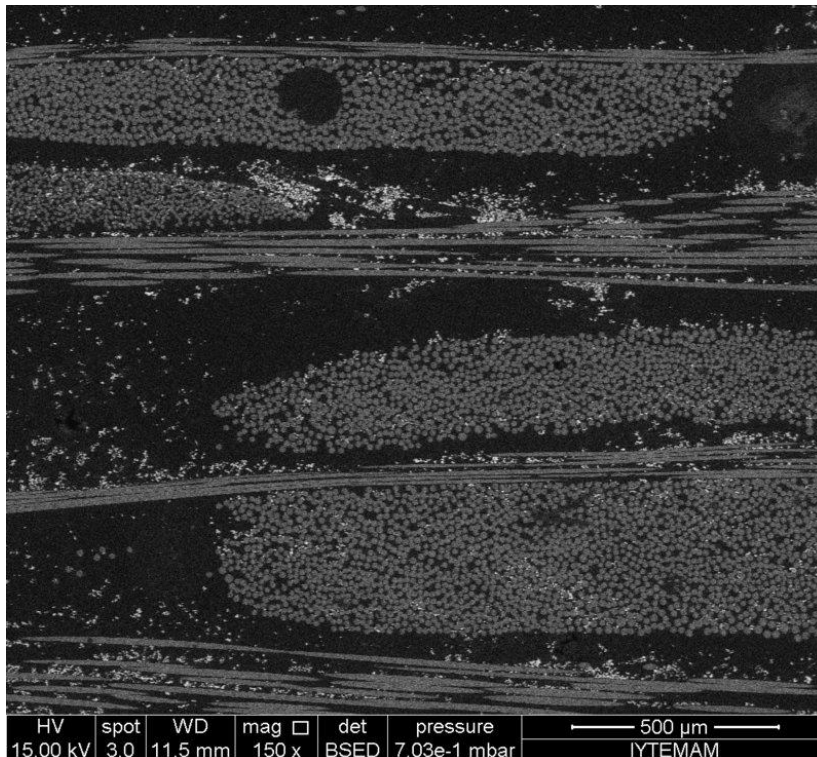
Figure 4.6. Back scattered electron micrograph from glass fiber / carbonyl iron / epoxy based laminated composite cross-section, sample (150X)
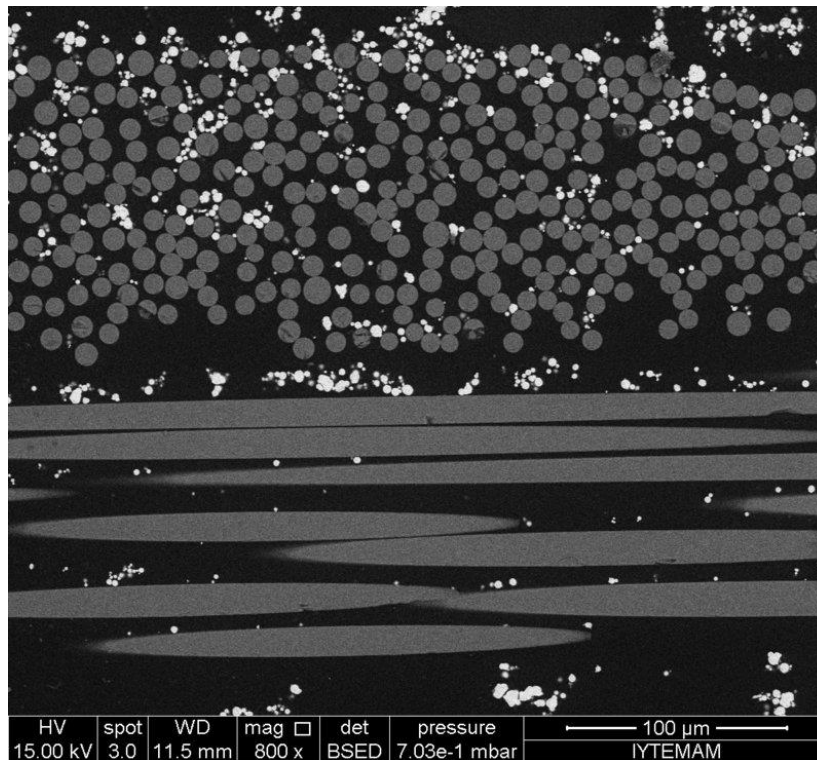
Figure 4.7. Back scattered electron micrograph from glass fiber / carbonyl iron / epoxy based laminated composite cross-section, sample (800X)
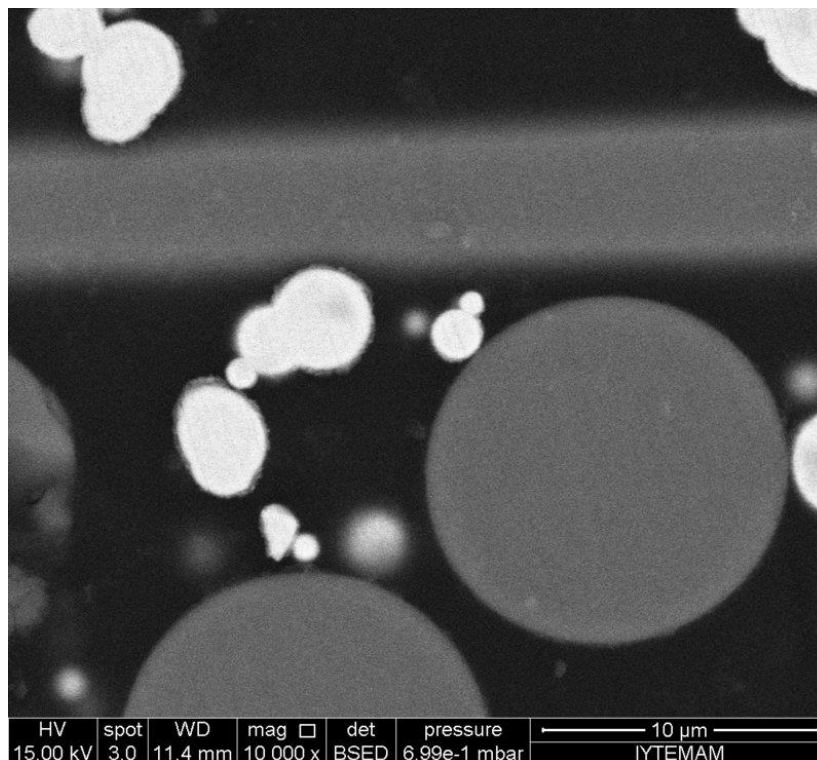
Figure 4.8. Back scattered electron micrograph from glass fiber / carbonyl iron / epoxy based laminated composite cross-section (10000X)

The surface features of the fabrics that were used in these study were also examined by SEM. Both conventional fabrics purchased from the manufacterer and ITO coated fabrics by magnetron sputtering method were examined. Figures 4.9 to 4.11 show the images of conventional E-glass fabric at 150X, 800X and 10000X magnification respectively. Figures 4.12 to 4.14 show ITO coated fabrics at 150X, 800X and 10000X magnification respectively. No significant changes that may happen due to magnetron sputtering coating method were observed at any magnification level in those fabrics.
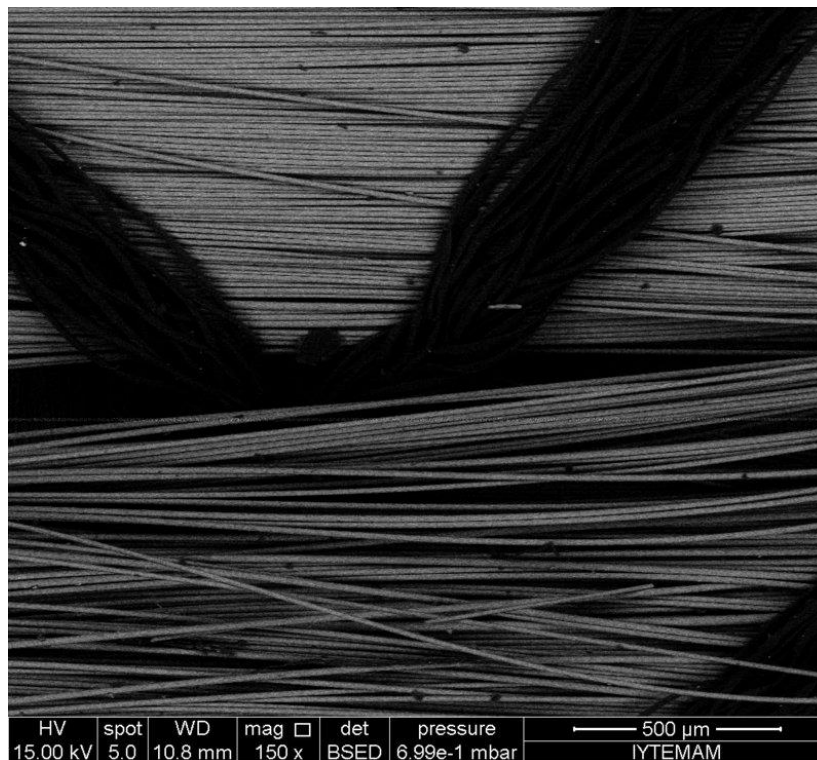

Figure 4.9. Back scattered electron micrograph of E-glass fabric (150X)
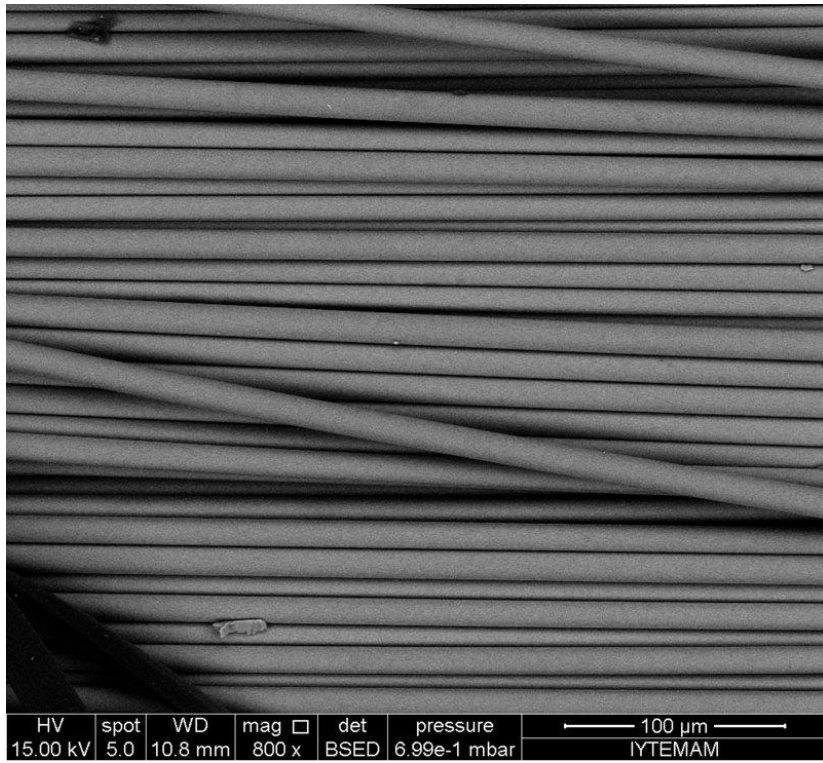
Figure 4.10. Back scattered electron micrograph of E-glass fabric (800X)
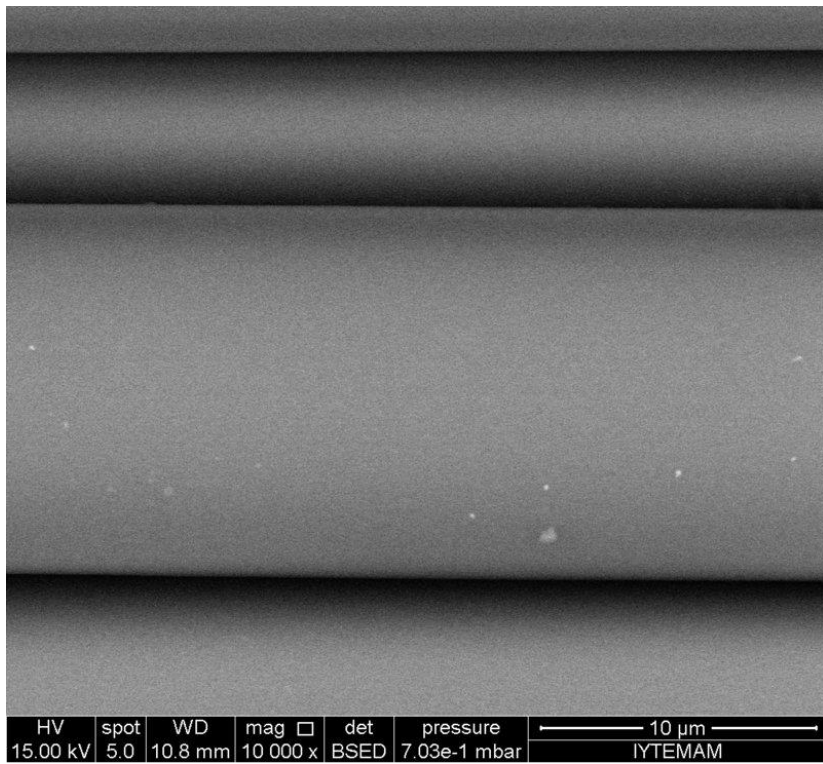
Figure 4.11. Back scattered electron micrograph of E-glass fabric (10000X)
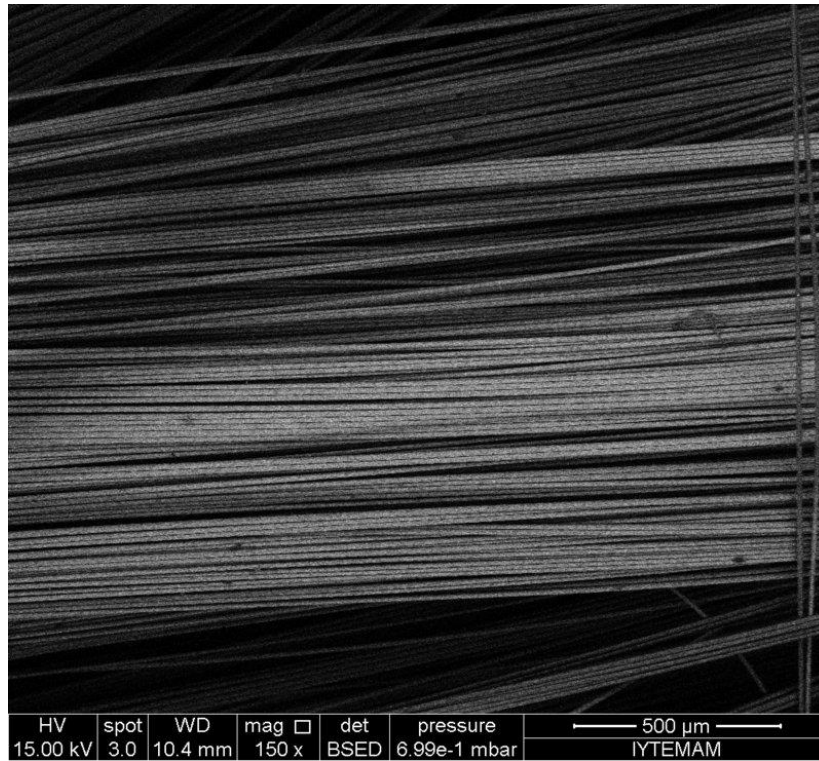
Figure 4.12. Back scattered electron micrograph of E-glass fabric with ITO coating (150X)
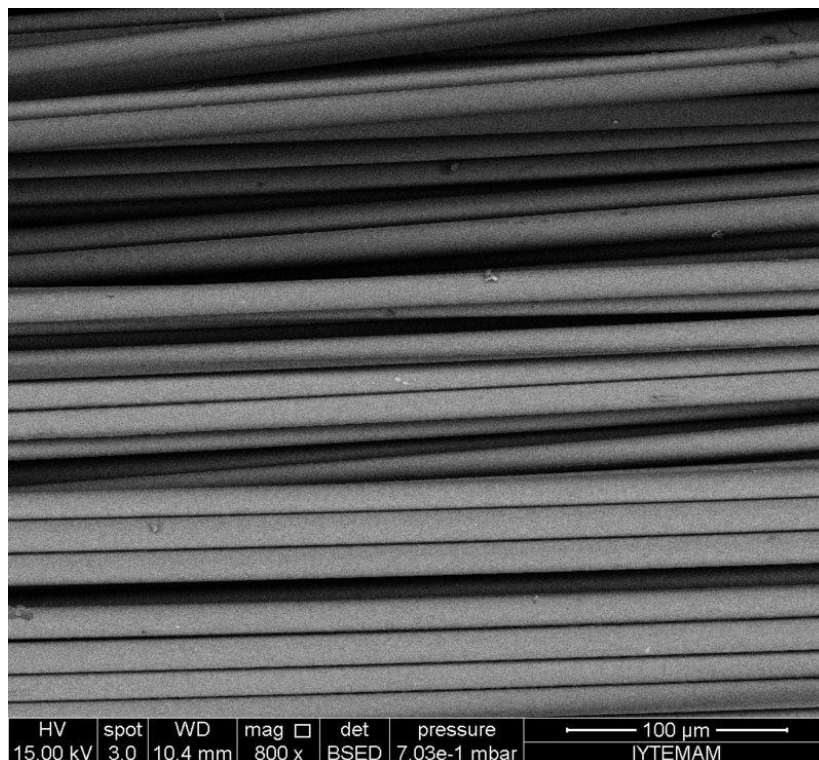

Figure 4.13. Back scattered electron micrograph of E-glass fabric with ITO coating (800X)
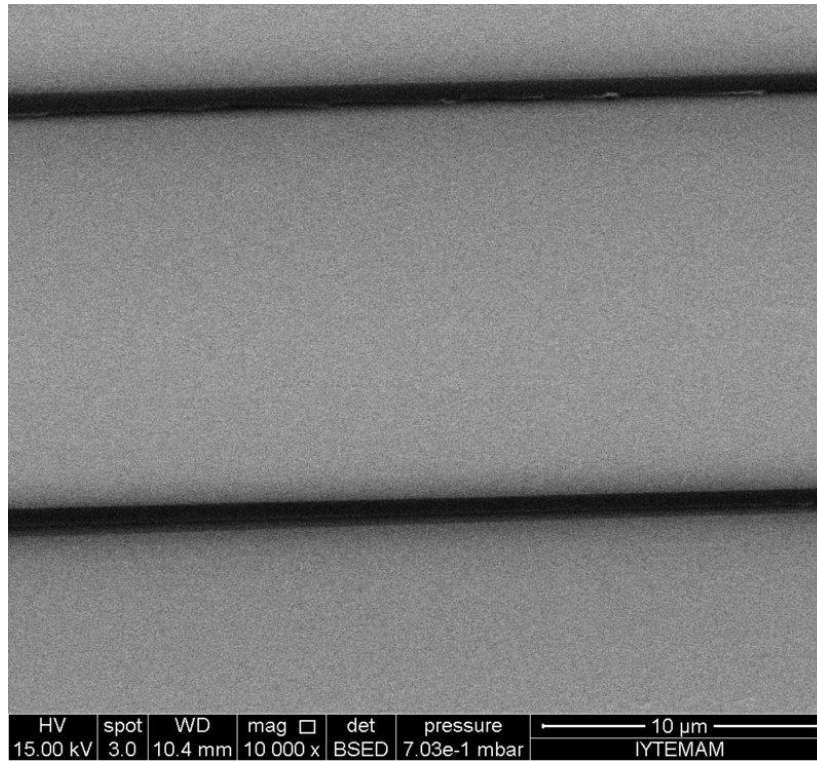
Figure 4.14. Back scattered electron micrograph of E-glass fabric with ITO coating
(10000X)

Electron dispersive X-Ray (EDX) spectroscopy technique was utilized in order
to investigate the surface chemical composition variations of conventional E-glass and
ITO coated E-glass.

Figure 4.15 shows elemental mapping image from conventional E-glass fabric,
which is dominated by silicon (Si), calcium (Ca), aluminum (Al) and oxygen (O)
elements. Figure 4.16 also shows EDX spectrum that indicates dominant elements as Si,
Ca, Al, O. Table 4.7. summarizes weight and atomic fractions of the conventional E-
Glass fabrics.
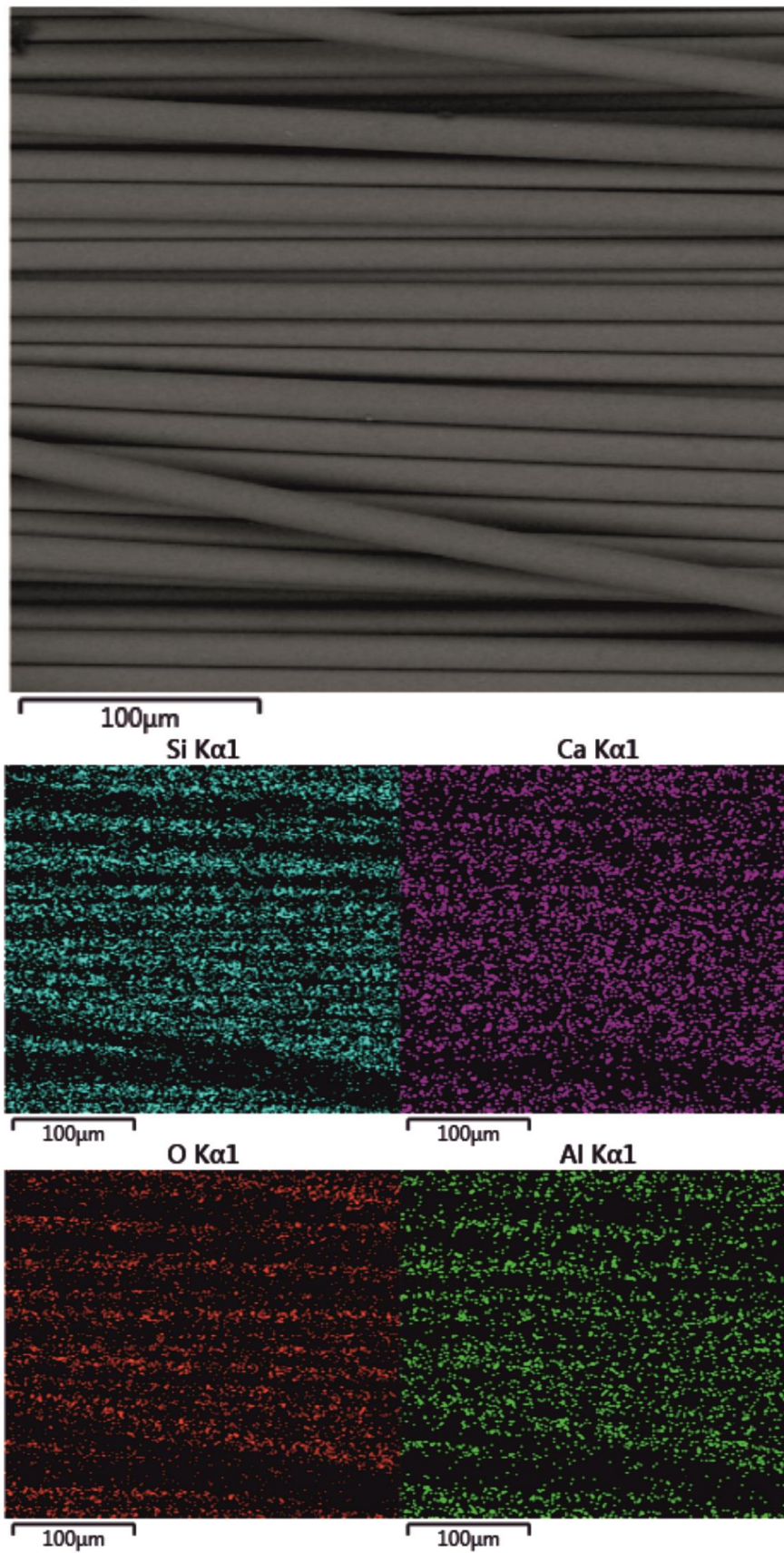
Figure 4.15. EDX mapping of uncoated conventional E-glass fabric
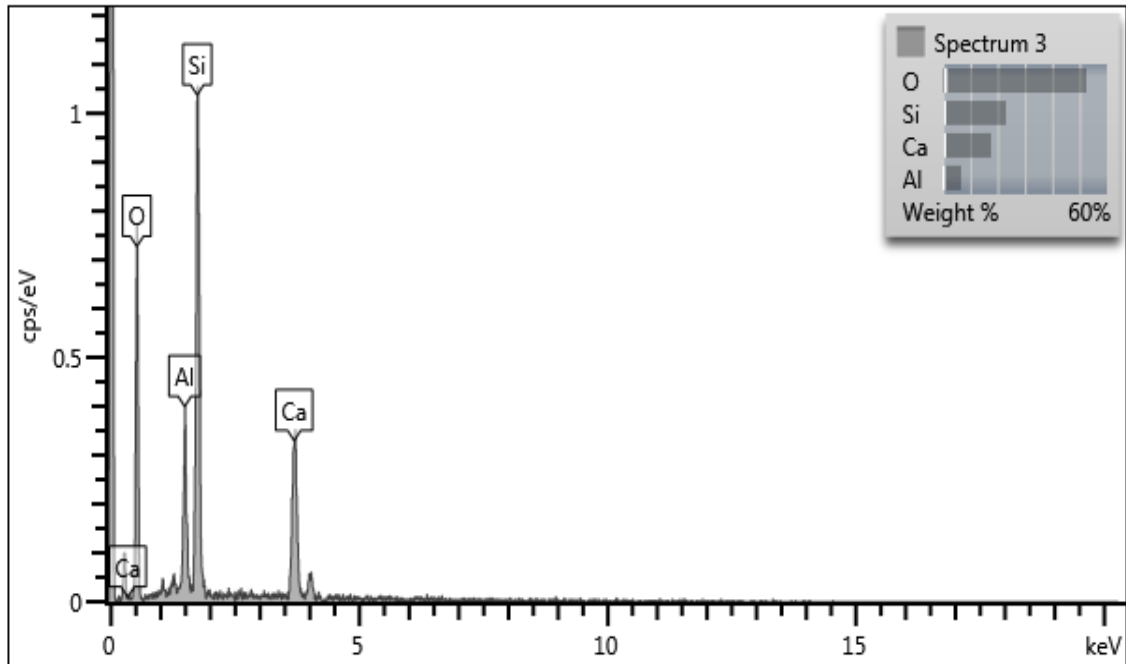
Figure 4.16. Chemical element analysis of uncoated conventional E-glass fabric

Table 4.7. Weight and atomic percentages of elements within uncoated E-glass fabric

Element	Wt%	Atomic %
O	52.50	68.45
Al	6.72	5.19
Si	23.12	17.17
Ca	17.67	9.19
Total:	100.00	100.00

Figure 4.17 shows elemental mapping of ITO coated E-glass fabric. Indium (In) as a component of ITO coating observed at the surface of the fabric. Figure 4.18 shows EDX spectrum of the ITO coated fabric surface. In this figure, in addition to indium, a low amount of tin (Sn) is also visible. Table 4.8 summarizes weight and atomic percentages of ITO coated E-glass fabric.
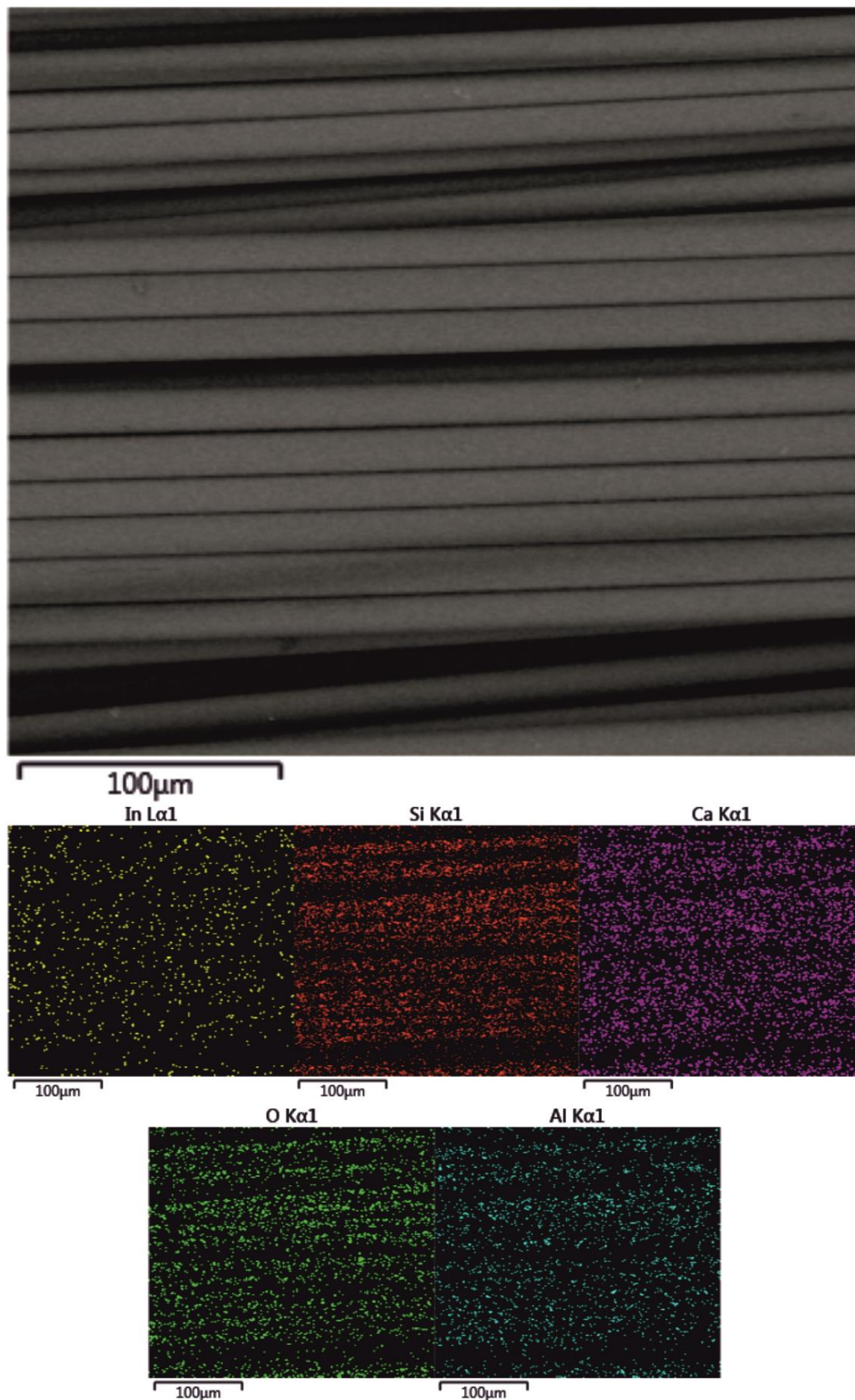
Figure 4.17. EDX mapping of ITO coated E-glass fabric
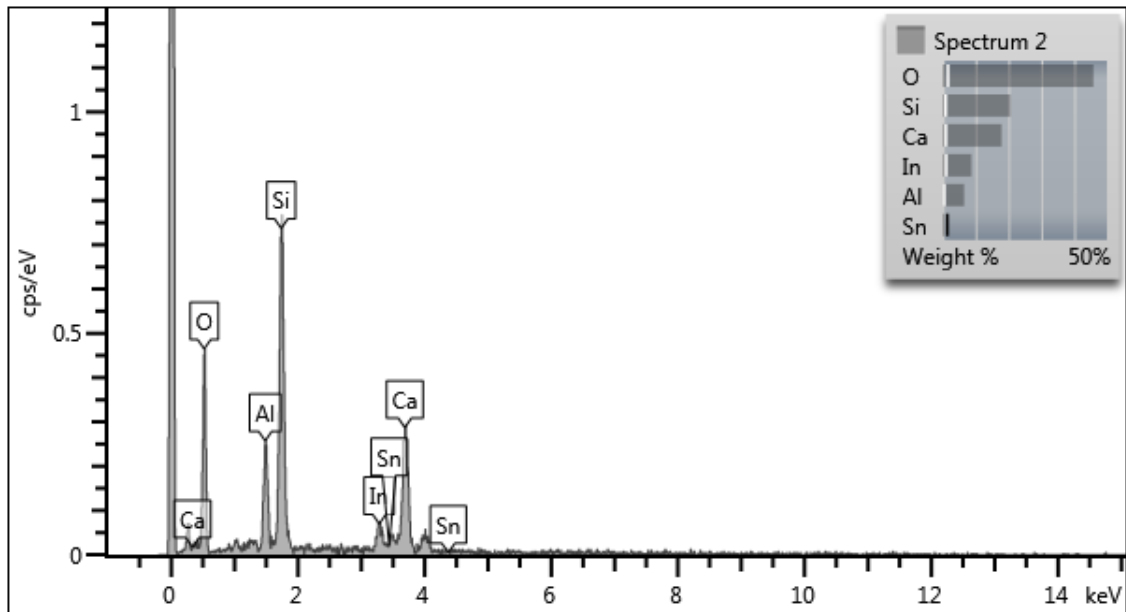
Figure 4.18. Chemical element analysis of ITO coated E-Glass fabric

Table 4.8. Weight and atomic percentages of ITO coated E-Glass fabric

Element	Wt%	Atomic %
O	45.83	65.60
Al	6.54	5.55
Si	20.62	16.82
Ca	17.87	10.21
In	8.72	1.74
Sn	0.42	0.08
Total:	100.00	100.00

Elemental mapping technique was also applied on the cross-section of radar absorbing structure sample B. Elemental mapping from cross section of sample B from two different locations are shown in Figures 4.19 and 4.20. As mentioned before, brightest particles are identifed as carbonyl iron. Similar to previous elemental mapping of fabrics, Si, Ca and Al elements that are dominant in fibers are visible. In addition to those, carbon as it is the primary element in epoxy chains, is visible within the EDX maps.
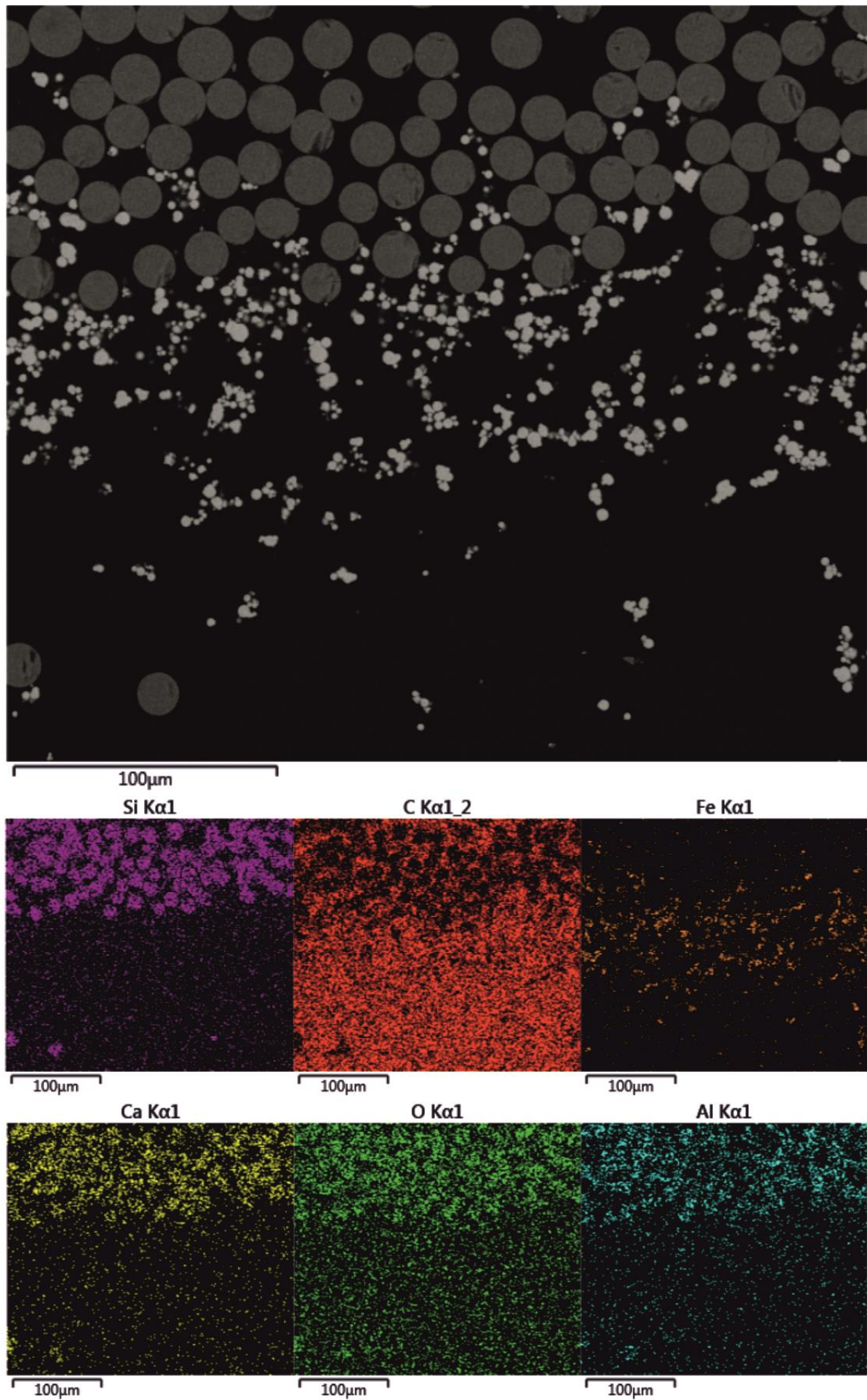
Figure 4.19. EDX mapping of Sample B cross section showing Si, C, Fe, Ca, O and Al elements
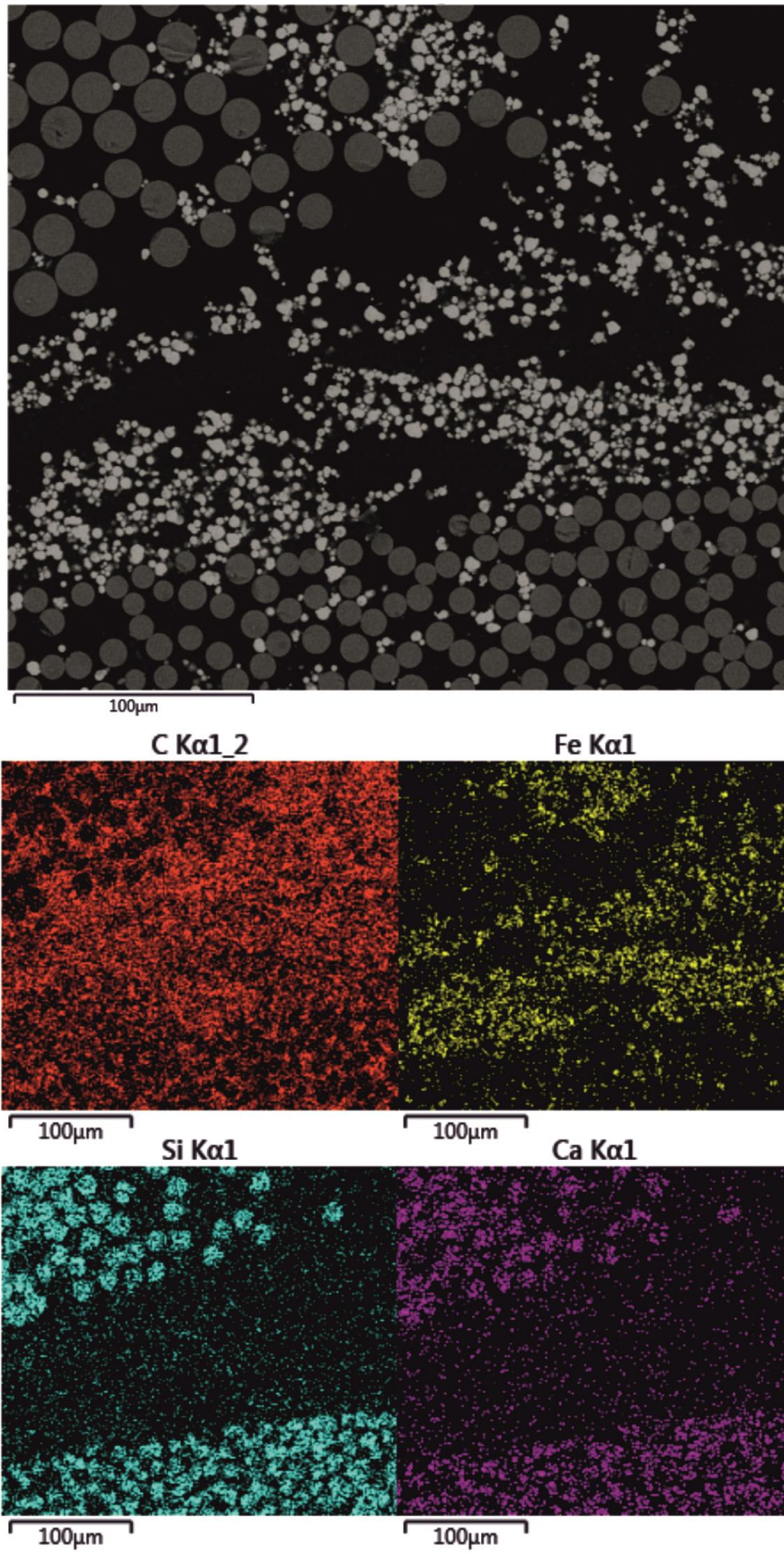
Figure 4.20. EDX mapping of Sample B cross section showing Si, C, Fe, Ca, O and Al elements

Tensile fracture surfaces of manufactured composites were also investigated. Figures 4.21 to 4.24 shows scanning electron micrographs of delaminated tensile specimen containing 0° and 90° oriented fibers, carbonyl iron and a layer of ITO coated fibers. Figures 4.21 to 4.23 show fractures along the 0° oriented fibers, same as the load direction. Carbonyl iron particles in the epoxy matrix can be observed at Figures 4.23 and 4.24. ITO coating patches at the 90° oriented fibers can be observed at Figure 4.24.
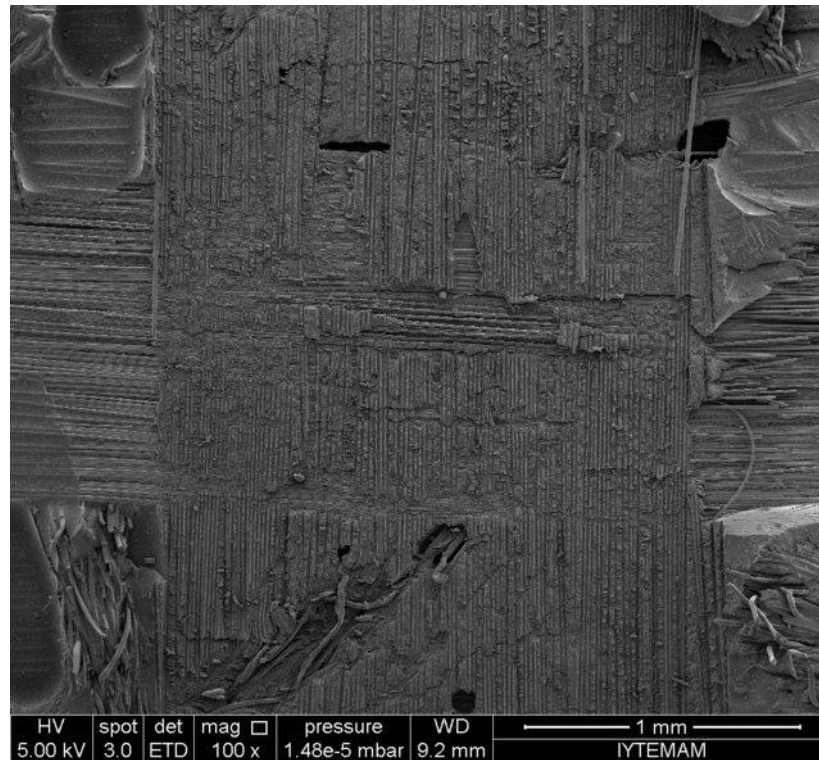
Figure 4.21. Scanning electron micrograph of delaminated tensile fracture surface of glass fiber / carbonyl iron / epoxy based composite (100X)
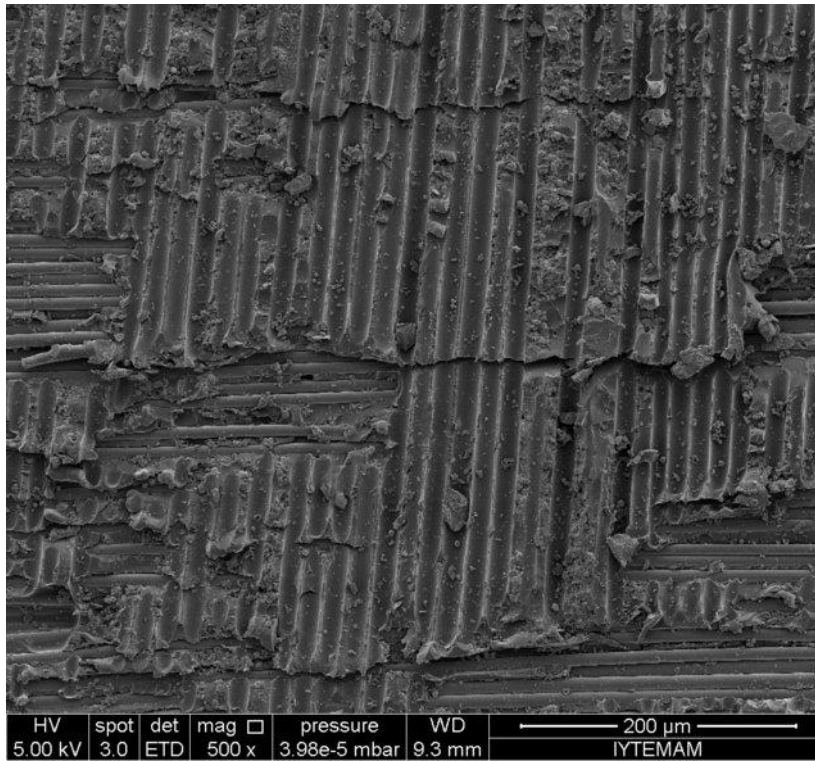
Figure 4.22. Scanning electron micrograph of delaminated tensile fracture surface of glass fiber / carbonyl iron / epoxy based composite (500X)
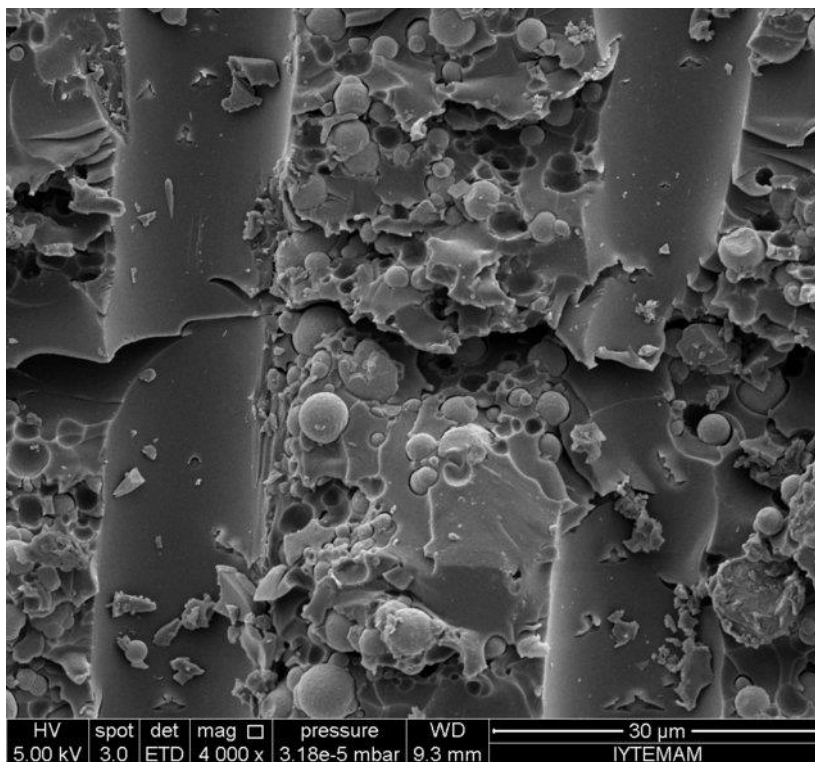

Figure 4.23. Scanning electron micrograph of delaminated tensile fracture surface of glass fiber / carbonyl iron / epoxy based composite (4000X)
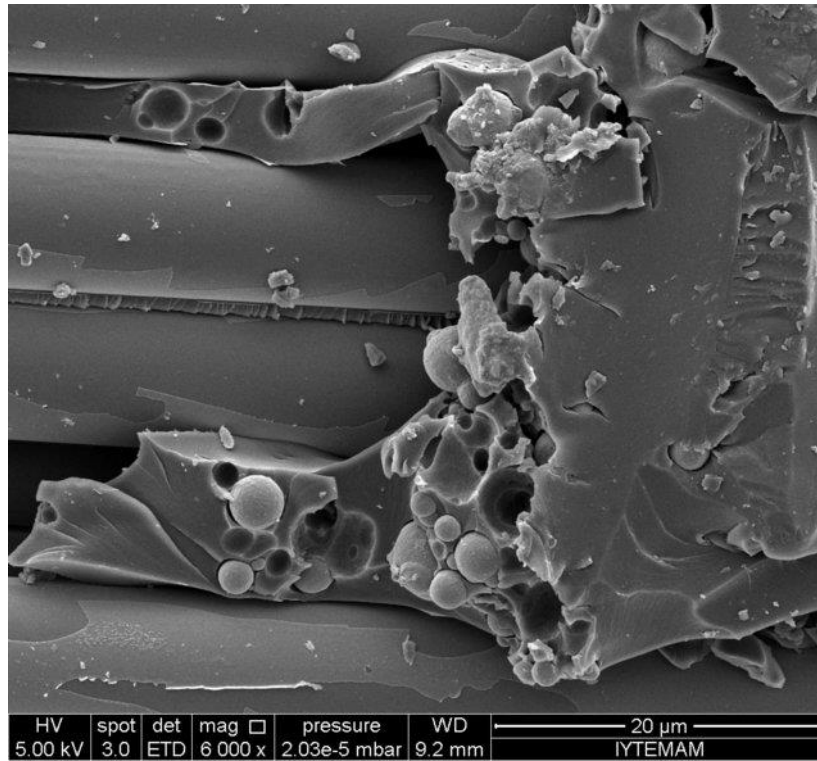
Figure 4.24. Scanning electron micrograph of delaminated tensile fracture surface of
glass fiber / carbonyl iron / epoxy based composite (6000X)

4.3. Thermal Properties

Dynamic mechanical analysis (DMA) was utilized to obtain glass transition temperature (T_g) of the manufactured composites. T_g was observed from loss and storage modulus curves. Tan Delta is the tangent of loss modulus and storage modulus ratio and shows a peak at the T_g. Figure 4.25 shows tan delta curve of unmodified sample A with its peak at 101.13 ^{o}C in addition to loss and storage modulus curves. At least three analysis is performed for each sample. Table 4.9. shows T_g (^{o}C) results from all tested samples.
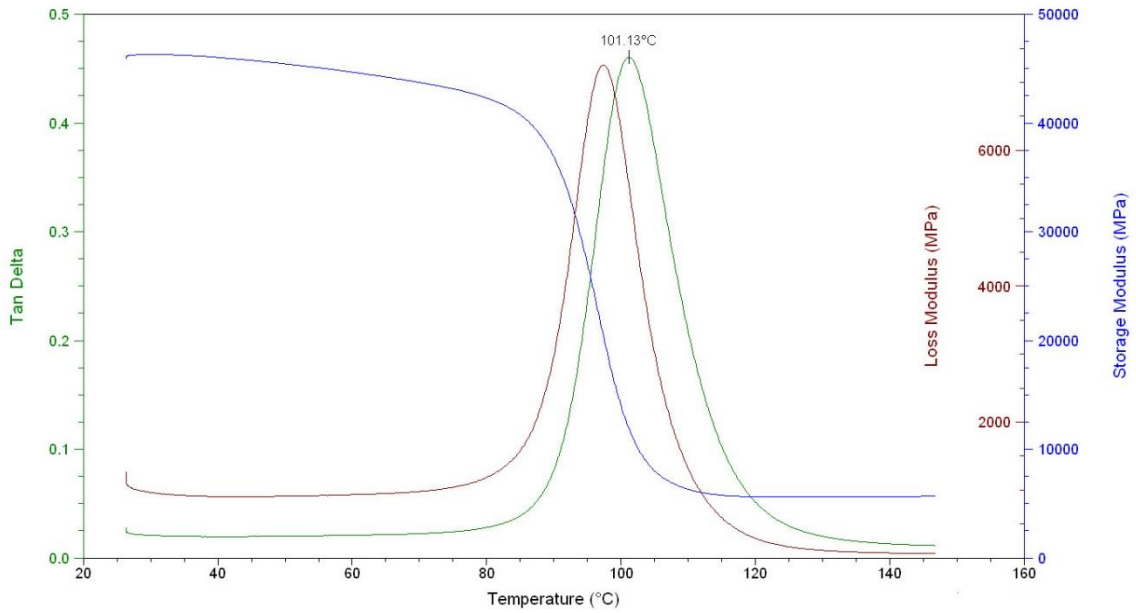
Figure 4.25. Tg analysis result of unmodified E-glass / epoxy laminated composite

Table 4.9. T_g analysis results of composites fabricated

Sample # / ID	A	B	C	D	E
1	101.36	100.21	103.25	102.71	102.39
2	100.99	100.28	104.38	103.55	102.82
3	101.13	99.71	103.57	102.07	103.11
Average	**101.16**	**100.06**	**103.73**	**102.77**	**102.77**
Std. Dev.	**0.18**	**0.31**	**0.58**	**0.74**	**0.36**

Results show that there is no significant change in Tg for all samples. Even thoug highest difference occurs between Sample B and C, this difference contributes to 3 % change in T_g, which can be considered as an experimental error.

4.4. Mechanical Properties

Evaluation of mechanical properties was perfomed by conducting tests such as tensile, bending, compression and Charpy impact. At least five specimens were tested for each test. Results, including strength, modulus, strain at break values are reported below based on tensile, bending and compression tests. Stress-strain graphs are plotted.

4.4.1. Tensile Properties

Tensile test results are summarized throught Tables 4.10 to 4.14. Stress-strain graphs of all specimens are shown in Figures 4.26 to 4.30. All specimes show linear stress-strain curves until failure. None of the specimens show plastic behaviour until failure.

Based on the tensile properties, it is observed that there is about 70 to 100 MPa reduction of tensile strength in all samples containing CI filler with respect to unmodified reference Sample A. Similar trend is seen for modulus values. Variance between strength and modulus values within samples B, C, D and E can be explained by their respective volume fractions but strength and modulus reduction from unmodified reference sample A can not be attributed to volume fraction as the volume fraction of fibers in Sample E is higher than sample A. Thus, it can be said that CI filler in the matrix phase directly affects tensile properties of the samples. Strength and modulus does not vary much as ITO coated layers increase in Samples C, D and E. So that, it is observed that ITO coating does not affect strength and modulues significantly.

Table 4.10. Tensile properties of Sample A

| Sample #	Tensile Strength (MPa)	Tensile Modulus (GPa)	Strain at Break (%)
1	311.9	20.20	1.89
2	333.2	21.00	1.97
3	310.6	20.61	1.84
4	309.6	20.01	1.83
5	314.8	20.83	1.77
Average	**316.0**	**20.53**	**1.86**
Std. Dev.	**9.80**	**0.41**	**0.07**
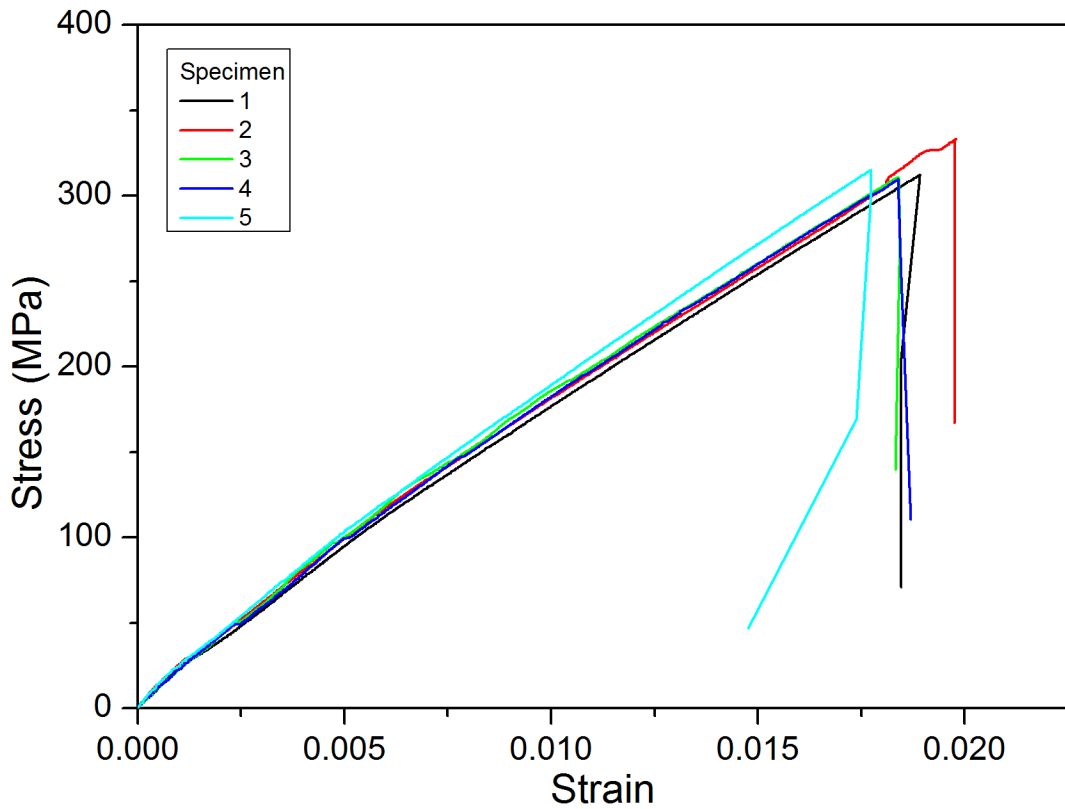
Figure 4.26. Tensile stress vs. strain graphs of Sample A

Table 4.11. Tensile properties of Sample B

| Sample #	Tensile Strength (MPa)	Tensile Modulus (GPa)	Strain at Break (%)
1	241.6	17.51	1.51
2	225.5	16.99	1.55
3	235.4	16.45	1.59
4	234.7	15.93	1.59
5	249.2	16.84	1.79
Average	**237.2**	**16.74**	**1.60**
Std. Dev.	**8.79**	**0.59**	**0.10**
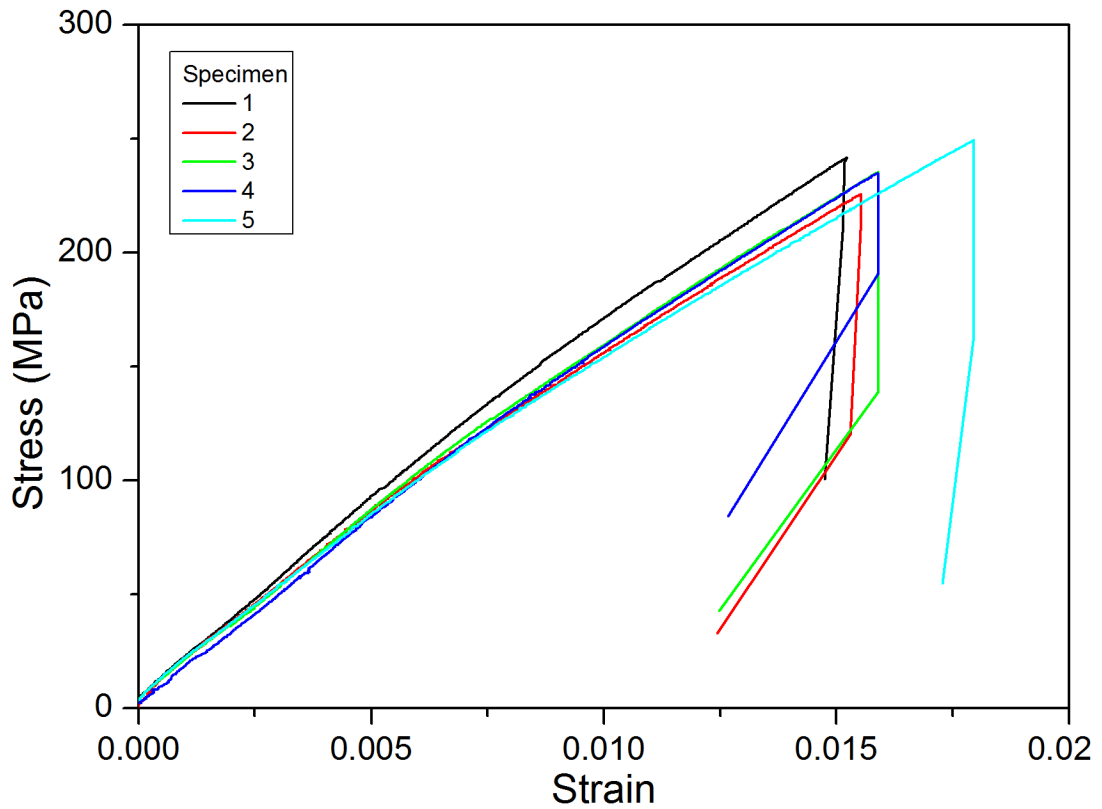
Figure 4.27. Tensile stress vs. strain graphs of Sample B

Table 4.12. Tensile properties of Sample C

| Sample #	Tensile Strength (MPa)	Tensile Modulus (GPa)	Strain at Break (%)
1	253.9	17.41	1.63
2	243.4	16.32	1.63
3	238.6	16.25	1.63
4	256.2	17.53	1.65
5	227.3	16.93	1.57
Average	243.8	16.88	1.62
Std. Dev.	11.78	0.59	0.03
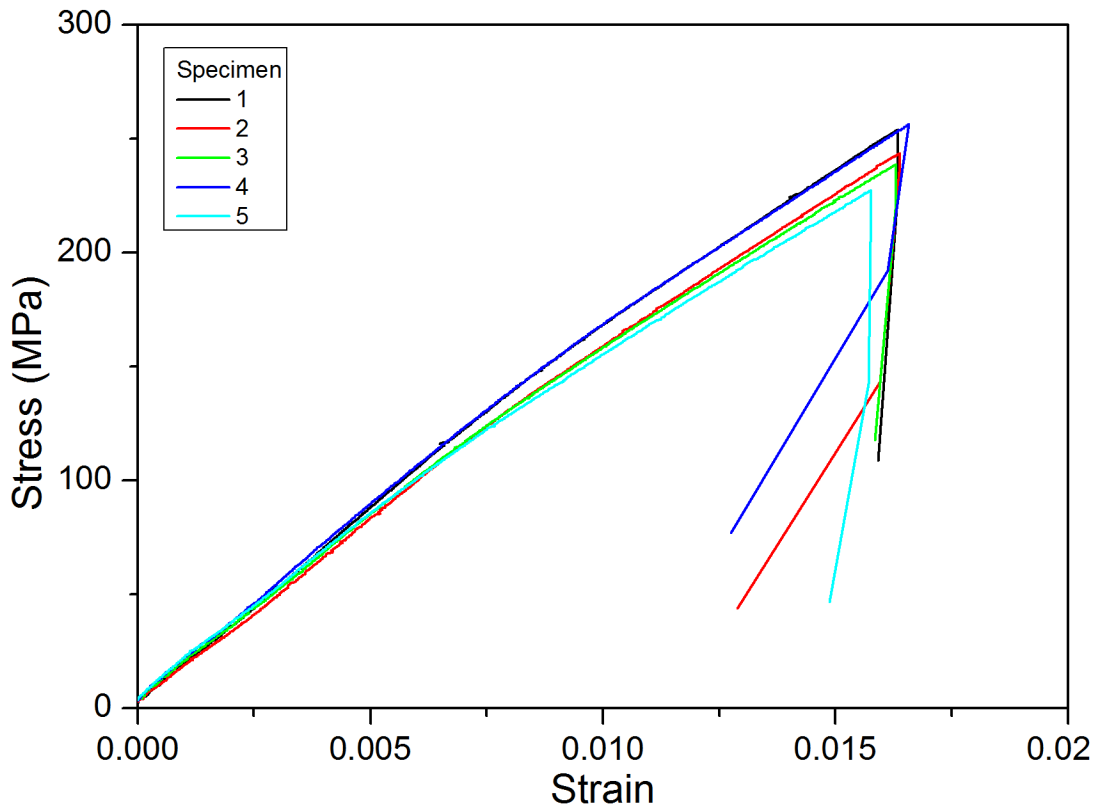
Figure 4.28. Tensile stress vs. strain graphs of Sample C

Table 4.13. Tensile properties of Sample D

| Sample #	Tensile Strength (MPa)	Tensile Modulus (GPa)	Strain at Break (%)
1	216.6	15.61	1.64
2	209.9	14.40	1.65
3	216.5	14.60	1.69
4	217.1	14.25	1.73
5	214.1	15.14	1.64
Average	**214.8**	**14.80**	**1.67**
Std. Dev.	**2.99**	**0.56**	**0.03**
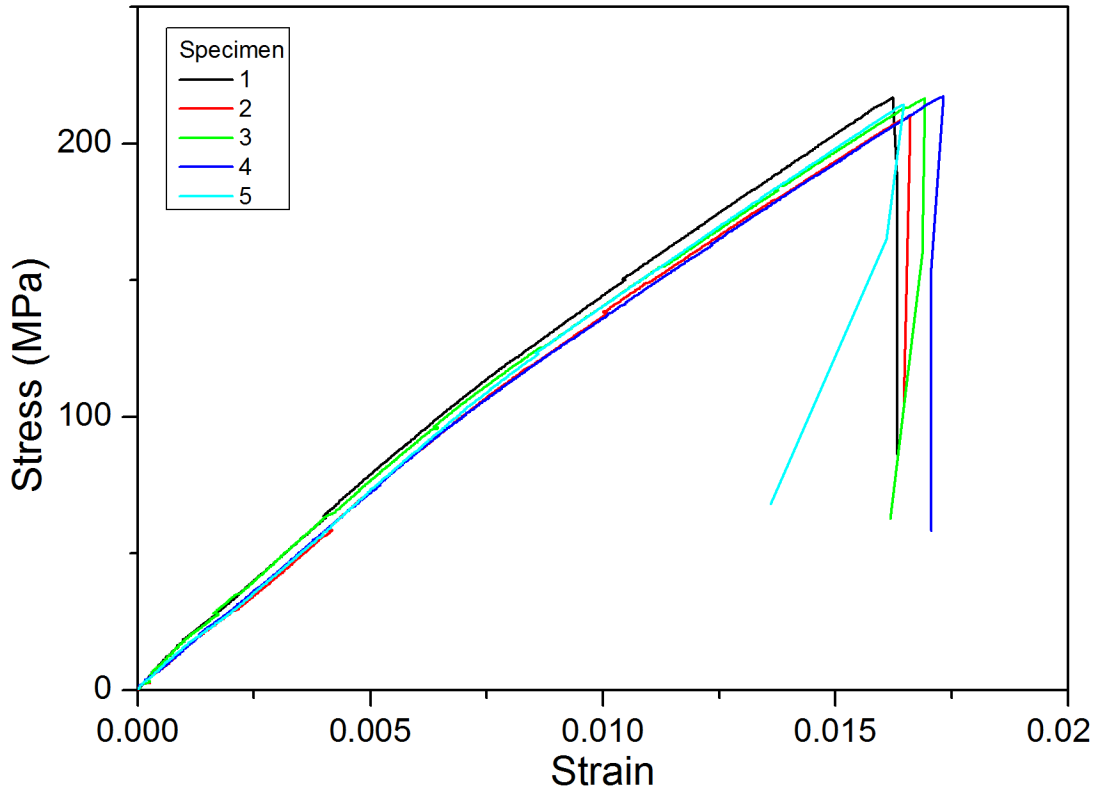
Figure 4.29. Tensile stress vs. strain graphs of Sample D

Table 4.14. Tensile properties of Sample E

| Sample #	Tensile Strength (MPa)	Tensile Modulus (GPa)	Strain at Break (%)
1	248.0	17.47	1.49
2	244.0	19.25	1.30
3	252.5	16.66	1.62
4	245.5	18.75	1.41
5	262.1	17.98	1.63
Average	**250.4**	**18.02**	**1.49**
Std. Dev.	**7.28**	**1.02**	**0.14**
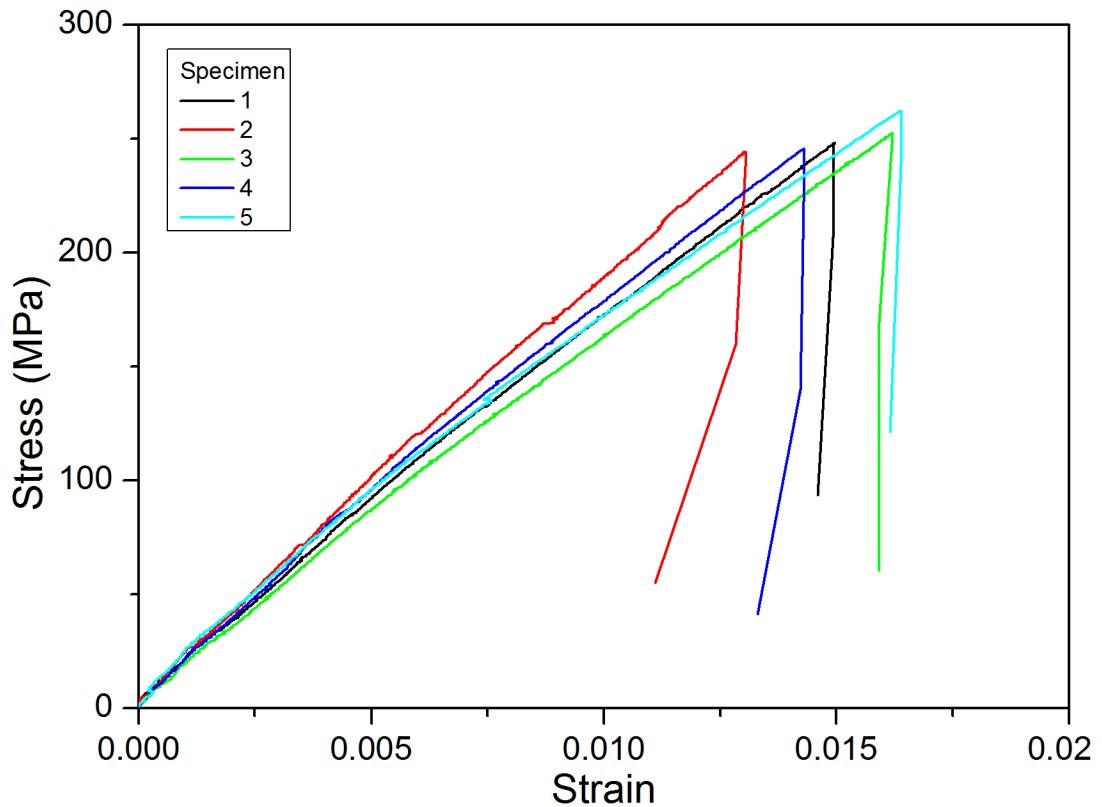
Figure 4.30. Tensile stress vs. strain graphs of Sample E

4.4.2. Flexural Properties

Flexural test results summarized through Tables 4.15 to 4.19. Stress-strain graphs of all specimens are shown in Figures 4.31 to 4.35. All specimes show linear stress-strain curves until failure. None of the specimens show plastic behaviour until failure.

Similar to tensile results, it is observed that there is significant reduction of bending strength loss (about 40 to 110 MPa) in all samples containing CI filler with respect to unmodified reference Sample A. The effect of volume fraction of the samples is increased as their variance with respect to each other increases for Samples B, C, D and E. Again, ITO coating seems not to affect significantly.

Table 4.15. Flexural properties of Sample A

| Sample #	Bending Strength (MPa)	Flexural Modulus (GPa)	Flexural Strain at Break (%)
1	658.6	20.47	3.26
2	606.0	20.52	3.15
3	653.6	22.47	3.24
4	605.1	20.76	3.44
5	584.2	19.79	3.15
Average	**621.4**	**20.80**	**3.24**
Std. Dev.	**32.81**	**0.99**	**0.11**
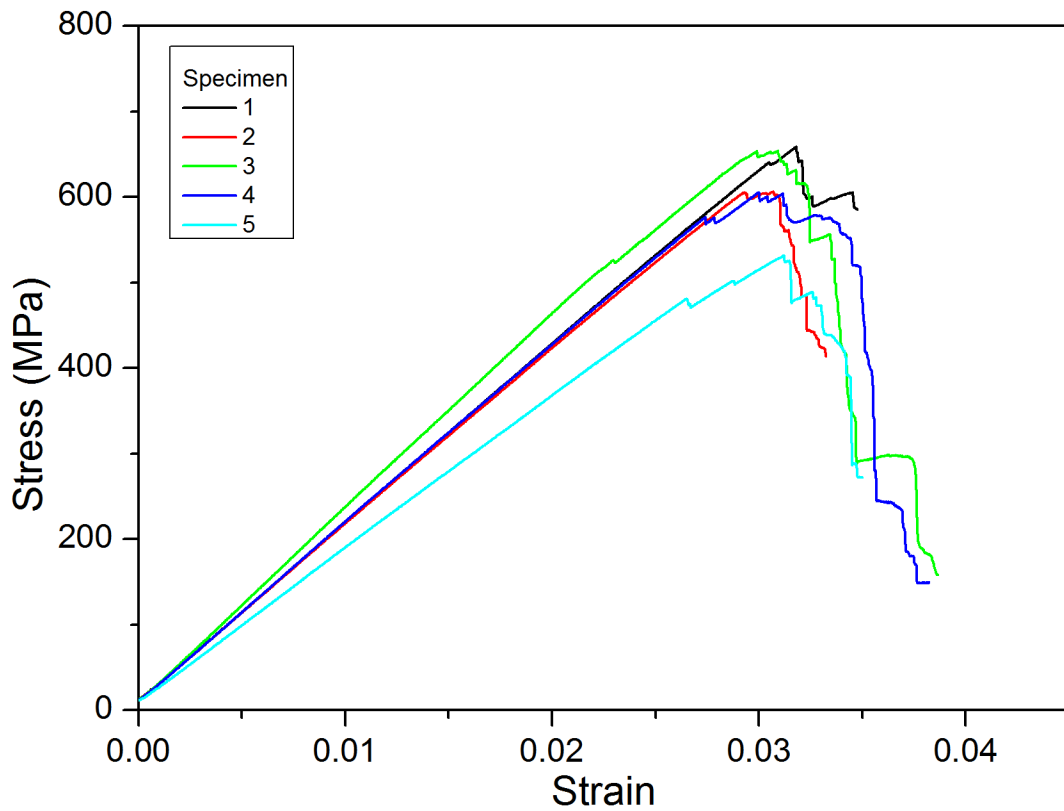
Figure 4.31. Flexural stress vs. strain graphs of Sample A

Table 4.16. Flexural properties of Sample B

| Sample #	Bending Strength (MPa)	Flexural Modulus (GPa)	Flexural Strain at Break (%)
1	507.1	17.98	2.90
2	505.9	17.25	3.01
3	496.4	18.04	2.83
4	504.5	18.21	2.77
5	526.1	17.92	3.01
Average	508.0	17.88	2.90
Std. Dev.	10.95	0.36	0.10
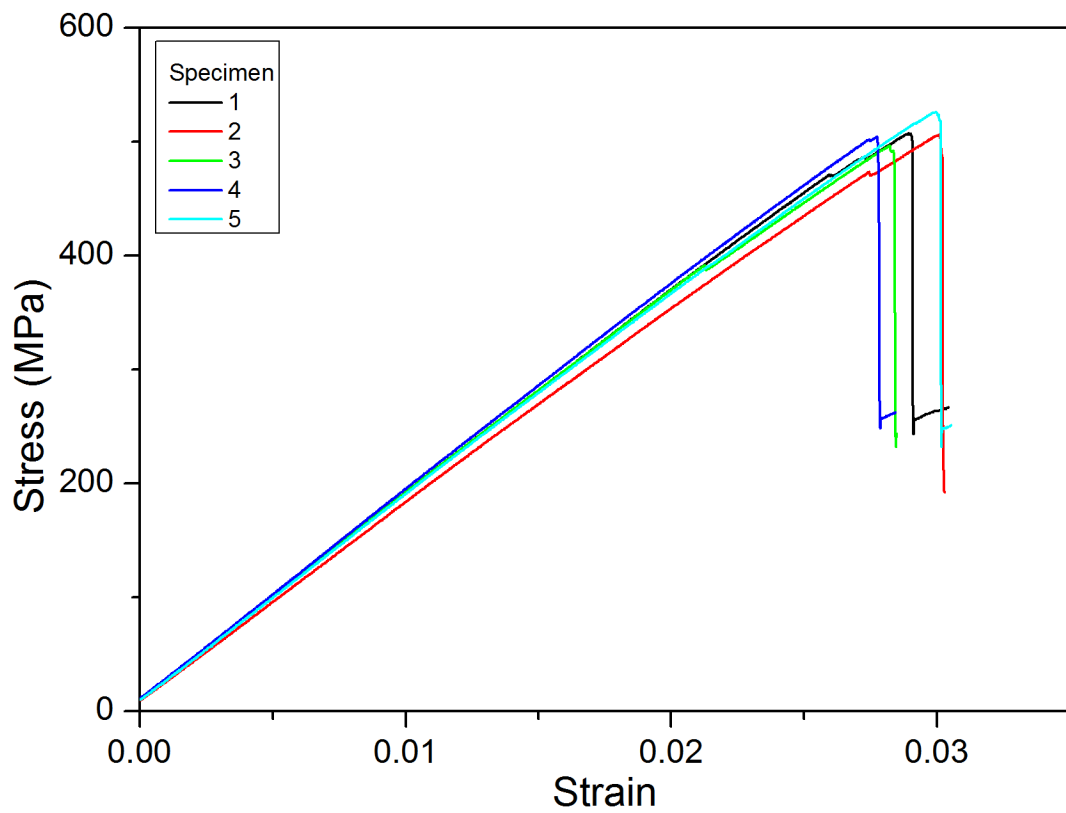
Figure 4.32. Flexural stress vs. strain graphs of Sample B

Table 4.17. Flexural properties of Sample C

| Sample #	Bending Strength (MPa)	Flexural Modulus (GPa)	Flexural Strain at Break (%)
1	540.2	19.66	3.75
2	550.9	18.95	3.73
3	576.1	19.01	3.90
4	561.0	18.89	3.89
5	557.2	18.83	3.92
Average	557.0	19.06	3.83
Std. Dev.	13.23	0.33	0.09
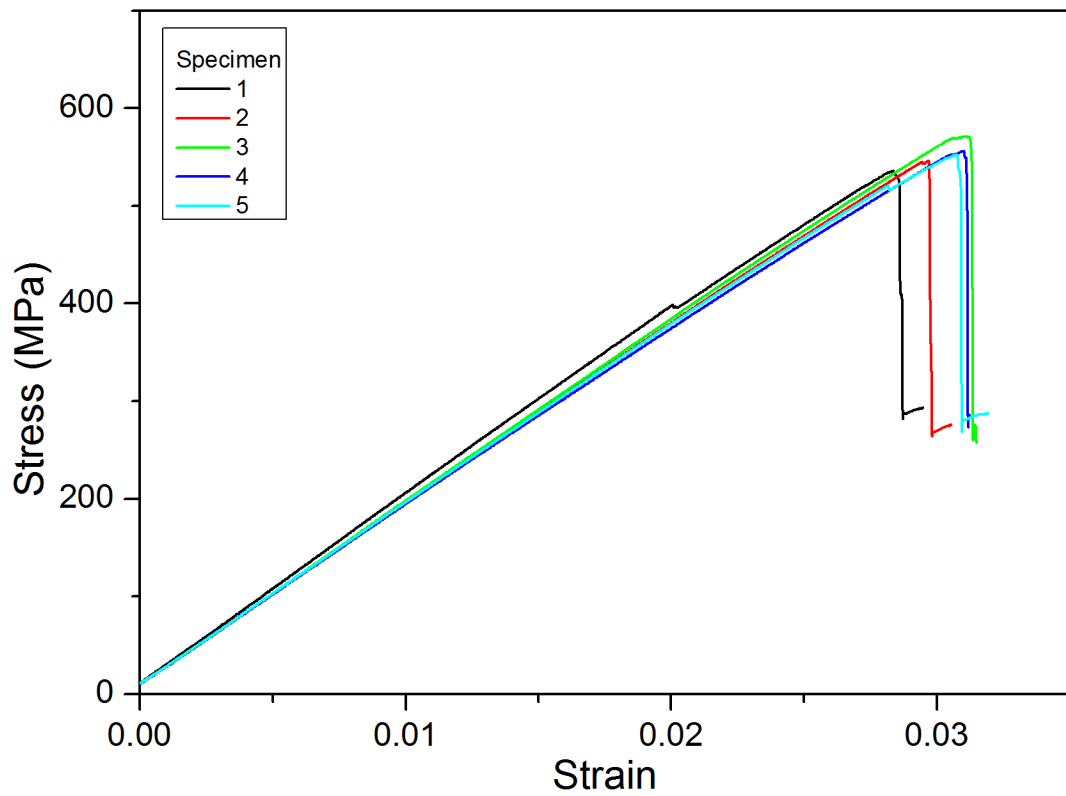
Figure 4.33. . Flexural stress vs. strain graphs of Sample C

Table 4.18. Flexural properties of Sample D

Sample #	Bending Strength (MPa)	Flexural Modulus (GPa)	Flexural Strain at Break (%)
1	523.8	18.27	2.88
2	552.8	16.99	3.35
3	493.9	16.67	2.96
4	511.6	17.49	3.04
5	509.1	16.98	3.09
Average	518.2	17.28	3.06
Std. Dev.	22.05	0.62	0.17
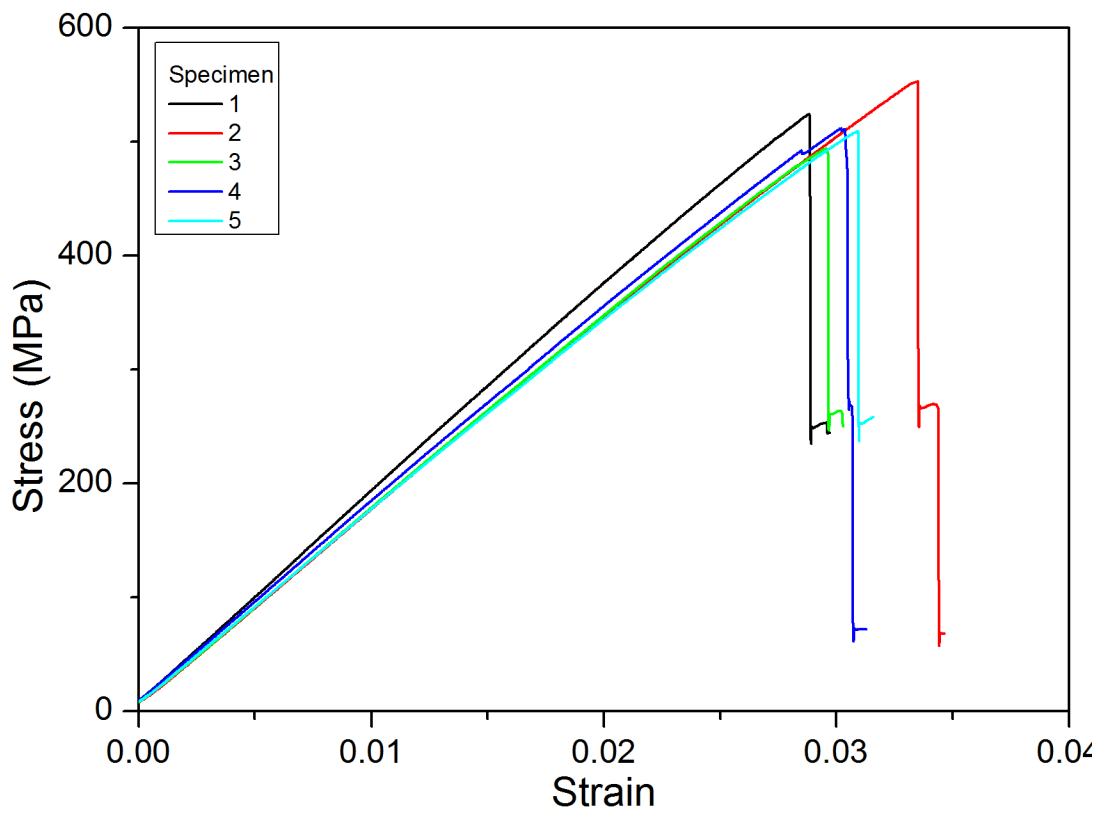
Figure 4.34. Flexural stress vs. strain graphs of Sample D

Table 4.19. Flexural properties of Sample E

Sample #	Bending Strength (MPa)	Flexural Modulus (GPa)	Flexural Strain at Break (%)
1	579.9	20.16	3.26
2	577.0	20.37	3.25
3	608.4	20.90	3.31
4	570.8	20.87	3.27
5	565.6	21.46	3.17
Average	**580.3**	**20.75**	**3.25**
Std. Dev.	**16.63**	**0.50**	**0.05**
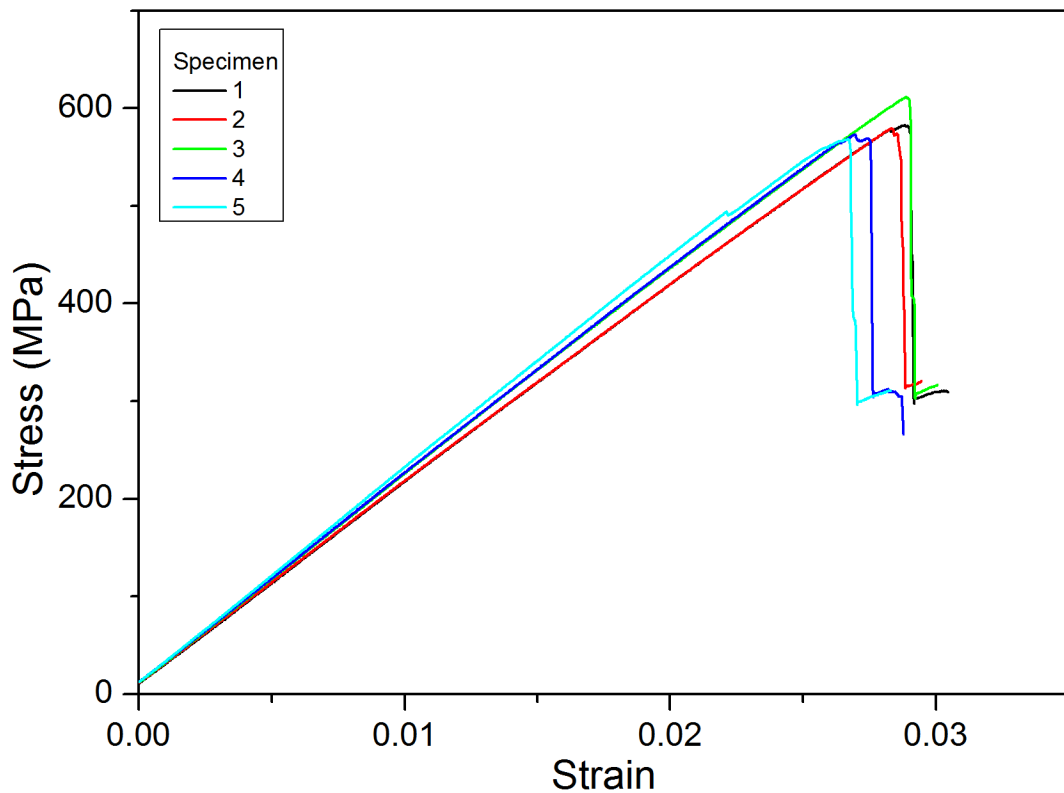
Figure 4.35. Flexural stress vs. strain graphs of Sample E

4.4.3. Compressive Properties

Compression test results summarized through Table 4.20 to 4.24. Stress-strain graphs of all specimens are shown in Figure 4.36 to 4.40. In several specimes, fluctuations are observed. This is due to nature of ASTM 6641 test, that both end loads

and shear loads contributes to compressive stress. These fluctuations are taken into account when calculation of compressive modulus.

Similar to tensile and bending tests but Sample E shows nearly identical results with reference Sample A. Considering their volume fractions, Sample E with 44 wt.%. and Sample A with 41 wt.%., it can be said that about %3 compansate for carbonyl iron filler stregth loss effect for compression tests.

Table 4.20. Compressive properties of Sample A

| Sample #	Compressive Strength (MPa)	Compressive Modulus (GPa)	Compressive Strain at Break (%)
1	404.5	24.07	1.98
2	380.6	23.18	1.89
3	384.5	21.11	1.80
4	416.0	21.99	2.11
5	390.3	21.15	2.04
Average	**395.2**	**22.30**	**1.96**
Std. Dev.	**14.75**	**1.29**	**0.12**
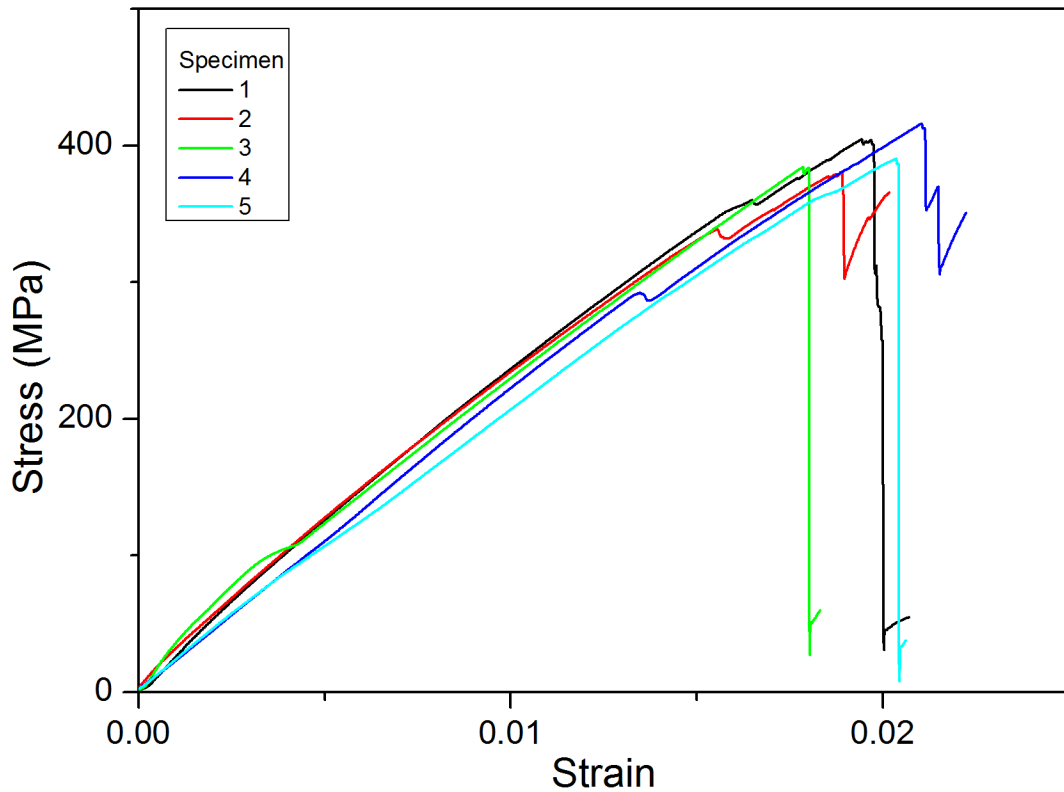
Figure 4.36. Compressive stress vs. strain graphs of Sample A

Table 4.21. Compressive properties of Sample B

Sample #	Compressive Strength (MPa)	Compressive Modulus (GPa)	Compressive Strain at Break (%)
1	325.4	14.24	1.86
2	330.2	15.97	2.20
3	328.8	15.32	2.13
4	322.0	15.73	2.12
5	342.3	16.01	1.94
Average	**329.7**	**15.42**	**2.05**
Std. Dev.	**7.71**	**0.73**	**0.14**
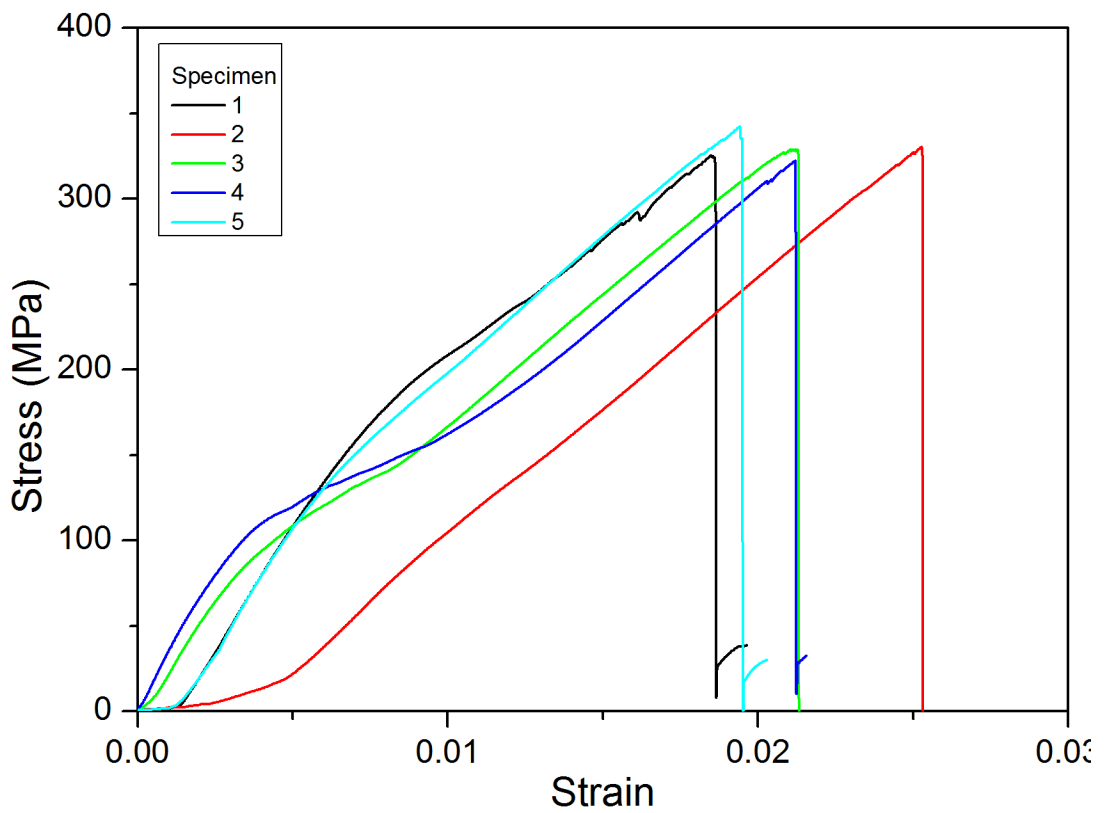
Figure 4.37. Compressive stress vs. strain graphs of Sample B

Table 4.22. Compressive properties of Sample C

Sample #	Compressive Strength (MPa)	Compressive Modulus (GPa)	Compressive Strain at Break (%)
1	354.1	21.45	1.73
2	355.2	21.62	1.95
3	330.2	21.30	1.56
4	306.5	20.51	1.49
5	322.2	17.76	1.78
Average	**333.6**	**20.52**	**1.70**
Std. Dev.	**20.99**	**1.60**	**0.18**
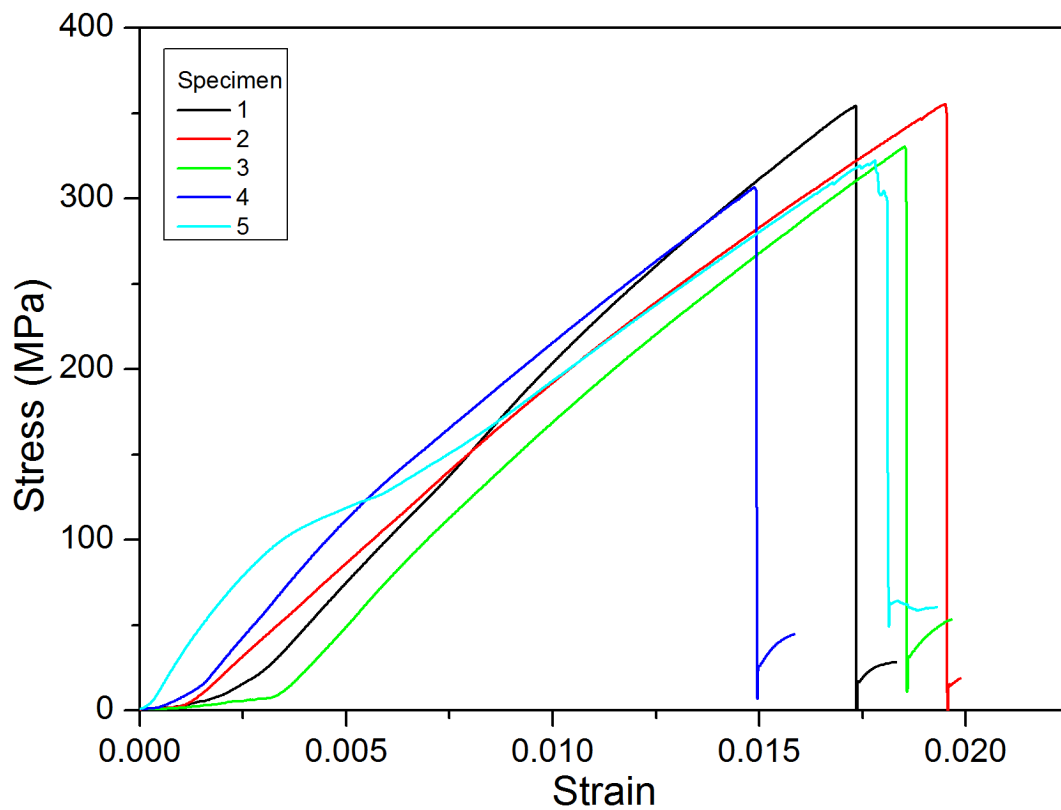
Figure 4.38. Compressive stress vs. strain graphs of Sample C

Table 4.23. Compressive properties of Sample D

Sample #	Compressive Strength (MPa)	Compressive Modulus (GPa)	Compressive Strain at Break (%)
1	372.3	17.90	1.98
2	381.0	17.75	1.97
3	394.5	18.72	2.02
4	348.3	17.78	1.90
5	379.3	19.59	1.60
Average	**375.1**	**18.35**	**1.89**
Std. Dev.	**16.99**	**0.80**	**0.17**
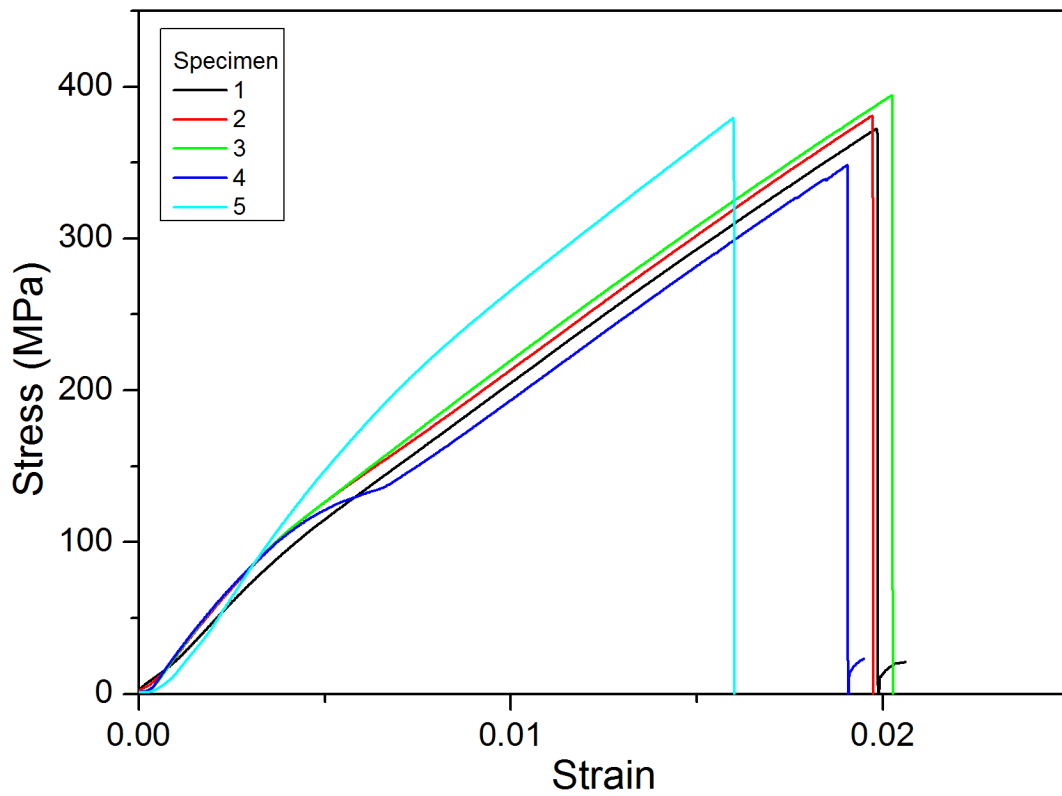
Figure 4.39. Compressive stress vs. strain graphs of Sample D

Table 4.24. Compressive properties of Sample E

Sample #	Compressive Strength (MPa)	Compressive Modulus (GPa)	Compressive Strain at Break (%)
1	386.8	19.11	2.28
2	388.5	18.44	2.15
3	392.2	19.52	2.01
4	368.5	19.76	1.87
5	392.8	21.19	1.86
Average	385.8	19.60	2.03
Std. Dev.	9.97	1.01	0.18
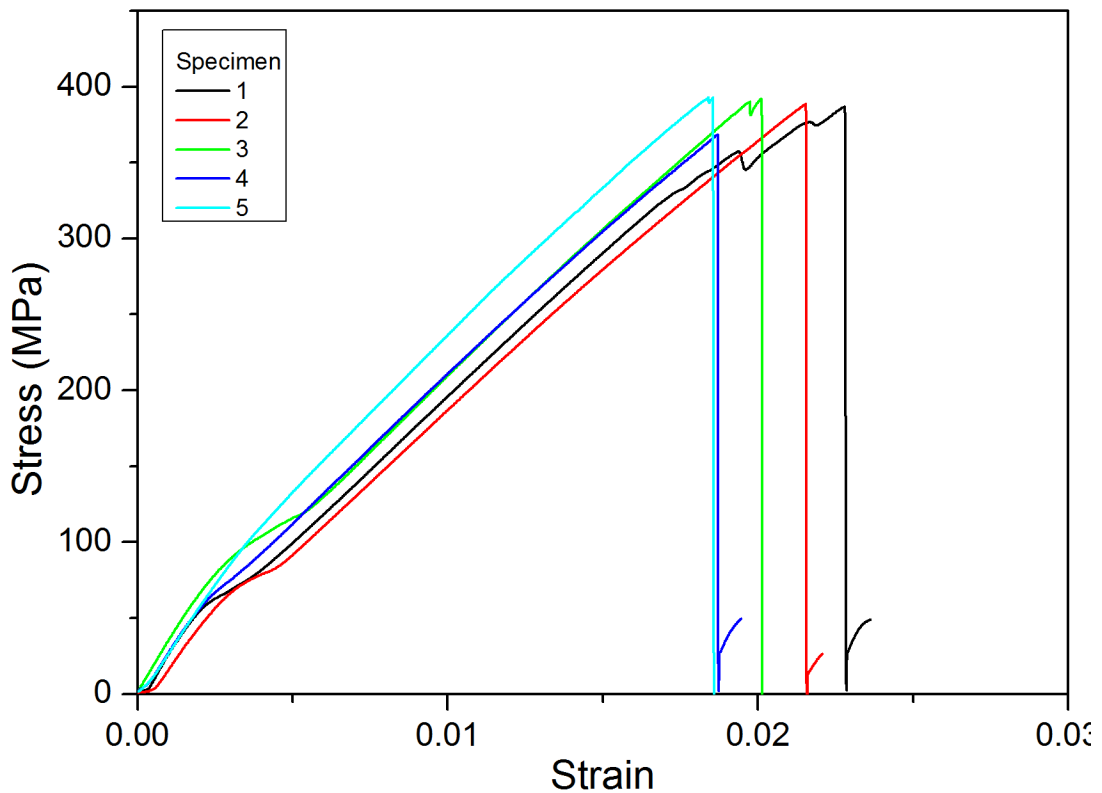
Figure 4.40. Compressive stress vs. strain graphs of Sample E

4.4.4. Impact Behaviour

Impact energy and Charpy impact strength results for all specimens are summarized through Tables 4.25 to 4.29. Impact energy values converted into impact strenght by dividing impact energy to cross sectional area of the notched area. Impact

strength loss in CI containing samples is about 30 to 37 %.Reduction of impact strength in CI included samples is striking compared to quasi-static mechanical tests.

Table 4.25. Impact energy and strength of Sample A

Sample #	Impact Energy (J)	Impact Strength (kJ/m^2)
1	1.458	67.51
2	1.337	61.83
3	1.598	75.01
4	1.666	78.23
5	1.297	58.66
Average	**1.471**	**68.25**
Std. Dev.	**0.160**	**8.35**

Table 4.26. Impact energy and strength of Sample B

Sample #	Impact Energy (J)	Impact Strength (kJ/m^2)
1	1.314	50.83
2	1.044	42.71
3	1.143	46.34
4	1.303	53.66
5	1.120	45.68
Average	**1.184**	**47.84**
Std. Dev.	**0.118**	**4.35**

Table 4.27. Impact energy and strength of Sample C

Sample #	Impact Energy (J)	Impact Strength (kJ/m^2)
1	1.186	46.51
2	1.180	44.63
3	1.209	46.41
4	1.008	44.38
5	1.078	44.76
Average	**1.132**	**45.34**
Std. Dev.	**0.085**	**1.03**

Table 4.28. Impact energy and strength of Sample D

Sample #	Impact Energy (J)	Impact Strength (kJ/m^2)
1	1.170	44.13
2	1.034	41.82
3	1.060	41.31
4	1.118	43.71
5	1.128	44.08
Average	**1.102**	**43.01**
Std. Dev.	**0.054**	**1.34**

Table 4.29. Impact energy and strength of Sample E

Sample #	Impact Energy (J)	Impact Strength (kJ/m^2)
1	1.012	48.23
2	1.186	49.44
3	1.012	45.11
4	1.012	49.63
5	1.190	48.85
Average	**1.082**	**48.25**
Std. Dev.	**0.096**	**1.84**

4.5. Radar Wave Absorbing Properties

Radar wave absorption evaluated at two main steps. First, using permittivity and permeability data of carbonyl iron matrix acquired from the literature, reflection loss was optimized and simulated by equations constructed for each sample structure. Then these results compared with reflection loss measurements that were conducted with a network analyzer and a horn antenna.

4.5.1. GA Optimization Results

Objective of the optimization was set as maximizing the bandwidht of absorbance at or below -10 dB reflection loss. Resistive sheet resistances were taken as 1000 ohms/square as ITO coated fabrics measured as that value. Thus eliminating the

need for optimization for resistive sheet resistances. The only remaining variable was material layer thicknesses between interfaces. GA optimization repeated at least ten times for each sample to ensure maximum bandwith. Table 4.30 summarizes the GA results in aforementioned conditions. Results that were plotted and compared were shown in Figure 4.41.

Table 4.30. Summary of GA optimization results

Sample #	# of Layers	Filler	Resistive Sheets	Bandwidth at -10 dB	t_1 (mm)	t_2 (mm)	t_3 (mm)	t_4 (mm)	Total t (mm)
B	5	25 wt% CI	N/A	%53.17	1.5 mm	N/A	N/A	N/A	1.5 mm
C	6	25 wt% CI	1 ITO coated fabric	%55.82	1.2 mm	0.6 mm	N/A	N/A	1.8 mm
D	6	25 wt% CI	2 ITO coated fabrics	%57.94	0.9 mm	0.3 mm	0.6 mm	N/A	1.8 mm
E	6	25 wt% CI	3 ITO coated fabrics	%59.52	0.6 mm	0.3 mm	0.3 mm	0.6 mm	1.8 mm
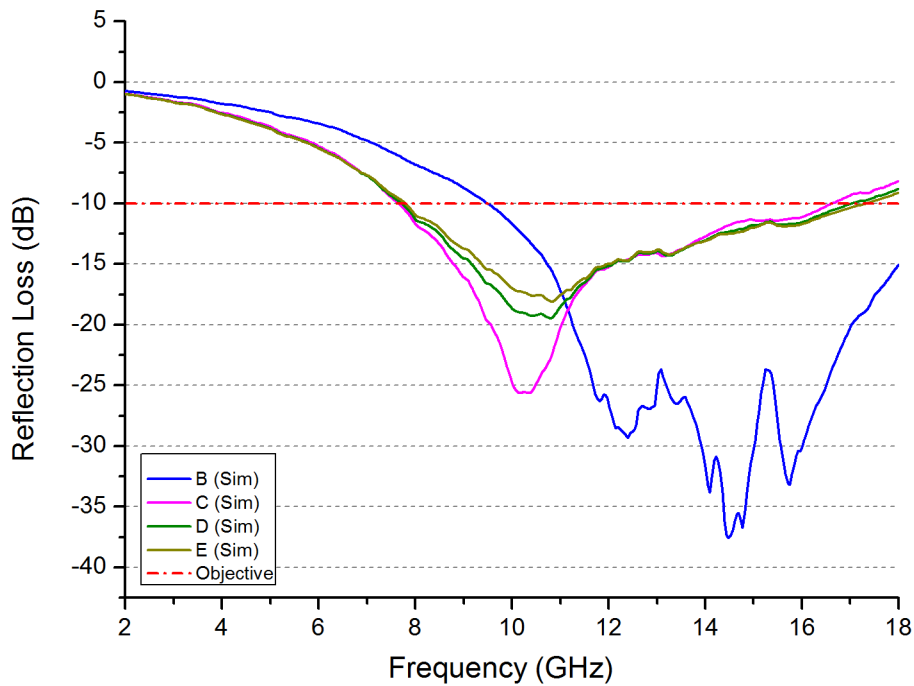
Figure 4.41. Reflection loss comparison of GA optimization results of the RASs

Optimization results shows that as resistive sheets increase, the peak reflection loss reduces but bandwith of absorbance at target reflection loss increases. Latter feature

is more important because -10 dB reflection loss already corresponds to %99 wave absorption ın logarithmic scale, so enlarging the bandwith at or below target reflection loss holds greater importance than having a deep but narrow peak.

Having more resistive sheets in the structure definitely contributes to increase of bandwidth, but considering coating costs and minimal bandwidth increase with each resistive sheet, it can be stated as more than 2 or 3 resistive sheets will be unnecessary for 25% wt. CI filler between 2-18 GHz freqruency range.

4.5.2. Reflection Loss Measurements

Reflection loss measurements conducted as stated before . Data gathered for each sample and a metal plate smoothened for having more expressive curves. Complete reflection from the metal plate is assumed. Complete reflection data was subtracted from S_{11} data of the samples. Resulting curves are shown in Figure 4.42. It is observed that with constant amount of CI filler in matrix phase, increasing the number of resistive sheets increases the reflection loss except sample E which contains 3 layers of resistive sheet but reflection loss falls behind sample D. The resonant frequency for all samples is about 7 GHz.
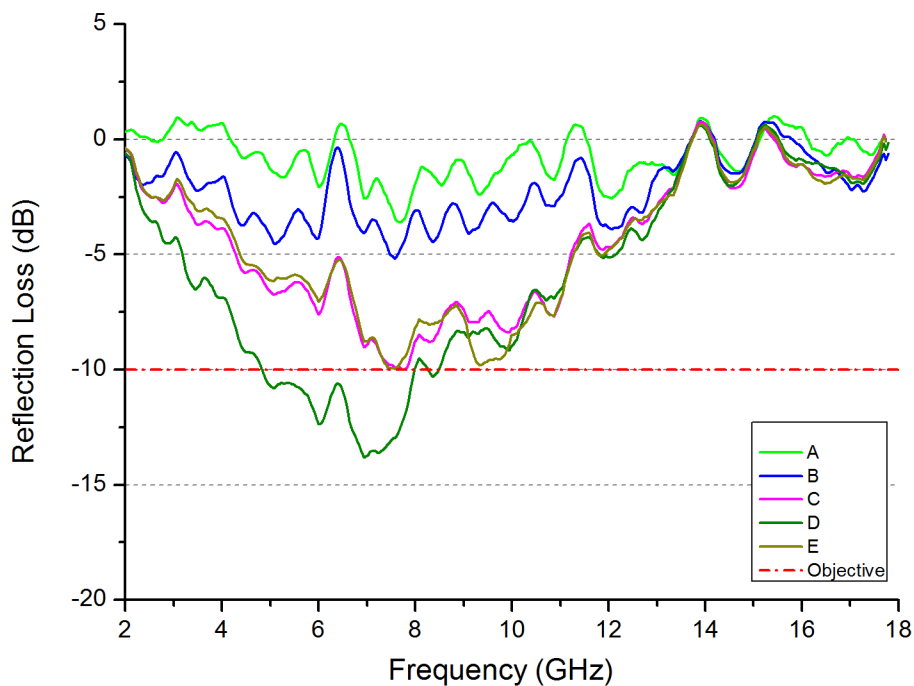
Figure 4.42. Comparison of reflection loss measurements of the RASs

Figure 4.43 shows comparison between reflection loss measurements with simulation results. Significant differences in bandwidth of absorbance and amount of reflection loss are observed. Several reasons can be listed for this observation. First of all, in the GA optimizations, resistive sheets were considered as a uniform thin layer with 1000 ohms/square surface resistance in all directions. In our samples discontinuities exist because of the fiberous nature of the coated region. Continuity in surface resistance is acceptable in fiber direction but discontinuities arise at 90° direction of the fabric.

Another significant argument is the difference between permittivities and permeabilities of the samples and the data used for GA optimization. Variables such as particle size of the absorber and the amount of filler used in the structure directly affects the permittivity and permeability of the samples. Distribution of the absorber particles among the matrix phase also affects electromagnetic properties. Even though data acquired from the literature corresponds to carbonyl iron filler, the amount used in the literature was 50 wt.% compared to 25 wt. % in this study.

Another argument identified as the difference between resistive sheet spacing thickness differs from GA results. Due to manual clamping of the mould at the end of the manufacturing process, it is very difficult to maintain constant thickness for all samples. Table 4.31 summarizes resistive sheet spacing and total thicknesses of the manufactured samples. Compared to Table 4.30, these thicknesses differs notably from GA optimization results. This difference may yield a change in resonant frequency and reflection loss.

Lastly, imperfections at the surface of the samples or at the interface between metal plate and the sample may cause variations and undesirable peaks in the reflection loss measurements. Epoxy based adhesive at the sample-back plate interface may also contribute to reflection loss difference in the measurements. It is also observed that any inclined surface or change in angle of incidence of incident wave considerably changes reflection loss peaks.
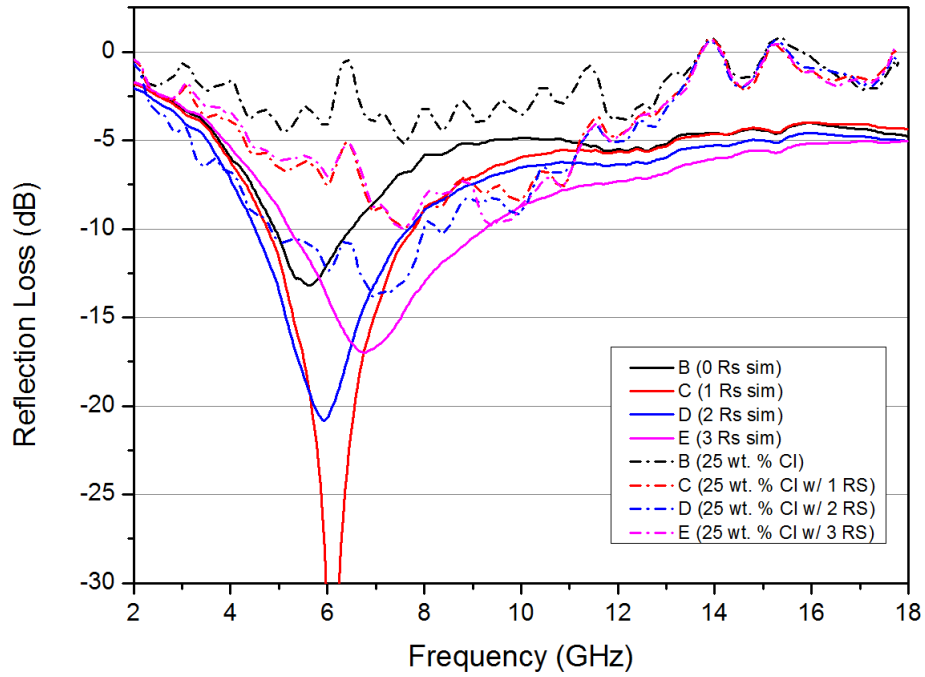
Figure 4.43. Comparison of simulation and measurement results of RASs

Table 4.31. Summary of resistive sheet and filler content and resistive sheet spacing of manufactured samples

Sample #	# of Layers	Filler	Resistive Sheets	t_1 (mm)	t_2 (mm)	t_3 (mm)	t_4 (mm)	Total t (mm)
A	8	N/A	N/A	2.40	N/A	N/A	N/A	2.40
B	8	25 wt% CI	N/A	3.15	N/A	N/A	N/A	3.15
C	8	25 wt% CI	1 ITO coated fabric	2.53	0.36	N/A	N/A	2.90
D	8	25 wt% CI	2 ITO coated fabrics	1.91	0.76	0.38	N/A	3.05
E	8	25 wt% CI	3 ITO coated fabrics	1.00	0.66	0.66	0.33	2.65

CHAPTER 5

CONCLUSIONS

In this study, radar absorbing structures based on epoxy / E-glass system with carbonyl iron (CI) filler were manufactured by hand lay-up technique. Physical and electromagnetic wave absorption properties of fabricated structures were characterized. Physical property investigations include, microstructural evaluation by SEM analysis, determination of fiber volume content by burnt out method, determination of glass transition temperature by DMA, characterization of Charpy impact strength and evaluation of mechanical properties such as ultimate strength, modulus and strain at break for tensile, flexural and compression test configurations. Electromagnetic wave absorption evaluation performed by a network analyzer utilizing a horn anntenna using free space method.

SEM analysis shows that distribution of CI filler particle distribution among the epoxy matrix seem to be non-homogeneous.Glass transition temperature found out to be 100 $^{\circ}$C for unmodified laminated composite. Addition of CI filler does not deviate T_g much as it is observed as 103 $^{\circ}$C in CI and ITO containing samples. All mechanical properties exhibit similar trend for ultimate strength and modulus values. As unmodified sample shows best properties in all conducted tests, it is observed that CI filler within the epoxy matrix drastically reduces ultimate strength and modulus values. Despite the effect of the CI filler, inclusion of ITO coated fabrics that serve as resistive sheets in the structures does not affect mechanical properties. Impact strength shows similar behaviour as mechanical test with reduction of impact strength loss is more explicit.

Genetic Algorithm (GA) optimizations were also performed for enhancing absorbance of the structures. Increasing the number of resistive sheets in the structure also increases the bandwidth of absorbance at target reflection loss, but the impact of additional layers is minimal beyond two resistive sheets. Reflection loss measurements results that structures manufactured achieve up to 12 dB with varying thicknesses between 2.65 mm to 3.15 mm. Resonant frequency of the all samples observed as 7 GHz.

Comparison of optimization results with reflection loss measurements shows distinct behaviour between theoritical and real life conditions. This distinction is explanied by several reasons such as, non-homogeneous resistive sheet layers, difference of electromagnetic property data acquired from literature with manufactured radar absorbing structure, resistive sheet spacing thickness, total thickness, imperfect binding of sample and back metal plate. Overcoming these difficulties will surely yield more consisting results between simulations and measurements.

This work is based on laminated composites with CI filler. There are several more types of electromagnetic absorbers avaliable as mention in Chapter 2. Magnetic absorbers such as barium hexaferrite or carbon based absorbers such as carbon nanotubes (CNT), carbon short and nano fibers, graphite are possible candidates for particulate absorbers for radar absorbing structures. Further studies should include comparison of these materials with carbonyl iron.

Multilayer structures with single matrix phase (epoxy / E- glass fiber / CI) were studied in this thesis. Multilayer configurations with different types of matrices might be a possible candidate for wide band absorbers. For this type of structures perfect binding between layers is a serious consideration. Sandwich structures with foam spacers which have radar absorption capabilities is another type of structure that might focused on.

Angle of incidence of incident waves should also be taken into account as in real life situations, a wide range of angle of incidence occurs between the radar wave and the absorbing structure and the effects on the absorbance should be studied.

Lastly, different geometries is a possible field of study for radar absorbing structures. Real life applications of these structures may exhibit complex geometries, such as wind turbine blades and aircraft wings. Thus curved and cylindrical surfaces holds great importance for absorbance.

REFERENCES

Barton, David K, and Sergey A Leonov. 1997. *Radar Technology Encyclopedia.*

Campell, F. C. 2003. *Manufacturing Processes for Advanced Composites*. Elsevier.

Chambers, B, and A Tennant. 1994. "Design of Wideband Jaumann Radar Absorbers with Optimum Oblique Incidence Performance." *Electronics Letters* 30 (18): 5–7.

Chambers, B, and A Tennant. 1996. "Optimised Design of Jaumann Radar Absorbing Materials Using a Genetic Algorithm." *IEE Proceedings - Radar, Sonar and Navigation* 143 (1): 23.

Feng, Y.B., T. Qiu, and C.Y. Shen. 2007. "Absorbing Properties and Structural Design of Microwave Absorbers Based on Carbonyl Iron and Barium Ferrite." *Journal of Magnetism and Magnetic Materials* 318 (1-2) (November): 8–13.

Feng, Yong-bao, Tai Qiu, Chun-ying Shen, and Xiao-yun Li. 2006. "Electromagnetic and Absorption Properties of Carbonyl Iron/rubber Radar Absorbing Materials." *IEEE Transactions on Magnetics* 42 (3) (March): 363–368.

Folgueras, Luiza De C., Mauro a. Alves, and Mirabel C. Rezende. 2010. "Microwave Absorbing Paints and Sheets Based on Carbonyl Iron and Polyaniline: Measurement and Simulation of Their Properties." *Journal of Aerospace Technology and Management* 2 (1): 63–70.

Foroozesh, A.R., A. Cheldavi, and F. Hodjat. 2000. "Design of Jaumann Absorbers Using Adaptive Genetic Algorithm." In *2000 5th International Symposium on Antennas, Propagation, and EM Theory*, 227–230. IEEE.

Gama, Adriana Medeiros, and Mirabel Cerqueira Rezende. 2010. "Complex Permeability and Permittivity Variation of Carbonyl Iron Rubber in the Frequency Range of 2 to 18 GHz." *Journal of Aerospace Technology and Management* 2 (1): 59–62.

Gen, Mitsuo, and Runwei Cheng. 2000. *Genetic Algorithms and Engineering Optimization. Vasa.*

Guan, J.G., Z.P. Gan, G.H. Gao, and Qing Jie Zhang. 2003. "Optimized Design of Multi-Ingredient Radar Absorbing Materials Using Genetic Algorithms." *Key Engineering Materials* 249: 367–372.

Hashimoto, Osamu, Takumi Abe, Ryuji Satake, Miki Kaneko, and Yasuo Hashimoto. 1995. "Design and Manufacturing of Resistive-Sheet Type Wave Absorber at 60 GHz Frequency Band." *IEICE Transactions on Communications* E78-B: 246–252.

Haupt, RL, and SE Haupt. 2004. *Practical Genetic Algorithms*. Second Edi. Wiley.

Hepcke, Gerhard 2007. *The Radar War, 1930-1945*.

Hill, Robert T. 2007. "Radar." *Encyclopedia of Science & Technology*. McGraw-Hill.

Jenn, David C. 2005. *Radar and Laser Cross Section Engineering*.

Ke, Li, Zhang Xin, Hou Xinyu, and Zhang Peng. 2011. "Analysis and Design of Multilayer Jaumann Absorbers." *2011 IEEE International Conference on Microwave Technology & Computational Electromagnetics* (May): 81–84.

Kim, J, S Lee, and C Kim. 2008. "Comparison Study on the Effect of Carbon Nano Materials for Single-layer Microwave Absorbers in X-band." *Composites Science and Technology* 68 (14) (November): 2909–2916.

Kim, Sung-soo, Yeo-choon Yoon, and Ki-ho Kim. 2003. "Electromagnetic Wave Absorbing Properties of High-Permittivity Ferroelectrics Coated with ITO Thin Films of 377." *Journal of Electroceramics* 10: 95–101.

Knott, E.F., and C.D. Lunden. 1995. "The Two-Sheet Capacitive Jaumann Absorber." *IEEE Transactions on Antennas and Propagation* 43 (11) (November): 1339.

Knott, Eugene F, John F Shaeffer, and Michael T Tuley. 2004. *Radar Cross Section*.

Lederer, P G. 1992. "Modelling of Practical Salisbury Screen Absorbers" (ii).

Lee, Sang-Eui, Ji-Ho Kang, and Chun-Gon Kim. 2006. "Fabrication and Design of Multi-layered Radar Absorbing Structures of MWNT-filled Glass/epoxy Plain-weave Composites." *Composite Structures* 76 (4) (December): 397–405.

Long, AC. 2005. *Design and Manufacture of Textile Composites*. CRC Press.

Malinauskas, A. 2001. "Chemical Deposition of Conducting Polymers." *Polymer* 42 (9) (April): 3957–3972.

Mallick, P. K. 2007. *Fiber-reinforced Composites*. CRC Press.

Marchant, S, F.R. Jones, T.P.C. Wong, and P.V. Wright. 1998. "Free-space Microwave Characteristics of Polypyrrole Coated Glass Fibre." *Synthetic Metals* 96 (1) (July): 35–41.

Mazumdar, Sanjay K. 2001. *Composites Manufacturing - Materials, Product and Process Engineering*. CRC Press.

McDonald, Jacob J, Billy C Brock, Steven E Allen, Paul G Clem, Joshua A Paquette, Ward E Patitz, William K Miller, David A Calkins, and Hung Jacques Loui. 2012. *Radar-Cross-Section Reduction of Wind Turbines (Part 1)*.

Meshram, M.R, Nawal K Agrawal, Bharoti Sinha, and P.S Misra. 2004. "Characterization of M-type Barium Hexagonal Ferrite-based Wide Band

Microwave Absorber." *Journal of Magnetism and Magnetic Materials* 271 (2-3) (May): 207–214.

Micheli, D., C. Apollo, R. Pastore, and M. Marchetti. 2010. "X-Band Microwave Characterization of Carbon-based Nanocomposite Material, Absorption Capability Comparison and RAS Design Simulation." *Composites Science and Technology* 70 (2) (February): 400–409.

Micheli, Davide. 2011. "Design of Microwave Absorbing Structure and Microwave Shielding Structure by Using Composite Materials, Nanomaterials and Evolutionary Computation". Sapienza Universita Di Roma.

Michielssen, Eric, J.-M. Sajer, S Ranjithan, and Raj Mittra. 1993. "Design of Lightweight, Broad-band Microwave Absorbers Using Genetic Algorithms." *IEEE Transactions on Microwave Theory and Techniques* 41 (6): 1024–1031.

Motevasselian, Alireza. 2010. "On the Scattering Reduction of an Aircraft Wing Profile Enclosing an Antenna."

Munk, Ben A. 2000. *Frequency Selective Surfaces*. Hoboken, NJ, USA: John Wiley & Sons, Inc. doi:10.1002/0471723770.

Naito, Y., and K. Suetake. 1971. "Application of Ferrite to Electromagnetic Wave Absorber and Its Characteristics." *IEEE Transactions on Microwave Theory and Techniques* 19 (1) (January): 65–72.

Oh, Jung-Hoon, Kyung-Sub Oh, Chun-Gon Kim, and Chang-Sun Hong. 2004. "Design of Radar Absorbing Structures Using Glass/epoxy Composite Containing Carbon Black in X-band Frequency Ranges." *Composites Part B: Engineering* 35 (1) (January): 49–56.

Oikonomou, a., T. Giannakopoulou, and G. Litsardakis. 2007. "Design, Fabrication and Characterization of Hexagonal Ferrite Multi-layer Microwave Absorber." *Journal of Magnetism and Magnetic Materials* 316 (2) (September): e827–e830.

Parida, RC, D Singh, and NK Agarwal. 2007. "Implementation of Multilayer Ferrite Radar Absorbing Coating with Genetic Algorithm for Radar Cross-section Reduction at X-band." *Indian Journal of Radio & Space Physics* 36 (April): 145–152.

Park, K, S Lee, C Kim, and J Han. 2006. "Fabrication and Electromagnetic Characteristics of Electromagnetic Wave Absorbing Sandwich Structures." *Composites Science and Technology* 66 (3-4) (March): 576–584.

Park, K.-Y., J.-H. Han, J.-B. Kim, and S.-K. Lee. 2011. "Two-layered Electromagnetic Wave-absorbing E-glass/epoxy Plain Weave Composites Containing Carbon Nanofibers and NiFe Particles." *Journal of Composite Materials* 45 (26) (September 9): 2773–2781.

Park, Ki-Yeon, Jae-Hung Han, Sang-Bok Lee, Jin-Bong Kim, Jin-Woo Yi, and Sang-Kwan Lee. 2009. "Fabrication and Electromagnetic Characteristics of Microwave Absorbers Containing Carbon Nanofibers and NiFe Particles." *Composites Science and Technology* 69 (7-8) (June): 1271–1278.

Perini, Jose, and L.S. Cohen. 1991. "Design Radar Absorbing Materials (RAMs) for Wide Range of Angles of Incidence." In *IEEE 1991 International Symposium on Electromagnetic Compatibility*, 418–424. IEEE.

Perini, Jose, and L.S. Cohen. 1993. "Design of Broad-band Radar-absorbing Materials for Large Angles of Incidence." *IEEE Transactions on Electromagnetic Compatibility* 35 (2) (May): 223–230.

Pinho, Magali Silveira, Maria Luisa Gregori, Regina Célia Reis Nunes, and Bluma Guenther Soares. 2002. "Performance of Radar Absorbing Materials by Waveguide Measurements for X- and Ku-band Frequencies." *European Polymer Journal* 38 (11) (November): 2321–2327.

Qing, Y. C., W. C. Zhou, S. Jia, F. Luo, and D. M. Zhu. 2010. "Electromagnetic and Microwave Absorption Properties of Carbonyl Iron and Carbon Fiber Filled Epoxy/silicone Resin Coatings." *Applied Physics A* 100 (4) (May 15): 1177–1181.

Qing, Yuchang, Wancheng Zhou, Shu Jia, Fa Luo, and Dongmei Zhu. 2010. "Dielectric Properties of Carbon Black and Carbonyl Iron Filled Epoxy–silicone Resin Coating." *Journal of Materials Science* 45 (7) (January 9): 1885–1888.

Qing, Yuchang, Wancheng Zhou, Fa Luo, and Dongmei Zhu. 2009. "Microwave-absorbing and Mechanical Properties of Carbonyl-iron/epoxy-silicone Resin Coatings." *Journal of Magnetism and Magnetic Materials* 321 (1) (January): 25–28.

Rosa, Igor Maria De, Adrian Dinescu, Fabrizio Sarasini, Maria Sabrina Sarto, and Alessio Tamburrano. 2010. "Effect of Short Carbon Fibers and MWCNTs on Microwave Absorbing Properties of Polyester Composites Containing Nickel-coated Carbon Fibers." *Composites Science and Technology* 70 (1) (January): 102–109.

Seo, Il Sung, Woo Seok Chin, and Dai Gil Lee. 2004. "Characterization of Electromagnetic Properties of Polymeric Composite Materials with Free Space Method." *Composite Structures* 66 (1-4) (October): 533–542.

Sivanandam, SN, and SN Deepa. 2007. "Introduction to Genetic Algorithms."

Stenger-Smith, John D. 1998. "Intrinsically Electrically Conducting Polymers. Synthesis, Characterization, and Their Applications." *Progress in Polymer Science* 23 (1) (January): 57–79.

Tellakula, R a, V K Varadan, T C Shami, and G N Mathur. 2004. "Carbon Fiber and Nanotube Based Composites with Polypyrrole Fabric as Electromagnetic Absorbers." *Smart Materials and Structures* 13 (5) (October 1): 1040–1044.

Du Toit, L.J., and J.H. Cloete. 1989. "A Design Process for Jaumann Absorbers." In *Digest on Antennas and Propagation Society International Symposium*, 1558–1561. IEEE.

Du Toit, L.J., and J.H. Cloete. 1990. "Advances in the Design of Jaumann Absorbers." In *International Symposium on Antennas and Propagation Society, Merging Technologies for the 90's*, 1212–1215. IEEE.

Tong, Xingcun Colin. 2009. "Absorber Materials." In *Advanced Materials and Design for Electromagnetic Interference Shielding*. Vol. 2.

Wikimedia Foundation, Inc., "Lockheed F-117 Nightawk" Wikipedia. http://en.wikipedia.org/wiki/F_117 (accessed June 6, 2013).

Wikimedia Foundation, Inc., "Northrop Grumman B-2 Spirit" Wikipedia. http://en.wikipedia.org/wiki/Northrop_Grumman_B-2_Spirit (accessed June 6, 2013).

Wikimedia Foundation, Inc., "Lockheed Martin F-22 Raptor" Wikipedia. http://en.wikipedia.org/wiki/Lockheed_Martin_F-22_Raptor (accessed June 6, 2013).

Wikimedia Foundation, Inc., "Lockheed Martin F-35 Lightning II" Wikipedia http://en.wikipedia.org/wiki/Lockheed_Martin_F-35_Lightning_II (accessed June 6, 2013)..

Wikimedia Foundation, Inc., "Eurofighter Typhoon" Wikipedia. http://en.wikipedia.org/wiki/Eurofighter (accessed June 6, 2013).

Wikimedia Foundation, Inc., "Sea Shadow (IX-529)" Wikipedia. http://en.wikipedia.org/wiki/Sea_Shadow (accessed June 6, 2013).

Wikimedia Foundation, Inc., "La Fayette-class frigate" Wikipedia. http://en.wikipedia.org/wiki/La_Fayette_class_frigate (accessed June 6, 2013).

Wikimedia Foundation, Inc., "Visby-class corvette" Wikipedia. http://en.wikipedia.org/wiki/Visby-class_corvette (accessed June 6, 2013).

Xu, Yonggang, Deyuan Zhang, Jun Cai, Liming Yuan, and Wenqiang Zhang. 2013. "Microwave Absorbing Property of Silicone Rubber Composites with Added Carbonyl Iron Particles and Graphite Platelet." *Journal of Magnetism and Magnetic Materials* 327 (February): 82–86.

Zhang, Baoshan, Yong Feng, Jie Xiong, Yi Yang, and Huaixian Lu. 2006. "Microwave-absorbing Properties of De-aggregated Flake-shaped Carbonyl-iron Particle Composites at 2-18 GHz." *IEEE Transactions on Magnetics* 42 (7) (July): 1778–1781.

APPENDIX A

MATLAB COMPUTER PROGRAMS

- Program 1 written for simulation of radar absorbing structures

```
freq1=(2:0.01:18)';
freq=freq1*1E9;

perma_zero=1.2566370614E-6;
permi_zero=8.854E-12;

mur1_r1=csvread('CI_v50_mu_r.csv',1,0);
mur1_r2=fit(mur1_r1(:,1),mur1_r1(:,2),'linearinterp');
mur1_i1=csvread('CI_v50_mu_i.csv',1,0);

mur1_i2=fit(mur1_i1(:,1),mur1_i1(:,2),'linearinterp');
epr1_r1=csvread('CI_v50_eps_r.csv',1,0);

epr1_r2=fit(epr1_r1(:,1),epr1_r1(:,2),'linearinterp');
epr1_i1=csvread('CI_v50_eps_i.csv',1,0);

epr1_i2=fit(epr1_i1(:,1),epr1_i1(:,2),'linearinterp');

mur1_r=feval(mur1_r2,freq1);
mur1_i=feval(mur1_i2,freq1);
epr1_r=feval(epr1_r2,freq1);
epr1_i=feval(epr1_i2,freq1);

mur=complex(mur1_r,-mur1_i);
epr=complex(epr1_r,-epr1_i);

Zl=0;
zetzero=sqrt(perma_zero/permi_zero);

mur1=mur;
epr1=epr;

mur2=mur;
epr2=epr;

mur3=mur;
epr3=epr;

mur4=mur;
```

```
epr4=epr;

Rs1=1000;
Rs2=1000;
Rs3=1000;

thickness1=0.3*1e-3;
thickness2=0.6*1e-3;
thickness3=0.6*1e-3;
thickness4=0.3*1e-3;

i=1;

while i<=size(freq,1)

beta1(i)=1i*2*pi()*(freq(i)*sqrt(perma_zero*permi_zero)*sqrt(mur1(i)*epr1(i)));
nk1(i)=sqrt(perma_zero/permi_zero)*sqrt(mur1(i)/epr1(i));
zet1(i)=nk1(i)*((Zl+nk1(i)*tanh(beta1(i)*thickness1))/(nk1(i)+Zl*tanh(beta1(i)*thickne
ss1)));

zet1_R(i)=Rs1*zet1(i)/(Rs1+zet1(i));

beta2(i)=1i*2*pi()*(freq(i)*sqrt(perma_zero*permi_zero)*sqrt(mur2(i)*epr2(i)));
nk2(i)=sqrt(perma_zero/permi_zero)*sqrt(mur2(i)/epr2(i));
zet2(i)=nk2(i)*((zet1_R(i)+nk2(i)*tanh(beta2(i)*thickness2))/(nk2(i)+zet1_R(i)*tanh(b
eta2(i)*thickness2)));

zet2_R(i)=Rs2*zet2(i)/(Rs2+zet2(i));

beta3(i)=1i*2*pi()*(freq(i)*sqrt(perma_zero*permi_zero)*sqrt(mur3(i)*epr3(i)));
nk3(i)=sqrt(perma_zero/permi_zero)*sqrt(mur3(i)/epr3(i));
zet3(i)=nk3(i)*((zet2_R(i)+nk3(i)*tanh(beta3(i)*thickness3))/(nk3(i)+zet2_R(i)*tanh(b
eta3(i)*thickness3)));

zet3_R(i)=Rs3*zet3(i)/(Rs3+zet3(i));

beta4(i)=1i*2*pi()*(freq(i)*sqrt(perma_zero*permi_zero)*sqrt(mur4(i)*epr4(i)));
nk4(i)=sqrt(perma_zero/permi_zero)*sqrt(mur4(i)/epr4(i));
zet4(i)=nk4(i)*((zet3_R(i)+nk4(i)*tanh(beta4(i)*thickness4))/(nk4(i)+zet3_R(i)*tanh(b
eta4(i)*thickness4)));

zet_last(i)=zet4(i);

RLtanh(i)=20*log10(abs((zet_last(i)-zetzero)/(zet_last(i)+zetzero)));

i=i+1;

end

amounttotal=size(RLtanh,2);
```

```
amountloss=size((find(RLtanh<= -10)),2);

Bandwidth = 100*(amountloss/amounttotal)

objectiveRL=-10*ones(size(freq,1),1);

numberofRs=3;
numberofLays=4;


figure(1);
objectiveplot=plot(freq1,objectiveRL);
set(objectiveplot,'Color','red','LineWidth',2,'LineStyle','--','Marker','none');
hold on;
figure(1); RLplot=plot(freq1,RLtanh); grid on; title(['Reflection Loss vs. Frequency (3
Resistive Sheet with Front Spacer (4 Layer)) (Banwidth=%' num2str(Bandwidth,4) ')']);
xlabel('Frequency (GHz)');  ylabel('Reflection Loss (dB)');
set(RLplot,'Color','black','LineWidth',1.5);


hold off;

amounttotal=size(RLtanh,2);
amountloss=size((find(RLtanh<= -10)),2);

Bandwidth = 100*(amountloss/amounttotal);

annotation(figure(1),'textbox',...
    [0.793750000000001 0.53448275862069 0.103906249999999 0.40],...
    'String',{['# of Rs: ' num2str(numberofRs)],['# of Layers: '
num2str(numberofLays)],['Bandwidth: %' num2str(Bandwidth,4)],['Rs_1: '
num2str(Rs1) ' \Omega'],['Rs_2: ' num2str(Rs2) ' \Omega'],['Rs_3: ' num2str(Rs3) '
\Omega'],['d_1: ' num2str(1000*thickness1) ' mm'],['d_2: ' num2str(1000*thickness2) '
mm'],['d_3: ' num2str(1000*thickness3) ' mm'],['d_4: ' num2str(1000*thickness4) '
mm']},...
    'FitBoxToText','off',...
    'BackgroundColor',[1 1 1]);
```

- Program 2 written for genetic algorithm optimizaiton of radar absorbing
  structures
  - *Execution of Genetic Algorithm*

```
freq1=(2:0.01:13.5)';
freq=freq1*1E9;

mur1_r1=csvread('CI_v50_mu_r.csv',1,0);
mur1_r2=fit(mur1_r1(:,1),mur1_r1(:,2),'linearinterp');
mur1_i1=csvread('CI_v50_mu_i.csv',1,0);
mur1_i2=fit(mur1_i1(:,1),mur1_i1(:,2),'linearinterp');
epr1_r1=csvread('CI_v50_eps_r.csv',1,0);
```

```
epr1_r2=fit(epr1_r1(:,1),epr1_r1(:,2),'linearinterp');
epr1_i1=csvread('CI_v50_eps_i.csv',1,0);
epr1_i2=fit(epr1_i1(:,1),epr1_i1(:,2),'linearinterp');

mur1_r=feval(mur1_r2,freq1);
mur1_i=feval(mur1_i2,freq1);
epr1_r=feval(epr1_r2,freq1);
epr1_i=feval(epr1_i2,freq1);

mur=complex(mur1_r,-mur1_i);
epr=complex(epr1_r,-epr1_i);


load('RAM_variable_values.mat');


lb = [1 1 1 1 1 1 1];
ub = [1 1 1 33 33 33 33];

intCon=1:7;
options = gaoptimset('CrossoverFrac',0.5,'PopulationSize',120,...
    'StallGen',200,'Generations',250,...
    'PlotFcns',@gaplotbestf);


ga_counter=15;

ans_run=zeros(ga_counter, 8);
i=1;
while i<=ga_counter
tic;
    [xOpt,fVal] = ga(@(x)GA_RAM_objFunc(x,Res,Thickness_Val,freq,mur,epr),...
    7,[0 0 0 0.0003 0.0003 0.0003 0.0003],[0.01],[],[],lb,ub,[],intCon,options);

disp('Integer Solution Returned by GA:')
disp(xOpt)

ans_run(i,:)=[fVal Res(xOpt(1)) Res(xOpt(2)) Res(xOpt(3)) Thickness_Val(xOpt(4))
Thickness_Val(xOpt(5)) Thickness_Val(xOpt(6)) Thickness_Val(xOpt(7))];
total_thickness(i,1)=1000*(ans_run(i,5)+ans_run(i,6)+ans_run(i,7)+ans_run(i,8));
i=i+1;
tEnd=toc/60
end
ans_run_thickness=[ans_run total_thickness];
save('GA_4layer_3Rs_result.mat','ans_run_thickness')
```

- *Reflection Loss Function*

```
freq1=(2:0.01:13.5)';
freq=freq1*1E9;

mur1_r1=csvread('CI_v50_mu_r.csv',1,0);
mur1_r2=fit(mur1_r1(:,1),mur1_r1(:,2),'linearinterp');
mur1_i1=csvread('CI_v50_mu_i.csv',1,0);
mur1_i2=fit(mur1_i1(:,1),mur1_i1(:,2),'linearinterp');
epr1_r1=csvread('CI_v50_eps_r.csv',1,0);
epr1_r2=fit(epr1_r1(:,1),epr1_r1(:,2),'linearinterp');
epr1_i1=csvread('CI_v50_eps_i.csv',1,0);
epr1_i2=fit(epr1_i1(:,1),epr1_i1(:,2),'linearinterp');

mur1_r=feval(mur1_r2,freq1);
mur1_i=feval(mur1_i2,freq1);
epr1_r=feval(epr1_r2,freq1);
epr1_i=feval(epr1_i2,freq1);

mur=complex(mur1_r,-mur1_i);
epr=complex(epr1_r,-epr1_i);


load('RAM_variable_values.mat');


lb = [1 1 1 1 1 1 1];
ub = [1 1 1 33 33 33 33];

intCon=1:7;
options = gaoptimset('CrossoverFrac',0.5,'PopulationSize',120,...
   'StallGen',200,'Generations',250,...
   'PlotFcns',@gaplotbestf);


ga_counter=15;

ans_run=zeros(ga_counter, 8);
i=1;
while i<=ga_counter
tic;
   [xOpt,fVal] = ga(@(x)GA_RAM_objFunc(x,Res,Thickness_Val,freq,mur,epr),...
   7,[0 0 0 0.0003 0.0003 0.0003 0.0003],[0.01],[],[],lb,ub,[],intCon,options);

disp('Integer Solution Returned by GA:')
disp(xOpt)

ans_run(i,:)=[fVal Res(xOpt(1)) Res(xOpt(2)) Res(xOpt(3)) Thickness_Val(xOpt(4))
Thickness_Val(xOpt(5)) Thickness_Val(xOpt(6)) Thickness_Val(xOpt(7))];
total_thickness(i,1)=1000*(ans_run(i,5)+ans_run(i,6)+ans_run(i,7)+ans_run(i,8));
```

```
i=i+1;
tEnd=toc/60
end
ans_run_thickness=[ans_run total_thickness];
save('GA_4layer_3Rs_result.mat','ans_run_thickness')
```

- ▪ *Fitness Function*

```
function G = GA_RAM_objFunc(x,Res,Thickness_Val,freq,mur,epr)
y = zeros(10,1);
y(1) = Res(x(1));
y(2) = Res(x(2));
y(3) = Res(x(3));
y(4) = Thickness_Val(x(4));
y(5) = Thickness_Val(x(5));
y(6) = Thickness_Val(x(6));
y(7) = Thickness_Val(x(7));

F = Reflection_Loss_Calc(y, freq, mur, epr);

amountloss=size((find(F<= -10)),2);
amounttotal=size(F,2);

G = -(amountloss/amounttotal);
```